Experimental and Analytical Investigation of Ammonia-Water Desorption in Microchannel Geometries

A Thesis
Presented to
The Academic Faculty

By

Matthew D. Determan

In Partial Fulfillment
Of the Requirements for the Degree
Master of Science in Mechanical Engineering

Georgia Institute of Technology
August, 2005

Experimental and Analytical Investigation of Ammonia-Water Desorption in Microchannel Geometries

Approved by:

Dr. Srinivas Garimella, Chair
School of Mechanical Engineering
Georgia Institute of Technology

Dr. Sheldon Jeter
School of Mechanical Engineering
Georgia Institute of Technology

Dr. Samuel Shelton
School of Mechanical Engineering
Georgia Institute of Technology

Date Approved: June 10, 2005

To my wife – Jenny

ACKNOWLEDGEMENT

I would like to thank my advisor, Dr. Srinivas Garimella for his guidance thorough the course of this work. I would like to thank Mark Meacham, whose prior work with Dr. Garimella laid the ground work for this project. I would also like to thank all of the students in the Sustainable Thermal Systems Laboratory, especially Tim Ernst and Jesse Killion, for their thoughtful advice and their willingness to help.

Matthew D. Determan

TABLE OF CONTENTS

LIST OF TABLES

LIST OF FIGURES

LIST OF SYMBOLS

a	wetted area fraction
A	area
c_p	constant pressure specific heat
$\tilde{c}_p$	molar constant pressure specific heat
c_v	constant volume specific heat
C	molar concentration
D	diameter, binary diffusion coefficient
g	gravitational acceleration
h	enthalpy
k	thermal conductivity
LMTD	log mean temperature difference
$\dot{m}$	mass flow rate
M	molecular weight
$\dot{n}$	molar flux
Nu	Nusselt number
P	Pressure
Pe	Pecelt number
Pr	Prandlt number
q	quality
$\dot{Q}$	heat transfer rate
R	thermal resistance, Gas Constant

Re	Reynolds number
Sc	Schmidt number
Sh	Sherwood number
T	temperature
u	uncertainty
U	overall heat transfer coefficient
V	velocity
$\dot{V}$	Volume flow rate
x	mass based liquid concentration
$\tilde{x}$	molar based liquid concentration
y	mass based vapor concentration
$\tilde{y}$	molar based vapor concentration
z	mass based condensing/evaporating flux concentration
$\tilde{z}$	molar based condensing/evaporating flux concentration

Greek Letters

α	heat transfer coefficient
β	mass transfer coefficient
Γ	mass flow rate per wetted length of tube
δ	film thickness
ε	equivalent roughness
η	fractional distance through vapor boundary layer
μ	viscosity

ϕ_T	parameter in Ackerman correction
Φ	parameter in mixture rules
π	pi
ρ	density
σ	collision diameter

Sub-scripts and Super-scripts

a	ammonia
avg	average
bulk	bulk
cs	cross sectional
des	desorber
dry	dry portion
eff	effective
f	film
free	free area to vapor flow
glyc	glycol/water solution
i	component index
int	interface
j	component index
ID	inside diameter
in	in
l	liquid

max	maximum
mix	mixture
OD	outside diameter
out	out
pp	per pass
s	solution
seg	segment
T	total
translational	translational
v	vapor
w	tube wall, water
wet	wetted portion

SUMMARY

An experimental and analytical study of a microchannel ammonia-water desorber was conducted in this study. The desorber consists of 5 passes of 16 tube rows each with 27, 1.575 mm outside diameter x 140 mm long tubes per row for a total of 2160 tubes. The desorber is an extremely compact 178 mm x 178 mm x 0.508 m tall component, and is capable of transferring the required heat load (~17.5 kW) for a representative residential heat pump system. Experimental results indicate that the heat duty ranged from 5.37 kW to 17.46 kW and the overall heat transfer coefficient ranges from 388 to 617 W/m^2-K. The analytical model predicts temperature, concentration and mass flow rate profiles through the desorber, as well as the effective wetted area of the heat transfer surface. Heat and mass transfer correlations as well as locally measured variations in the heating fluid temperature are used to predict the effective wetted area. The average wetted area of the heat and mass exchanger ranged from 0.25 to 0.69 over the range of conditions tested in this study. Local mass transfer results indicate that water vapor is absorbed into the solution in the upper stages of the desorber leading to higher concentration ammonia vapor and therefore reducing the rectifier cooling capacity required. These experimentally validated results indicate that the microchannel geometry is well suited for use as a desorber. Previous experimental and analytical research has demonstrated the performance of this microchannel geometry as an absorber. Together, these studies show that this compact geometry is suitable for all components in an absorption heat pump, which would enable the increased use of absorption technology in the small capacity heat pump market.

1 INTRODUCTION

Concerns about the depletion of the ozone layer and global warming have generated renewed interest in absorption heat pumps in a variety of markets. Not only are the working fluids of most absorption systems benign with respect to ozone depletion, but also the ability to use waste heat as the driving force for space conditioning or refrigeration leads to increased energy savings. While there are numerous choices for absorption systems in the large capacity chiller market, there are far fewer choices of absorption systems for the residential and small commercial markets (10-50 kW).

Vapor compression heat pumps operate by circulating a refrigerant between a high and a low pressure side. The difference in pressure allows the phase transitions in the fluid to take place at appropriate temperatures to "pump" heat from a cold area, to a warmer area. Figure 1 shows a schematic of a simple vapor compression heat pump. Refrigerant vapor at a low pressure (1) enters the compressor where it is compressed to a higher pressure by a work input, W_{IN}. It then enters the condenser where it condenses, rejecting its latent heat $Q_{c,}$ to the hot ambient. After fully condensing (3) and undergoing some subcooling, the refrigerant passes through an expansion valve or other flow modulating device that reduces the pressure. The refrigerant then enters the evaporator (4), where it receives heat, Q_E from the controlled space. Once the refrigerant is fully evaporated, it is returned to the compressor (1), and the cycle continues. Vapor compression systems use electrical energy to drive the compressor, which then produces the desired cooling effect. Although the coefficient of performance (COP) of vapor compression systems is high, the losses associated with the generation and transmission of the electrical energy, typically from fossil fuels, lead to a low overall efficiency for

cooling. This dependence on electrical energy to provide cooling also results in high electricity demand periods, especially at the peak of the summer cooling season. Vapor compression systems also use synthetic refrigerants that have been shown to be detrimental to the ozone layer and also contribute to global warming.

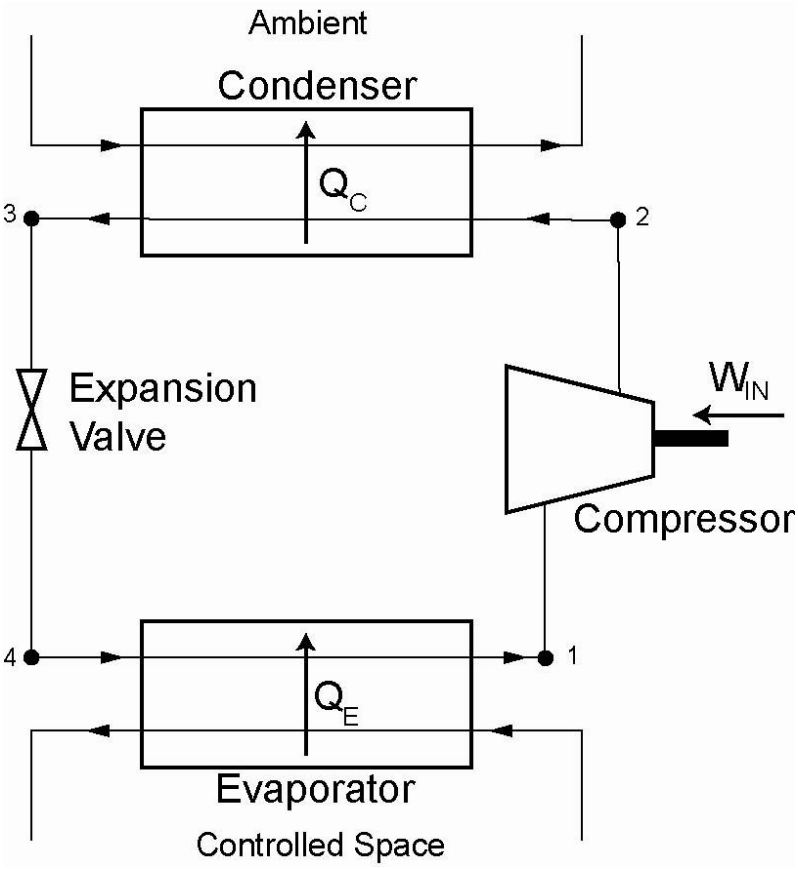

Figure 1 Vapor Compression Heat Pump

Absorption heat pumps use a condenser, throttling device and evaporator much like a vapor compression heat pump. The compressor, however, is replaced with an absorber, desorber, solution heat exchanger, throttling device and a pump. Figure 2 is a schematic of a simple absorption system. When the refrigerant vapor leaves the evaporator (1), it enters the absorber where it is absorbed into a liquid solution of refrigerant and absorbent. This absorption of the refrigerant into the absorbent releases a

large amount of heat, Q_A, which must be rejected to the ambient. The liquid solution is then pumped to the high pressure side (3), and passes through the solution heat exchanger on its way to the desorber recuperating some of the heat, Q_R, from the liquid stream of absorbent returning to the absorber from the desorber. Heat is supplied to the desorber, Q_D, to separate the refrigerant stream (5), from the solution stream (4), leaving behind a

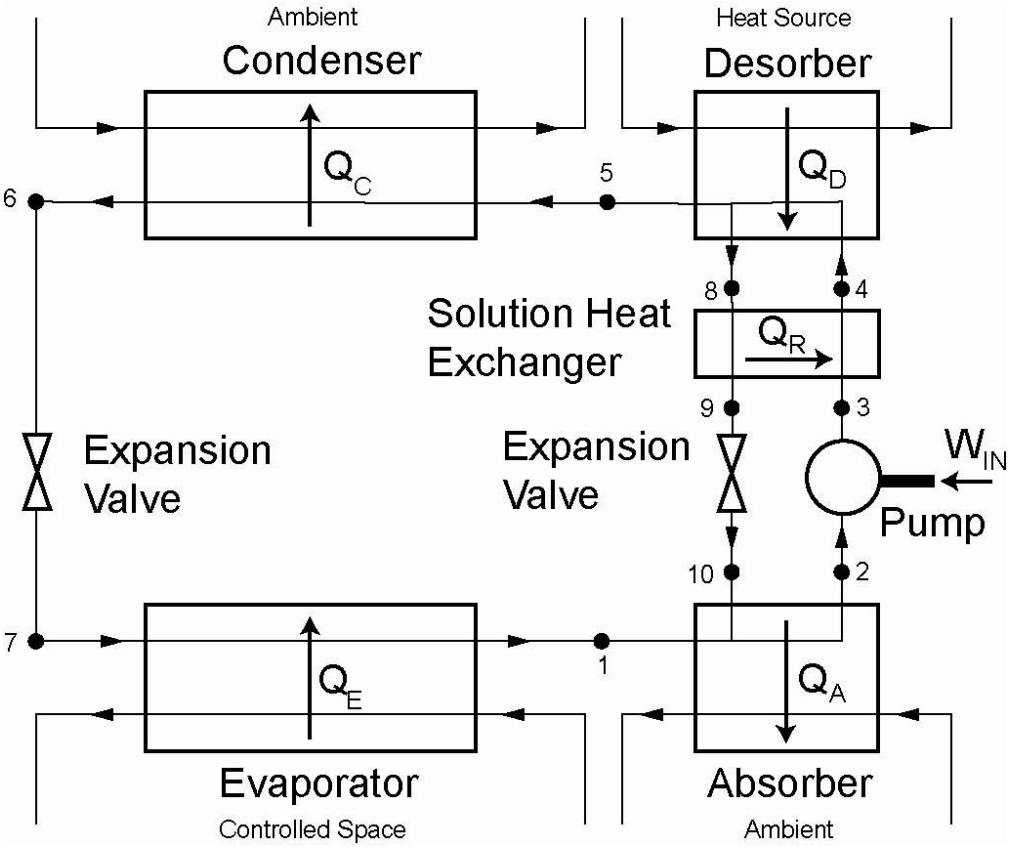

Figure 2 Absorption Heat Pump

refrigerant-poor absorbent stream (8).

The refrigerant vapor that is generated (5), flows to the condenser while the remaining solution of refrigerant and absorbent (8), flows through the solution heat exchanger and a throttling device, and then back to the absorber. In this manner, the

main source of energy used to produce the cooling effect is the heat supplied to the desorber, Q_D. This may be provided by the direct burning of natural gas or by a waste heat recovery system. The electrical energy supplied to the pump, W_{IN} is practically negligible compared to the energy required to run the compressor in a vapor compression system. Thus absorption heat pumps can alleviate the peak electrical demand during the summer months.

Another benefit of the absorption system is the use of non-ozone depleting and low global warming potential working fluid pairs, the most common of which are ammonia-water and water-lithium bromide. Vapor compression systems have long used halogenated refrigerants as their working fluids. Some of these refrigerants were cited as major contributors to the depletion of the earth's ozone layer. In response to this, the international community decided to act. The Montreal protocol, and its follow-on amendments, were enacted to limit the production of chlorofluorocarbon (CFC), hydrochlorofluorocarbons (HCFC) and halons (ASHRAE 2001). Other refrigerants that were not limited, such as hydrofluorocarbons (HFC), do not have the potential to destroy ozone, but are still considered detrimental to the environment due to their global warming potential. The ozone depleting potential (ODP) and the global warming potential (GWP) of several common refrigerants are listed in Table 1 (Wang 2001).

Table 1 Ozone Depletion Potential and Global warming Potential of Common Refrigerants (Wang 2001)

Refrigerant	Application	Ozone Depletion Potential	Global Warming Potential
HCFC			
R-22	Residential and Commercial Refrigeration	.05	0.34
CFC			
R-11	Centrifugal Chillers	1.0	1.0
R-12	Automobile Air Conditioning	1.0	3.1
HFC			
R-134a	Replacement for R-12	0.0	0.28
R-404a	Replacement for R-22	0.0	0.95
R-410a	Replacement for R-22	0.0	0.48
Inorganic Compounds			
R-717 (Ammonia)	Low Temperature Refrigeration/ Absorption Refrigerant	0.0	0.0

The most common absorption pairs are ammonia-water and water-lithium bromide. In the water-lithium bromide system, water is used as the refrigerant; therefore, the refrigeration temperature is limited to 0°C. Water-lithium bromide systems are generally used in water chilling applications for building air conditioning. Ammonia-water systems can be used for both air-conditioning systems as well as heat pump applications. The very low freezing temperature (-77°C) of ammonia also allows for the use of these systems in low temperature refrigeration applications. These refrigerants and absorbents do not contribute to the destruction of the ozone layer or to global warming.

The low first cost, high coefficient of performance and relative simplicity of vapor compression systems make the introduction of residential absorption systems that

much more difficult. For an absorption system to be practical in this market, the first cost must be lowered and the coefficient of performance increased.

The issue of increasing COP has been addressed over the years with ever more complicated thermodynamic cycles such as double-effect, triple-effect, GAX and others. While these systems do raise the COP, they necessitate the use of more heat exchangers and thus increase the first cost. For the more complex cycles to be practical, the heat and mass exchangers must be as efficient and small as possible. To that end, many investigations have been carried out to improve component level performance of absorption heat pumps. The present study investigates the potential of a microchannel heat and mass exchanger to be used as the desorber in a compact absorption heat pump system.

1.1 Scope of Current Research

The current work investigates a microchannel heat and mass exchanger (Garimella 2004) for use as the desorber in an ammonia-water absorption heat pump. This particular geometry has already proven successful when used as the absorber component (Garimella 1999, Meacham and Garimella 2002, 2003, 2004) in the heat pump. This configuration is ideal for use as a steam or liquid heated desorber in an absorption system, for example in a cogeneration system where the cooling fluid, carrying reject heat from the power generation system, is used as the heat source. This heat source is only at a moderate temperature, so it is essential to have a very efficient heat and mass exchanger. The same would be true if the system were driven by solar heat. The necessity for compactness is also a factor when considering absorption systems for use in residential and small commercial applications.

An experimental and analytical investigation of the microchannel desorber is conducted in this study. The experimental study investigated the effects of solution flow rate, vapor generation rate and heating fluid flow rate on the performance of the desorber. In addition, heat transfer rates were measured not only for the entire component but also on a segmental basis through the length of the desorber. These measurements were used to develop a model of the heat and mass transfer in the desorber on a segmental basis.

1.2 Thesis Organization

The organization of this thesis is as follows:

- Chapter 2 provides a brief review of the literature on experimental and analytical work on absorption heat pumps.
- Chapter 3 describes the prototype heat and mass exchanger investigated in this work.
- Chapter 4 describes the test facility used.
- Chapter 5 outlines the development of the heat and mass transfer model.
- Chapter 6 presents the results from the experiments on the desorber and the results of the heat and mass transfer model.
- Finally, Chapter 7 summarizes the important conclusions of this study.

2 LITERATURE REVIEW

This chapter briefly summarizes some of the more recent work done to increase the performance of absorption systems through modifications at the system level, and also to improve the efficiency and compactness of individual components in the absorption cycle. (Research on heat and mass transfer with additives and the effects of non-condensable gases is not addressed in this review.)

2.1 System Level Modeling

Several different computer modeling programs have been used to evaluate the performance of absorption heat pumps. Grossman *et al.* (1991) developed a modular absorption system simulation program (ABSIM) at Oak Ridge National Laboratory. Using this program, the components and the fluid interconnections are specified and the cycle COP and heat duties are computed. Individual component operating conditions are also computed. McGahey *et al.* (1994) developed a modified version of the ABSIM software (OSU-ABSIM) that incorporates additional fluid properties as well as the psychometric properties of moist air. The OSU-ABSIM software also included a burner module to account for the effect of burner heat transfer on cycle COP.

Gommed and Grossman (1990) used the ABSIM code to model several water-lithium bromide absorption heat pump configurations over a range of operating conditions. The heat pump configurations studied included a single-stage heat pump as well as 3 double-effect cycles, each employing a slightly different flow arrangement. For each of the systems, the effects of various system temperatures on the COP are discussed.

DeVault and Marsala (1990) evaluated the feasibility of three potential triple-effect cycles. It was found that the ammonia-water working fluid pair is only suitable for one of the configurations. The COP of the triple-effect cycle is compared with single and double-effect cycles at a standard rating condition. The triple-effect cycle has a COP of 1.41 as compared with the single-effect COP of 0.77 and the double effect COP of 1.20. The triple-effect cycle also had the added benefit of operating at a lower pressure than the corresponding double-effect cycle.

A 10 ton, double effect absorption heat pump with a working fluid pair of sodium thiocyanate-ammoina was modeled by McGahey *et al.* (1994) using the OSU-ABSIM software. The model was used to predict the performance of the heat pump in both the heating and cooling modes over an ambient range of -12.2-46.11°C (10-115°F). The burner efficiency was included in the model to provide a more realistic estimate of the COP. They predicted cooling mode COPs from 1.00 at 18°C (65°F) to 0.70 at 46.11°C (115°F) and heating mode COPs from 1.57 at 15.55°C (60°F) to 1.24 at -12.22°C (10°F).

Using the ABSIM code, Grossman *et al.* (1994) evaluated several water-lithium bromide triple-effect cycles. A standard rating condition was used, and the operating conditions were varied about that point to produce maps of the system COP over the range of operating conditions. Based on the internal flow arrangement of the cycle, the COP was found to vary between 1.272 and 1.729.

Ivester and Shelton (1994) conducted an analysis of the ammonia/water triple-effect system. The pinch concept was used to include the effects of finite heat exchangers. An optimal COP of 1.50 was found by holding constant the evaporator

temperatures and upper loop generator temperature, and varying the lower loop generator temperature.

Carmody and Shelton (1994) used a second law analysis to account for the irreversibility in each component of several direct fired absorption cycles. They determined that the component that causes the largest degradation in the cycle COP, for all of the cycles, was the generator. This can be attributed to the heat transfer from the high temperature combustion gasses to the lower temperature solution and flue losses.

Ziegler and Alefeld (1994) discuss the possibilities of increasing COP by using triple-effect and even quadruple-effect cycles. They use a superposition principle with the known cycle performance of elementary cycles to estimate the COPs of more complex cycles. This method is not restricted to any specific cycle configuration or fluid pair. They conclude that the COP may be increased to 1.8 for triple-effect systems and 2.0 for quadruple-effect systems.

Grossman *et al.* (1995) simulated the performance of a 4-effect, lithium bromide-water absorption chiller. The system was simulated using the modular ABSIM code. The COP of the 4-effect cycle is compared with that of a double-effect and a triple-effect cycle. For a constant chilled water temperature, 7°C, and various cooling water temperatures, the 4-effect cycle out-performs the triple-effect cycle when the heat supply temperature is above a certain value. The double-effect cycle performs best when the heat input is in the range 150-180°C. In the temperature range of 200-230°C, the triple effect cycle performs the best, and for temperatures greater than 230°C, the 4-effect system is the best choice. At the design point, the triple effect cycle COP was 1.724 and

the 4-effect cycle COP was 2.013. With some additional optimization of heat exchanger UAs, the 4-effect cycle COP was above 2.2.

Engler *et al.* (1996) conducted a study of 5 ammonia-water absorption cycles using the ABSIM computer code. The cycles included, in order of increasing complexity: basic single-effect, singe-effect with pre-cooler, single-effect with pre-cooler and two solution heat recoveries, GAX, and branched GAX. The heating mode and cooling mode COPs for each of the systems is reported over a range of ambient conditions. The GAX cycle is shown to out-perform the other cycles except at ambient temperatures where there is a loss of temperature overlap between the absorber and the desorber (> 55°C and < -6.6°C).

Garimella *et al.* (1996) analyzed an ammonia-water GAX heat pump using the OSU-ABSIM software. The cycle components were coupled to the conditioned space through secondary hydronic fluid loops as would be necessary to avoid having ammonia circulating through the conditioned space. The cooling mode COP at 35°C ambient was 0.925 and the heating mode COP was 1.51 at an ambient temperature of 8.3°C. Performance maps covering the entire range of ambient operating temperatures (-30°C to 46.1°C) were also developed. Garimella *et al.* (1997) also evaluated the triple-effect cycle that DeVault and Marsala (1990) had determined was feasible for ammonia-water. They studied the system with two sets of working fluids: ammonia-water in both the upper and lower cycles, and ammonia-water in the upper cycle and ammonia-sodium thiocyanate in the lower cycle. These two systems were modeled with the OSU-ABSIM software. The realistic gas burner model in OSU-ABSIM also accounted for flue gas losses. The analysis concluded that, due to several practical considerations concerning

intermediate fluid flow arrangements, the COP of the triple effect cycle was essentially the same as a double-effect cycle with equivalent heat exchanger size. However, the triple-effect cycle accomplished this with a substantially lower high cycle maximum pressure.

2.2 System Level Experiments

Serpente *et al.* (1994) designed and built a 2 kW lithium bromide absorption system. The design process included using general heat transfer correlations to size components. The design of the absorber included mass transfer considerations as well as incomplete wetting of tubes. The COP for various cycles employing different heat recovery techniques ranged from 0.642 to 0.743

A direct gas fired, ammonia-water absorption system was tested by Treffinger (1996) for use as a domestic water heater. The system was designed to provide a maximum heating capacity of 20 kW. Every effort was made to use standard components in the system so as to reduce manufacturing costs. The COP of the system was shown to vary between 1.4 and 1.7 over a range of ambient air temperatures (-10 to 10°C) and a range of hot water output temperatures (35 to 55°C).

Erickson *et al.* (1996) built a prototype GAX ammonia-water absorption system. The system was designed for a 17.59 kW (5 Ton) cooling load at 35°C ambient and the COP was rated at 0.88 at that temperature. At 27.8 C ambient, the cooling load was found to be 21.15 kW (6.7 Ton) and the cycle COP was 1.05. In the heating mode, the COP was found to be 1.77 at a lift of 48.1°C.

2.3 Component Level Modeling and Experimental Work

A comprehensive review of the modeling work on heat and mass transfer in absorption was presented by Killion and Garimella (2001). The review includes models developed for both volatile and nonvolatile absorbents, and addresses the various assumptions different studies have used. Some of their conclusions were that the film hydrodynamics are not accounted for in most models, the presence of wavy films is usually ignored, absorption in the pendant forming droplets is not accounted for, surface wetting effects are seldom accounted for, and experimental validation of models is very limited.

Killion and Garimella (2003) also presented a review of the experimental work on the absorption of water vapor into falling liquid films. They found a large body of work on the effects of surfactants, geometry and operating conditions on absorber performance. They concluded that droplet formation between the tubes has a substantial role in the total absorption process and that the film flowrate affects the droplet formation behavior as well as the fraction of the tube surface area that is wet by the film. They also found that the majority of studies reported only overall heat transfer coefficients. They suggest that a higher resolution of experimental data is required and that local heat and mass transfer rates need to be determined simultaneously because one process will not adequately reveal the details of the other. The use of surfactants always increased heat and mass transfer rates but the use of structured tubes could increase heat transfer while simultaneously decreasing mass transfer rates.

Perez-Blanco (1988) presented a model for ammonia/water falling film absorbers for laminar, steady flow at low Reynolds numbers. Uniform wetting of the tube was

assumed. The liquid mass transfer resistance was found to be the controlling resistance. To increase performance, they recommend periodic mixing of the film, the addition of surfactants, and the use of special surfaces that enhance mixing of the film at the vapor-liquid interface. The vapor heat transfer coefficient is also found to have an influence, and the authors recommend sweeping the liquid surface with high velocity vapor, which would help to remove non-condensables as well as cool the liquid surface.

The design, testing and performance analysis of two bubble absorbers is presented by Merrill *et al.* (1994). The absorbers were designed for a GAX load of 2.6 kW. The first absorber consisted of an inverted U shaped tube-in-tube heat exchanger. After initial tests indicated overall heat transfer coefficients in the range 902 -1147 W/m^2-K, and a lower than expected absorber load, a second absorber with several heat transfer enhancements was tested. The enhancements included internal spacers on the coolant side as well as surface roughness enhancements on the solution side. These enhancements resulted in an increase in the overall heat transfer coefficient to 2100-2767 W/m^2-K, but the absorber load still fell short of the design goal.

Kang and Christensen (1994) present a heat and mass transfer model for a GAX absorber in an ammonia-water system. The absorption takes place inside a vertical, fluted tube. The solution flows downwards, while the vapor flow upwards. A potassium carbonate solution, flowing counter current to the solution, is used to cool the absorber. Complete wetting of the tube wall by the solution is assumed. The mass transfer resistance of the vapor is found to be the controlling factor in determining heat exchanger size. The authors recommend maximizing the vapor velocity to increase the vapor mass transfer coefficient and thereby reduce the size of the component.

Both a vertical and a horizontal tube absorber were tested by Beutler *et al.* (1996) for use as a LiBr-Water absorber. In the horizontal tube absorber, the falling-film solution was observed to flow in discrete rivulets down the tube array. The area in between the rivulet is covered by a thin stagnant film. Because of the difficulty in determining the actual size of the non-participating area, the total surface area of the tubes is still used in the determination of the heat transfer coefficient.

The generator (desorber) and the rectifier of an absorption system are discussed in the context of fractionation columns by Herold and Pande (1996). In the analysis of such a column, the heat and mass transfer between the vapor and the liquid occur on incremental adiabatic plates. The heat to generate the vapor is added in a single plate at the bottom of the column and the heat to cool the rectifier is removed at a single step at the top of the column. They use the concept of chemical potential to describe the driving force for mass transfer, which allows them to avoid the assumption that the individual phases are saturated.

Potnis *et al.* (1997) simulated the performance of a GAX component that consisted of a helically wound fluted tube sandwiched between two shrouds. The high ammonia concentration solution flows upwards in the tube while the low concentration solution flows in a falling film over the outside of the tubes. The vapor flows upwards counter current to the falling film. The absorption heat and mass transfer is modeled by using the method developed by Colburn and Drew (1937) and Price and Bell (1974) for the condensation of mixed vapors. They have also included the liquid phase heat and mass transfer in the analysis. The liquid film thickness, and applicable heat and mass transfer coefficients are found from relevant correlations. The flow boiling side

coefficients are found to be 15 times greater than those on the absorption side. This indicates the absorption side is the controlling resistance to heat transfer and thus is the determining factor in heat exchanger size.

A numerical model of ammonia-water bubble absorption is presented by Merrill and Perez-Blanco (1997). In bubble absorption, small vapor bubbles are injected into the liquid, and flow upwards, eventually fully absorbing into the liquid. This method increases the vapor-liquid interfacial area per unit volume of vapor. The study solves the unsteady, two-dimensional problem of a single bubble being absorbed.

Kang *et al.* (1997) present a model for the analysis of all components in a ammonia-water heat pump. This study also uses the method from Colburn and Drew (1937); however, they assume that the mass transfer resistance within the liquid film is negligible. This analysis requires that suitable heat transfer coefficients are available for each of the specific components being examined. An algorithm is presented for the calculation of the heat and mass transfer on a segmental basis through the length of the component. The results of an analysis of a specific solution-heated desorber are presented. They present a composition map for ammonia-water heat pumps that illustrates what the composition of the condensing or evaporating flux will be for each of the components in the system.

Experimental work on a coiled tube ammonia-water absorber was carried out by Jeong *et al.* (1998). Experiments were conducted with and without absorption taking place. Heat transfer coefficients were higher for the case without absorption. The reduction in heat transfer coefficient during absorption was thought to be due to vapor shear at the liquid vapor interface that caused uneven distribution of the liquid.

Kang *et al.* (1999) conducted experiments on an ammonia-water, falling film, plate heat exchanger with enhanced surfaces. In this absorber, the vapor and liquid flow co-currently. They both flow cross/counter-current to the cooling fluid. The experiments revealed that rectification of the vapor occurred initially and then absorption proceeded after the bulk vapor concentration was above the equilibrium vapor concentration at the interface. This rectification was most likely due to the low vapor inlet concentration in this study (65-80%) and the inlet liquid subcooling. Water desorption was also present at the bottom of the absorber.

Garimella (1999) presents a heat and mass transfer model of an ammonia-water falling film absorber that utilizes small diameter tubes. The small diameter tubes provide high heat transfer coefficients on the coolant side, while the falling film mode provides large vapor/liquid transfer surface area and low pressure drops. The model follows the computational technique of Colburn and Drew (1937) and Price and Bell (1974). The absorber is sized for a residential absorption system and is analyzed on a row by row basis. The average solution falling film heat transfer coefficient is predicted to be 2790 W/m^2-K. It is noted that at some portions of the absorber, the mass transfer direction of water is opposite that of the ammonia indicating some local desorption, depending on the local gradients. This result has also been documented by Kang and Christensen (1994). This model was used to design a 0.476 x 0.127 x 0.127 m absorber with a surface area of 1.9 m^2 to transfer a 19.28 kW absorber load typical of residential heat pumps.

Meacham and Garimella (2002) conducted experiments on a microchannel, falling film, ammonia/water absorber. The absorber design was based on the analysis of Garimella (1999) and results were compared to that study. It was found that the

experimental heat transfer coefficients were somewhat lower than those predicted. It was suggested that liquid distribution problems were inhibiting the performance of the device.

Meacham and Garimella (2003) present a model of an ammonia-water absorber that was first developed by Garimella (1999), with a prototype tested by Meacham and Garimella (2002). The experimental results of Meacham and Garimella (2002) indicated that the performance of the prototype was less than had originally been expected. One of the reasons for the differences in transfer rates was that the prototype had 21% smaller heat transfer area than the original model. In addition, Meacham and Garimella (2003) also found that the solution was not distributed well over the tube bank due to poor design of the distribution device. They were able to account for this in their coupled heat and mass transfer model by introducing a surface wetting ratio, which resulted in good agreement between the model and the experimental results. The wetting ratio varied from 0.21 to 0.31 over the range of conditions analyzed. The heat duty transferred ranged from 4.86 to 16.23 kW with the overall heat transfer coefficients ranging from 133 to 403 W/m^2-K.

Meacham and Garimella (2004) also tested a second prototype absorber that was designed to reduce the solution flow distribution problems that were experienced previously. This second prototype absorber also had optical access to the heat transfer surface so that uniform flow distribution could be confirmed. Even though the second prototype had only 30% of the heat transfer area of the original prototype studied by them, it was able to transfer similar heat duties. The improved flow distribution was credited for the substantial increase in heat transfer performance. Solution side heat

transfer coefficients were reported in the range 638 – 1648 W/m^2-K and overall heat transfer coefficients ranged from 545 to 940 W/m^2-K.

Jeong and Garimella (2002) modeled heat and mass transfer in a lithium bromide-water, horizontal tube, falling-film absorber. They accounted for different flow regimes as well as incomplete wetting of the tubes. The absorber modeled in their study was based on the absorber that was experimentally investigated by Nomura *et al.* (1994) to facilitate model validation. The model assumes no sensible heating or cooling of the vapor from the liquid interface or the unwetted portion of the tubes. Results from this model were in excellent agreement with the work of Nomura *et al.* (1994). Furthermore they indicated that the wetting ratio for the study was between 0.6 to 0.8. The model was also able to predict the rise in solution temperature between adjacent tubes due to the adiabatic absorption of vapor during the droplet formation stage. The study concludes that the vapor is absorbed mainly in the falling-film and droplet-formation regimes and is negligible in the free-fall regime. At lower solution flow rates it was found that more vapor was absorbed in the falling-film regime than in the droplet-formation regime. The droplet-formation regime plays a more significant role as the solution flow rate increases.

Experiments on a horizontal tube, falling film absorber with the working pair lithium bromide-water were conducted by Frances and Ojer (2003). Through a visual study of the flow phenomena and a heat and mass transfer model that includes surface wetting effects, they conclude that assuming complete wetting of the tubes may lead to significant errors in performance predictions.

2.4 Need for Further Research

The majority of the component level investigations in the literature are focused on the performance of the absorber. There is a lack of information dealing with the performance of the generator/desorber. This component is critical, especially when the system is operating on low grade waste heat, and therefore more research is needed on this component. As noted in several of the studies presented above, inadequate liquid wetting of the heat transfer area results in severe degradation of heat and mass transfer. Even though the incomplete wetting of the heat transfer area has been well documented in experimental studies, the majority of analytical models of components still assume that the liquid film is uniformly distributed. This erroneous assumption may lead to significant errors when attempting to predict heat and mass exchanger performance. The present work attempts to develop an experimentally validated heat and mass transfer model of a microchannel ammonia-water desorber that also accounts for the incomplete wetting of the tubes.

3 PROTOTYPE DEVELOPMENT

3.1 Original Absorber Concept

The heat and mass exchanger under investigation was originally described by Garimella (1999), Garimella (2004). In its original configuration, a row of horizontal microchannel tubes is placed above a similar row of tubes but perpendicular to the row below it, as can be seen in Figure 3. The hydronic fluid flows in parallel through all the tubes in a row before being collected in a header and flowing up to the next row. Dilute solution enters the top of the array and flows downward in a falling film/droplet mode. The vapor enters the bottom of the absorber and flows upwards, due to buoyancy, while it is absorbed into the liquid. The resulting concentrated solution is removed from the bottom of the absorber.

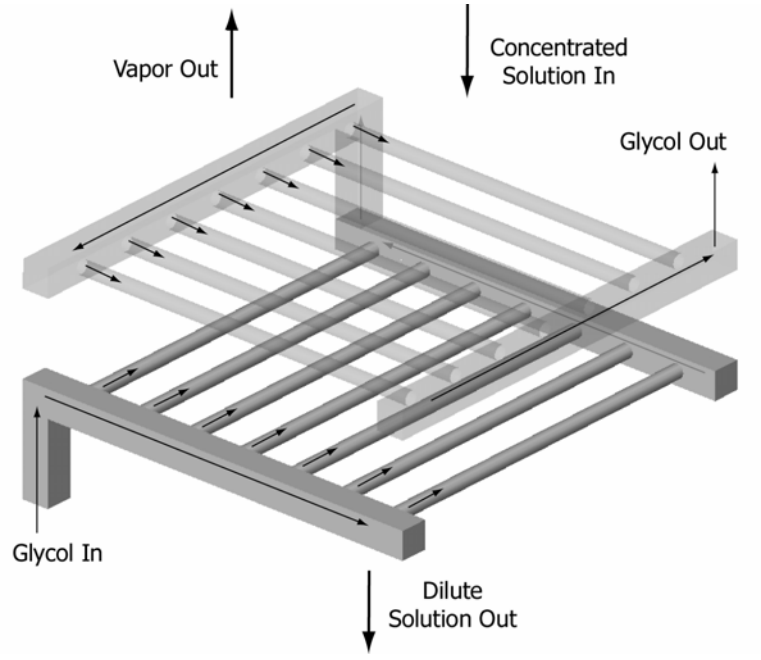

Figure 3 Microchannel Heat and Mass Exchanger Schematic (Desorber Flow Configuration)

In the desorber flow configuration, concentrated solution flows downwards over the tubes. As the vapor is produced, it flows upwards and is removed at the top of the desorber. The dilute solution is collected at the bottom of the desorber.

Hydronic fluid pressure drop is managed by flowing the fluid in parallel through several rows of tubes, referred to as a pass. The tube spacing in the vertical and horizontal directions was determined by using the criterion developed by Richter (1981) to avoid flooding, based on the Kutateladze number. The geometry used in the first absorption model is outlined in Table 2. This heat and mass exchanger geometry offers several key benefits. The falling film flow mode results in negligible pressure drop on the solution side while still maintaining high heat transfer coefficients. The tube-side pressure drop can be readily minimized by choosing the appropriate number of rows in each pass. With such small diameter tubes, it is possible to have relatively high heat transfer coefficients on the tube side while still in laminar flow. The droplet formation, fall and impingement also provide good liquid-vapor interaction and liquid mixing.

This absorber concept was analytically and experimental investigated by Meacham and Garimella (2003). The absorber geometry in their work was similar to that of the original concept as shown in Table 2. One of the conclusions of this work was that a poor liquid distribution system at the top of the tube array resulted in inadequate wetting of the tubes. In a subsequent investigation, Meacham and Garimella (2004) used a modified liquid distribution system consisting of a tray with tubes brazed vertically into the bottom. This forced the fluid to fall in droplets at discrete locations over the whole tube array instead of falling at some preferred location on the bottom of a flat distributor.

This study showed that an equivalent amount of heat (15 kW) could be transferred even with significantly less heat transfer area (0.456 m^2).

Table 2 Comparison of Dimensions of Heat and Mass Exchanger

	Garimella (1999)	Meacham and Garimella (2002) and Present Work
Function	**Absorber**	**Absorber and Desorber**
Tube outer diameter, mm	1.587	1.575
Tube inner diameter, mm	1.079	1.067
Tube wall material and conductivity, W/m-K	Carbon Steel, 60 W/m-K	T304 Stainless Steel, 15.4 W/m-K
Tube length, mm	127	140
Number of tubes per row	40	27
Number of tube rows	75	80
Number of rows per pass	15	16
Tube transverse pitch, mm	3.175	4.76
Row vertical pitch, mm	6.350	4.76
Absorber height, m	0.476	0.508
Total surface area, m^2	1.9	1.5

3.2 Conversion to Desorber

The heat and mass exchanger used as a desorber in this work is the exact same heat and mass exchanger used in the work of Meacham and Garimella (2002) (Figure 4). The only difference is in the flow distribution system and the enclosure. Based on the enhanced heat transfer performance resulting from the liquid distribution system in Meacham and Garimella (2004), a new liquid distribution tray was fabricated. The tray had short lengths (15.9 mm) of tubing, 1.27 mm OD, placed vertically in the bottom plate in a 4.76 mm by 4.76 mm pitch. Nine larger diameter (12.7 mm) tubes were also provided in the distribution tray to allow the rising vapor to pass through the tray and be removed from the top of the desorber (Figure 4d, e). These vapor bypass tubes were

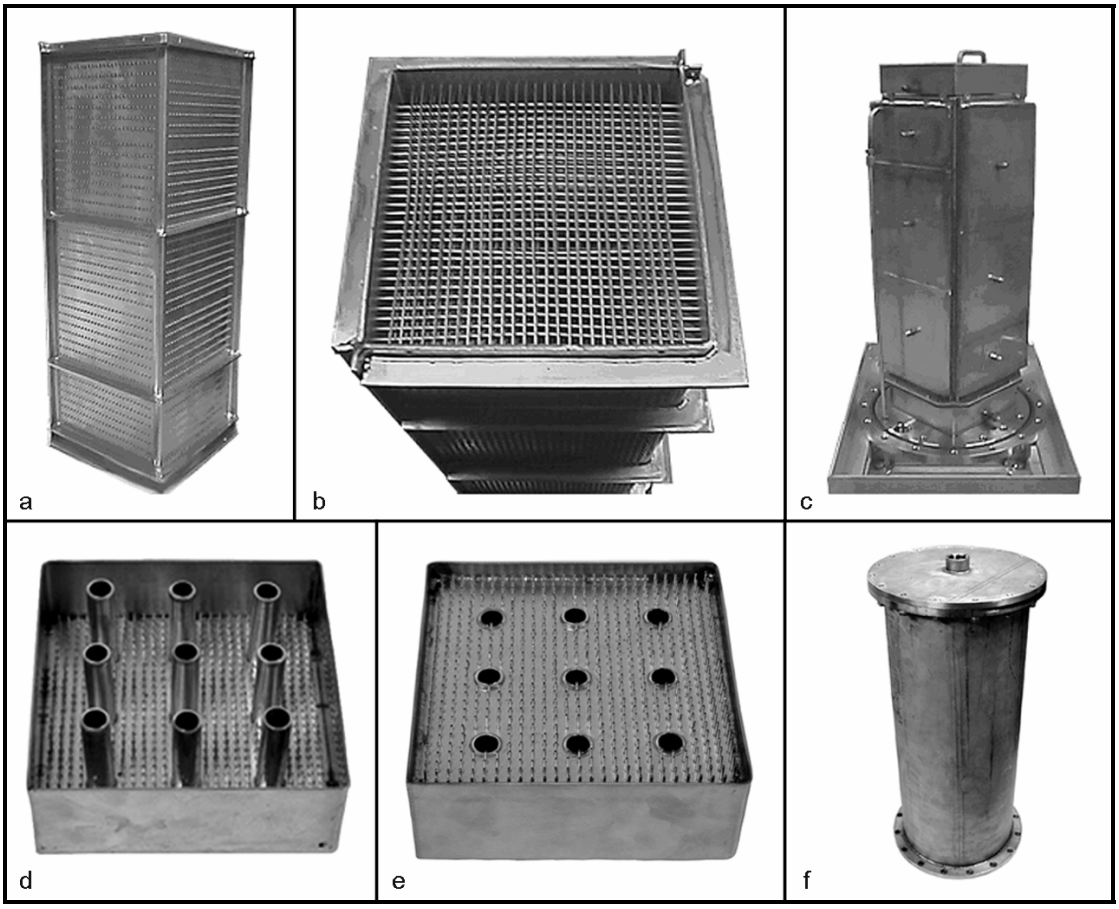

Figure 4 Photographs of the Desorber

taller than the sides of the tray to ensure the vapor would have a free path out of the desorber, and also to avoid concentrated solution flowing into these bypass tubes.

The original absorber design had a domed enclosure with all the liquid and vapor inlets and outlets on the bottom flange. A new enclosure with a top flange was fabricated for the desorption experiments. The top flange has a large tap so the vapor can be removed from the top of the desorber (Figure 4f). No changes were made to the heat and mass transfer surface area. The tube array, with fluid headers, has overall dimensions of 170 x 170 x 430 mm. The overall enclosure dimensions are 305 mm in diameter and 650 mm tall.

4 EXPERIMENTAL APPROACH AND DATA ANALYSIS

4.1 Test Facility Overview

A schematic of the heat and mass transfer test facility used for the investigation of this desorber is shown in Figure 5. A variable-speed pump delivers the desired concentrated solution flow rate to the solution heat exchanger where it is preheated before it enters the desorber. The concentrated solution then flows to the desorber where it is distributed uniformly over the tube array by the solution drip tray, and flows in the falling-film and droplet mode over the tubes. A glycol/water solution is first heated by condensing steam and then flows upward through the tube array in cross-counterflow with the falling solution.

Control of the condensing steam pressure allows for a range of desorption heat transfer rates. The glycol/water loop consists of a pump and a coiled tube-in-tube heat exchanger where steam is condensed to provide the desired heat input. As the ammonia vapor is desorbed, it flows upwards, countercurrent to the solution, and is removed at the top of the desorber. The resulting dilute solution is collected in a tray at the bottom of the desorber and then flows through the solution heat exchanger where it is subcooled by the concentrated solution that is on its way to the top of the desorber.

The solution heat exchanger recuperates some of the heat from the dilute solution stream, and also ensures that the dilute solution does not flash due to pressure drop as it flows through the mass flow meter. The vapor and dilute solution streams rejoin upstream of the coiled tube-in-tube absorber. The heat of absorption is removed by a closed cooling water loop which, in turn, is cooled by city water in the plate heat exchanger.

City and cooling water flow rate variations provide the requisite control of the absorber

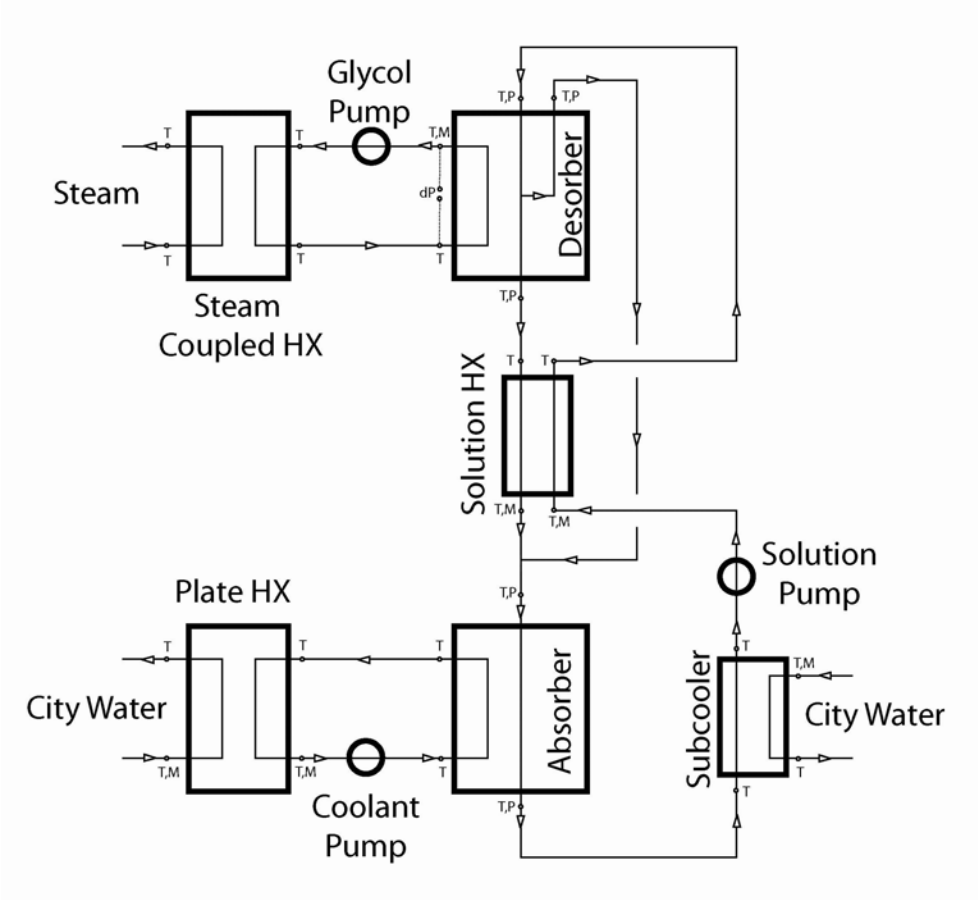

Figure 5 Heat and Mass Transfer Test Facility

heat sink. After exiting the absorber, the solution enters a shell-and-tube subcooler to ensure that the vapor has been completely absorbed into the solution before it returns to the solution pump. Figure 6 shows the complete absorption heat and mass transfer test facility.

Figure 6 Photographs of Desorber Test Facility

4.2 Test Facility Component Overview

The solution pump is a variable speed, gear pump made by MicroPump (Model # 415A). It has a maximum flow rate of 4.7×10^{-5} m^3/s, with a maximum operating pressure of 2.1 MPa and a maximum differential pressure of 345 kPa. The pump head contains an internal recirculation loop that may be used in conjunction with the variable speed controller. This allows for the pump to run at moderate speeds with only a small net flow rate in the system, providing a more consistent flowrate.

The solution heat exchanger is an Exergy Inc. single pass, counterflow, shell-and-tube heat exchanger (Model # 00256-3). The shell side is 38.1 mm in diameter with 9 baffles containing 55, 0.381 m long tubes. The tubes have an outside diameter of 3.2 mm and a wall thickness of 0.32 mm. The maximum operating pressures are 8.2 MPa and 5.5 MPa on the tube and shell sides respectively. The maximum allowable temperature difference between the fluids is 70° C. The dilute solution flows on the tube side and the concentrated solution flows on the shell side.

The glycol pump is a ¾ hp, Finish Thompson Inc., stainless steel centrifugal pump (Model # AC4STSIV35060015C015) with a maximum flow rate of 2.879×10^{-3} m^3/s, a maximum differential pressure of 176 kPa and a maximum fluid temperature of 150° C.

The glycol/steam heat exchanger and the absorber are both stainless steel coiled tube-in-tube heat exchangers from Exergy Inc. (Model # 00528). The inner tube has an outside diameter of 12.7 mm and a wall thickness of 1.65 mm. The outer tube outside diameter is 25.4 mm and the wall thickness is 1.65 mm. The total length of the tubes in the heat exchanger is 5.9 m. The maximum operating pressures are 13.8 MPa and 31

MPa for the outer and inner tubes respectively. In the glycol/steam heat exchanger, the glycol flows in the inner tube as the steam condenses in the annulus. In the absorber, the solution flows in the inner tube and the cooling water flows in counter flow in the annulus.

The cooling water pump is a ¾ hp, Little Giant Pump Co. centrifugal pump (Model # TE-7-MD-HC) with a maximum flow rate of 4.0×10^{-3} m^3/s and a maximum differential pressure of 176 kPa.

The plate heat exchanger is a Tranter, Inc. Superchanger (Model # UX-016-UU-21) with a maximum operating pressure of 1.0 MPa at 93°C, and a total heat transfer area of 1.65 m^2.

The solution subcooler is an Exergy Inc. shell and tube heat exchanger (Model # 00256-2). The shell side is 38.1 mm in diameter with 7 baffles. There are 55, 0.254 m long tubes in a single pass, with an outside diameter of 3.2 mm and a wall thickness of 0.32 mm. The maximum operating pressures are 8.2 MPa and 5.5 MPa on the tube and shell sides respectively and the maximum allowable temperature difference between the fluids is 70° C.

4.3 Instrumentation and Data Acquisition

Temperature, pressure, and mass flow rate measurement locations are shown in Figure 5. Mass flow measurements of the concentrated solution and dilute solution are made with Micromotion coriolis flow meters (Model # CMF025M319NU, ±0.15% uncertainty). The vapor flow rate is determined by the difference of the concentrated and dilute solution flow rates. The absorber cooling water flow rate is measured with a Rosemount magnetic flow meter (Model # 8712C, ±0.5% uncertainty). The glycol/water

flow rate is measured with Micromotion coriolis flow meters (Model # CMF100M329NU, ±0.15% uncertainty). Absolute pressure measurements of the solutions and vapor are made using Rosemount transducers (Model # 2088) with uncertainties of ±0.25% of span. The tube-side pressure drop in the desorber is measured with a Rosemount differential pressure transducer (Model # 3051, ±0.075% of span). Type T thermocouples (±0.5°C uncertainty) are used to measure the glycol/water temperatures in the headers of the desorber, as well as the solution temperatures in the solution drip tray and collection tray. The remaining solution temperatures, as well as the glycol/water temperatures and the absorber cooling water temperatures are measured with RTDs (±0.5°C to ±0.8°C uncertainty). The city water temperatures are measured with type T thermocouples. A TEMPSCAN data acquisition system records all measured data for near real-time data analysis. Plots of the temperatures and pressures versus time are used to ensure that steady state conditions are reached before data for any test condition are recorded.

4.4 Operating Procedures

Whenever operating with ammonia, extreme caution must be used to avoid injury. A Lumidor Safety Products ammonia gas detector is installed near the test facility at all times with the alarm set to sound at an ammonia concentration of 25 ppm. When ammonia is being charged and discharged from the loop, the operator wears a full face gas mask with chemical cartridges approved for ammonia and methylamine. When operating the facility, the user must always wear safety goggles. The test facility is kept under a fume hood that is operated whenever ammonia is present in the loop. Curtains surround the test facility when it is not in operation.

To initiate testing, all of the city water and cooling water loops are first turned on and the appropriate flow rates are set. Next the glycol/water loop pump is turned on and the flow rate is adjusted to the desired test condition. The steam lines are then opened and a steam pressure regulator is used to set the desired steam pressure. For several minutes the steam lines only flow condensate. By carefully monitoring the temperature of the entering steam, the user can determine when all of the condensate in the steam lines has been purged. Once the steam is flowing, the glycol loop temperatures as well as the pressures on the ammonia-water side begin to rise. Once the pressure in the system begins to rise, the solution pump is turned on and slowly brought up to the desired flow rate. As the system approaches the desired test conditions, the cooling water flow rates and temperatures are monitored and adjusted as needed to ensure sufficient temperature rises in the heat exchangers to minimize uncertainty in heat duty calculations. Plots of key temperatures and pressures versus time are monitored continuously to ensure the system is at steady state before data are recorded for each test point.

After the final experiment for each test session, the steam pressure is reduced in several increments and finally the steam supply valve is closed. The glycol/water loop continues to gain heat as it passes through the steam heat exchanger until all of the steam finally condenses. Once the temperature of the glycol/water loop begins to decrease the pressure in the ammonia-water loop begins to decrease and the solution flow rate may begin to be decreased. As the system cools, the ammonia-water solution tends to collect in the bottom of the desorber. All the flow control valves should be opened wide to allow the solution to flow back to the absorber and solution pump. Once it is insured that the difference between the concentrated ammonia solution flowrate and the dilute solution

ammonia flowrate is minimal, it is concluded that vapor generation has ended, and the solution pump is turned off. The cooling water flows are kept running until the solution temperatures and pressures have returned to their values when the system is at equilibrium with the ambient.

4.5 Overall Heat Duty Analysis

Using Engineering Equation Solver (EES), (Klein 2004), temperature and pressure measurements of the dilute solution and vapor leaving the desorber were used to determine the concentrations at these saturated states as follows.

$$y_{des,out} = f\left(T_{des,v,out}, P_{des,v,out}, q_{des,v,out} = 1\right) \tag{4.1}$$

$$x_{des,out} = f\left(T_{des,s,out}, P_{des,s,out}, q_{des,s,out} = 0\right) \tag{4.2}$$

These concentrations, as well as the measured solution flow rates were used to determine the concentration of the entering solution.

$$x_{des,in} = \frac{\dot{m}_{des,s,out} \cdot x_{des,out} + \dot{m}_{des,v,out} \cdot y_{des,out}}{\dot{m}_{des,s,in}} \tag{4.3}$$

Once the concentrations were determined, temperatures and pressures at the desorber inlet and outlet were used to determine the enthalpy at each location and then the solution-side heat duty, as shown below.

$$\begin{aligned} h_{des,s,out} &= f\left(T_{des,s,out}, P_{des,s,out}, x_{des,s,out}\right) \\ h_{des,s,in} &= f\left(T_{des,s,in}, P_{des,s,in}, x_{des,s,in}\right) \\ h_{des,v,out} &= f\left(T_{des,v,out}, P_{des,v,out}, x_{des,v,out}\right) \end{aligned} \tag{4.4}$$

$$\dot{Q}_{des} = \dot{m}_{des,s,out} \cdot h_{des,s,out} + \dot{m}_{des,v,out} \cdot h_{des,v,out} - \dot{m}_{des,s,in} \cdot h_{des,s,in} \tag{4.5}$$

The temperatures and flow rate of the glycol-water solution were also used to calculate the heat duty, to help establish an energy balance between the two sides of the desorber.

$$\dot{Q}_{des} = \dot{m}_{glyc} \cdot c_{p,glyc} \left(T_{des,glyc,in} - T_{des,glyc,out} \right) \tag{4.6}$$

Once the desorber heat duty was known, the log-mean temperature difference (LMTD) between the solution and the heating fluid was used to calculate the overall heat transfer coefficient (U). The saturation temperature of the inlet solution was used to better represent the driving force for heat transfer.

$$LMTD_{des} = \frac{\left(T_{des,glyc,in} - T_{des,s,out} \right) - \left(T_{des,glyc,out} - T_{des,s,in,sat} \right)}{\mathrm{Ln}\left[\frac{\left(T_{des,glyc,in} - T_{des,s,out} \right)}{\left(T_{des,glyc,out} - T_{des,s,in,sat} \right)} \right]} \tag{4.7}$$

$$\dot{Q}_{des} = U \cdot A_{des,OD} \cdot LMTD_{des} \tag{4.8}$$

The flow of the glycol-water solution in the tubes was laminar for all cases, which resulted in a constant Nusselt number of 4.364. The corresponding heat transfer coefficient was calculated as follows:

$$\alpha_{glyc} = \frac{Nu_{glyc} \cdot k_{glyc}}{D_{ID}} \tag{4.9}$$

The wall thermal resistance was calculated as follows:

$$R_w = \frac{D_{OD}}{2 \cdot k_w} \ln\left[\frac{D_{OD}}{D_{ID}} \right] \tag{4.10}$$

The solution-side desorption heat transfer coefficient was then calculated from the measured U, using a resistance network approach as follows.

$$\alpha_{des,s} = \frac{1}{\left(\frac{1}{U} - \frac{D_{OD}}{D_{ID}\alpha_{glyc}} - R_w\right)} \tag{4.11}$$

An error propagation technique described by Taylor and Kuyatt (1994) was used to estimate the uncertainty in the solution-side heat transfer coefficient. At a representative point with a concentrated solution flow rate of 0.0264 kg/s, a vapor flow rate of 6.80×10^{-3} kg/s and a glycol/water flow rate of 0.153 kg/s, the uncertainties in the measured temperature and pressure values used to determine concentrations yield: x_{con}=0.4793±0.0021, x_{dil}=0.3049±0.0025, and y_{vap}=0.9832±0.0006. These values, combined with the uncertainties of the flow rate, temperature and pressure measurements, yield a solution side heat duty of 13.09±0.35 kW. The corresponding glycol/water-side heat duty is 12.93±0.36 kW, which results in an average desorber heat duty of 13.01±0.25 kW. This heat duty and an LMTD of 17.6±0.6°C yield an overall U of 493.9±20 W/m^2-K. The tube-side heat transfer coefficient, α_t, with an assumed uncertainty of ±25%, is calculated to be 1419±354 W/m^2-K. Finally, the solution-side heat transfer coefficient is calculated to be α_s = 1037±293 W/m^2-K, i.e., with an uncertainty of 28%.

5 HEAT AND MASS TRANSFER MODEL

The overall heat duty analysis of the previous section provides an estimate of the total heat transfer performance of the desorber. In an attempt to better understand the heat and mass transfer processes taking place, a model was developed to calculate heat and mass transfer rates on an incremental basis through the desorber. This model is then validated by comparing the calculated values with those obtained from the experimental study.

5.1 Transport Properties

5.1.1 Liquid Properties

The liquid surface tension, viscosity and thermal conductivity are calculated using curve fit equations to the ammonia-water property plots in Herold *et al.* (1996). The specific heat is calculated from the difference in enthalpy with a temperature change at constant pressure. The Prandtl number is given by:

$$\mathrm{Pr}_l = \frac{\mu_l c_{p,l}}{k_l} \tag{5.1}$$

5.1.2 Vapor Properties

The Chapman-Enskog kinetic theory of gasses, as outlined by Mills (1995) is used to evaluate the mixture vapor transport properties. This model is for monatomic gasses but may also be used, as it is here, for polyatomic gasses without introducing significant error. Using the Lennard-Jones potential model to describe the interaction of two molecules, the viscosities of each individual component are calculated as follows:

$$\mu_i = 2.67 \times 10^{-6} \frac{\sqrt{M_i T}}{\sigma_i^2 \Omega_\mu} \tag{5.2}$$

Where M is the molecular weight, T is the absolute temperature, σ is the collision diameter in Angstroms, and Ω_μ is the collision integral.

The thermal conductivity of a monatomic gas is given by:

$$k_i = 5/2 \, c_{v,i} \cdot \mu_i \tag{5.3}$$

The constant volume specific heat is:

$$c_{v,i} = \frac{3}{2} \frac{R}{M_i} \tag{5.4}$$

Substituting into equation (5.3) for the viscosity and the constant volume specific heat yields the translational thermal conductivity for a monatomic gas.

$$k_{i,translational} = 8.32 \times 10^{-2} \frac{\sqrt{T/M_i}}{\sigma_i^2 \Omega_k} \tag{5.5}$$

The collision integral for thermal conductivity is equal to the collision integral for viscosity. To correct the thermal conductivity for a polyatomic gas, the Eucken correction is added.

$$k_i = k_{i,translational} + 1.32 \left(c_{p,i} - \frac{5}{2} \frac{R}{M_i} \right) \mu_i \tag{5.6}$$

The constant pressure specific heat is:

$$c_{p,i} = \left(5 + N_r\right) \left(\frac{1}{2} \frac{R}{M_i} \right) \tag{5.7}$$

Here, N_r is the number of rotational degrees of freedom. Both ammonia and water have 3 degrees of rotational freedom.

Once the viscosity and thermal conductivity of each species has been determined, the properties of the mixture may be determined using the mixture rules from Wilke (1950) as follows:

$$\mu_{v,mix} = \sum_{i=1}^{n} \frac{x_i \mu_i}{\sum_{j=1}^{n} x_j \Phi_{ij}} \tag{5.8}$$

$$k_{v,mix} = \sum_{i=1}^{n} \frac{x_i k_i}{\sum_{j=1}^{n} x_j \Phi_{ij}} \tag{5.9}$$

$$\Phi_{ij} = \frac{\left[1 + \left(\frac{\mu_{v,i}}{\mu_{v,j}}\right)^{1/2} \left(\frac{M_j}{M_i}\right)^{1/4}\right]^2}{\sqrt{8}\left[1 + \left(\frac{M_i}{M_j}\right)\right]^{1/2}} \tag{5.10}$$

The specific volume of the mixture is calculated from the known temperature, pressure and concentration. The specific heat of the mixture is found from the enthalpy difference over a 1°C temperature change. The mixture Prandtl number is given by:

$$\mathrm{Pr}_{v,mix} = \frac{\mu_{v,mix} c_{p,mix}}{k_{v,mix}} \tag{5.11}$$

The binary diffusion coefficient is given by:

$$D_{aw,v} = 1.86 \times 10^{-7} \frac{\sqrt{T^3 \left(\frac{1}{M_a} + \frac{1}{M_w}\right)}}{\sigma_{aw}^2 \Omega_D P} \tag{5.12}$$

where the pressure, P, is in atmospheres. The Lennard-Jones collision diameter, σ_{aw}, for the mixture is found from the following empirical relation:

$$\sigma_{aw} = \frac{1}{2}\left(\sigma_a + \sigma_w\right) \tag{5.13}$$

5.2 Ammonia-Water Heat and Mass Transfer Coefficients

The heat transfer to the liquid falling over the tubes is modeled by using the following correlation developed by Wilke (1962)

$$Nu_l = 0.029 \cdot \mathrm{Re}^{0.533} \cdot \mathrm{Pr}^{0.344}, \quad \left(\mathrm{Re} < 400\right) \tag{5.14}$$

The Reynolds number is defined as follows:

$$\mathrm{Re}_l = \frac{4\Gamma_l}{\mu_l} \tag{5.15}$$

where Γ_l is the mass flowrate of liquid per wetted length of tube. The liquid Reynolds number ranged from 36 to 487 in this study. For the 7 passes in this study where the Reynolds number was greater than 400 the Wilke (1962) correlation was extrapolated. The liquid film heat transfer coefficient is then calculated as follows:

$$\alpha_f = \frac{Nu_l \cdot k_l}{\delta_f} \tag{5.16}$$

The liquid film thickness δ_f is calculated as:

$$\delta_f = 0.8434 \cdot \mathrm{Re}^{1/3} \left(\frac{\nu_L^2}{g}\right)^{1/3} \tag{5.17}$$

As the vapor is generated from the falling liquid film, it flows upward around the tubes and liquid film. The heat transfer to the film is modeled using a correlation for crossflow heat transfer to a fluid from a bank of tubes. For this correlation the maximum velocity is calculated as follows:

$$V_{\max,v} = \frac{\dot{m}_v}{\rho_v \cdot A_{free}} \tag{5.18}$$

The vapor Reynolds number is based on this maximum vapor velocity and the outside diameter of the tubes. Thus,

$$\mathrm{Re}_{\max,v} = \frac{\rho_v \cdot V_{\max,v} \cdot D_{OD}}{\mu_v} \tag{5.19}$$

The Churchill and Bernstein (1977) correlation developed for heat transfer from a tube in crossflow is used to calculate the Nusselt number as follows:

$$Nu_v = 0.3 + \frac{0.62 \cdot \mathrm{Re}_{\max,v}^{1/2} \cdot \mathrm{Pr}_v^{1/3}}{\left[1+\left(0.4/\mathrm{Pr}_v\right)^{2/3}\right]^{1/4}} \left[1+\left(\frac{\mathrm{Re}_{\max,v}}{282000}\right)^{5/8}\right]^{4/5}, \quad \left(\mathrm{Re}\cdot\mathrm{Pr} > 0.2\right) \tag{5.20}$$

The vapor Reynolds number-Prandtl number product ranged from 1.3 to 60.4 in this study. The heat transfer coefficient is then calculated as follows:

$$\alpha_v = \frac{Nu_v \cdot k_v}{D_{OD}} \tag{5.21}$$

Using a heat and mass transfer analogy, the vapor-phase Sherwood number is evaluated as follows:

$$Sh_v = Nu_v \left(\frac{Sc_v}{\mathrm{Pr}_v}\right)^{1/3} \tag{5.22}$$

where Sc_v is the vapor Schmidt number.

The vapor mass transfer coefficient is then determined as follows:

$$\beta_v = \frac{Sh_v \cdot D_{12,v}}{D_{OD}} \tag{5.23}$$

5.3 Glycol Heat Transfer Coefficient

The glycol Reynolds number, $Re_g = (\rho V_{g,avg} D_{ID}/\mu_g)$ is less than 2300 for all cases in the current study, which results in a constant Nusselt number, $Nu_{glyc} = 4.364$. The glycol heat transfer coefficient is calculated from the Nusselt number as follows:

$$\alpha_{glyc} = \frac{Nu_{glyc} \cdot k_{glyc}}{D_{ID}} \tag{5.24}$$

5.4 Overall Heat Transfer

At any given instant in the desorption process, the tube wall can either have a film of liquid surrounding it, or be in direct contact with the vapor. Therefore, the heat transferred to a given section of the desorber can be divided into two parts; a) glycol-tube wall-liquid film and b) glycol-tube wall-vapor (Figure 7). Several temperature profiles are shown on Figure 7 to illustrate the possible heat transfer paths. These two portions can be accounted for by introducing a wetting ratio,

$$a = \frac{A_{pp,eff}}{A_{pp}} \tag{5.25}$$

in which A_{pp} is the total area of the tubes per pass, based on the outside diameter, and $A_{pp,eff}$ is the tube area per pass that is wetted.

The outer tube wall temperature is first calculated as follows:

$$R_{glyc} = \frac{D_{OD}}{D_{ID} \cdot \alpha_{glyc} \cdot A_{pp}} \tag{5.26}$$

$$R_{wall} = \frac{D_{OD}}{2 \cdot k_w \cdot A_{pp}} \ln\left[\frac{D_{OD}}{D_{ID}}\right] \tag{5.27}$$

$$\dot{Q}_{glyc} = \left(\frac{1}{R_{wall} + R_{glyc}} \right) \cdot \left(T_{glyc,ave} - T_{wall} \right) \tag{5.28}$$

Heat transfer between the wall and the liquid is calculated based on the thermal resistance of the solution film as follows:

$$R_{l,f} = \frac{1}{\alpha_{f,l} \cdot a \cdot A_{pp}} \tag{5.29}$$

$$\dot{Q}_{wet} = \left(\frac{1}{R_{l,f}} \right) \cdot (T_{l,ave} - T_{wall}) \tag{5.30}$$

The flow regime is assumed to induce a completely mixed liquid phase and therefore the liquid average temperature and liquid surface temperature are equal. The corresponding

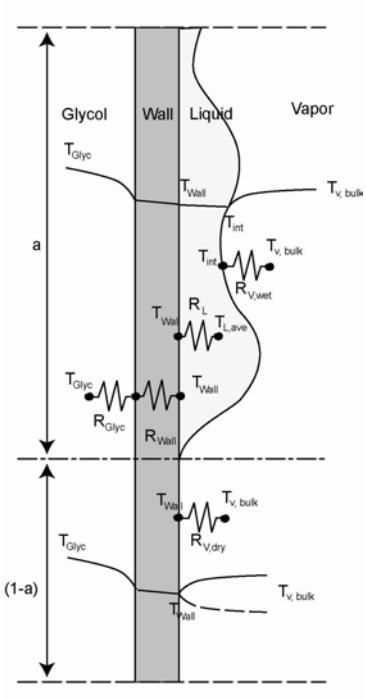

Figure 7 Illustration of Wetted and Non-Wetted Wall

heat transfer through the dry portion of the wall is calculated by using the thermal resistance of the vapor film.

$$R_{v,dry} = \frac{1}{\alpha_v \cdot (1-a) \cdot A_{pp}} \tag{5.31}$$

$$\dot{Q}_{dry} = \left(\frac{1}{R_{v,dry}} \right) \cdot \left(T_{v,bulk} - T_{wall} \right) \tag{5.32}$$

The total heat transfer from the glycol to the solution side is given by:

$$\dot{Q}_{seg} = \dot{Q}_{wet} + \dot{Q}_{dry} \tag{5.33}$$

In general the vapor temperature will always be higher than the liquid temperature so there will be heat transfer from the vapor to the liquid. The vapor temperature will be lower than the outer tube wall temperature in some segments of the desorber and will be higher than the wall temperature in other segments. Therefore the heat transfer direction between the vapor and the dry tube wall will be different for various data points and even may be different in adjacent passes due to the local wetting ratio and heat transfer variations. The heat transfer from the vapor to the liquid will be more substantial than the heat transfer from the dry wall to the vapor because of the larger temperature difference between the vapor and the liquid than between the vapor and the dry wall.

5.5 Vapor Phase Transport Equations

In accordance with the assumption made by Price and Bell (1974) and prior work on the absorption function of the device by Meacham and Garimella (2002), it is assumed that the liquid phase is well mixed and presents negligible resistance to mass transfer. The interface mass transfer may therefore be described by assuming that the major

resistance to mass transfer is in a small film in the vapor. The total molar flux of ammonia may then be written as:

$$\dot{n}_a = -C_T \cdot D_{aw,v} \frac{d\tilde{y}}{d\eta} + \dot{n}_T \tilde{y} \tag{5.34}$$

where ỹ is the vapor, molar concentration of ammonia. The condensing or evaporating flux, z̃ can be defined as follows:

$$\tilde{z} = \frac{\dot{n}_a}{\dot{n}_T} = \frac{\dot{n}_a}{\dot{n}_a + \dot{n}_w} \tag{5.35}$$

Rearranging and integrating over the film thickness yields:

$$\dot{n}_T = -\frac{C_T D_{aw,v}}{\delta_{v,f}} \ln\left[\frac{\tilde{z} - \tilde{y}_{\text{int}}}{\tilde{z} - \tilde{y}_{bulk}}\right] \tag{5.36}$$

The vapor interface concentration is found by assuming that the vapor and liquid are in equilibrium at the interface. The mass transfer coefficient may be introduced as follows:

$$\beta_v = \frac{D_{aw,v}}{\delta_{v,f}} \tag{5.37}$$

The total flux is then given by:

$$\dot{n}_T = -C_T \beta_v \ln\left[\frac{\tilde{z} - \tilde{y}_{\text{int}}}{\tilde{z} - \tilde{y}_{bulk}}\right] \tag{5.38}$$

The individual species fluxes are calculated as follows:

$$\dot{n}_a = \tilde{z} \cdot \dot{n}_T \tag{5.39}$$

$$\dot{n}_w = (1 - \tilde{z}) \cdot \dot{n}_T \tag{5.40}$$

Depending on the local temperature and concentration gradients, the value of z̃ may be greater than one, in which case the water mass flux is in the opposite direction as that of the ammonia.

The sensible heat transfer to the vapor is composed of two parts; the heat transferred directly to the vapor through the portion of the un-wetted wall, and the heat that is transferred from the vapor to the liquid film. The heat transfer from the vapor to the liquid film is represented by;

$$\frac{\dot{Q}_{v\to l}}{A_{pp,eff}} = \left(\dot{n}_a \cdot \tilde{c}_{p,a} + \dot{n}_w \cdot \tilde{c}_{p,w}\right)\left(T - T_{\text{int}}\right) + \alpha_v \frac{dT}{d\eta} \tag{5.41}$$

The first term in the above equation represents the bulk vapor flow, while the second term represents the heat conducted through the vapor film. Upon rearrangement and integration over the film, the heat transfer from the vapor to the liquid becomes:

$$Q_{v\to l} = \alpha_v \left[\frac{\phi_T}{e^{\phi_T} - 1}\right] \cdot A_{pp,eff}\left(T_{v,bulk} - T_{\text{int}}\right) \tag{5.42}$$

In the above equation, the term in brackets represents the correction to the heat transfer coefficient due to the effect of mass transfer. This correction is in terms of:

$$\phi_T = \frac{\left(\dot{n}_a \cdot \tilde{c}_{p,a} + \dot{n}_w \cdot \tilde{c}_{p,w}\right)}{\alpha_v} \tag{5.43}$$

The heat transfer between the vapor and the dry wall was given previously as Q_{dry}. The total sensible heat transfer is then the sum of the two individual parts.

$$\dot{Q}_v = \dot{Q}_{v\to l} + \dot{Q}_{dry} \tag{5.44}$$

This heat transfer rate is used to calculate the change in vapor temperature over the segment of the desorber as follows:

$$\dot{Q}_v = \dot{m}_{v,avg} \cdot c_{p,v} \cdot \left(T_{v,o} - T_{v,i}\right) \tag{5.45}$$

5.6 Mass and Concentration Balances

A mass and species balance on the solution side of a segment of the desorber yields:

$$\dot{m}_{l,in} + \dot{m}_{v,in} = \dot{m}_{l,out} + \dot{m}_{v,out} \tag{5.46}$$

$$\dot{m}_{l,in} \cdot x_{l,in} + \dot{m}_{v,in} \cdot y_{v,in} = \dot{m}_{l,out} \cdot x_{l,out} + \dot{m}_{v,out} \cdot y_{v,out} \tag{5.47}$$

A mass and species balance on the vapor in the segment yields:

$$\dot{m}_{v,out} = \dot{m}_{v,in} + \dot{m}_{des,T} \tag{5.48}$$

$$\dot{m}_{v,out} \cdot y_{v,out} = \dot{m}_{v,in} \cdot y_{v,in} + \dot{m}_{des,a} \tag{5.49}$$

5.7 Energy Balance

An energy balance on the solution side of the desorber yields:

$$\dot{Q}_{seg} = \dot{m}_{l,out} \cdot h_{l,out} + \dot{m}_{v,out} \cdot h_{v,out} - \dot{m}_{l,in} \cdot h_{l,in} - \dot{m}_{v,in} \cdot h_{v,in} \tag{5.50}$$

The heat transferred by the glycol is calculated as follows:

$$\dot{Q}_{seg} = \dot{m}_{glyc} \cdot c_{p,glyc} \cdot \left(T_{glyc,in} - T_{glyc,out} \right) \tag{5.51}$$

These equations are solved simultaneously and a consistent solution is obtained when all three of the segment heat duties are equal (Equations (5.33), (5.50), (5.51)). The outlet conditions of the segment are then used as the inlet conditions of the next segment, and the calculations are repeated for all the segments in the desorber.

6 RESULTS AND DISCUSSION

6.1 Experimental Results

The effects of the concentrated solution flow rate and the vapor fraction on the desorber heat duty, overall heat transfer coefficient, and solution-side heat transfer coefficient are illustrated in Figures 8, 9 and 10, respectively. All three figures indicate that the solution mass flow rate has the largest impact on the performance of the desorber. The desorber heat duties increase from 5.37 kW to 17.46 kW as the solution flow rate increases from 0.0188 kg/s to 0.0339 kg/s. Over the range of test conditions, the overall heat transfer coefficient increases roughly linearly with the concentrated solution flow rate, ranging from a minimum of 388 W/m^2-K at 0.0188 kg/s to a maximum of 617 W/m^2-K at a concentrated solution flow rate of 0.0351 kg/s. Similarly, the experimental results indicate that the solution-side heat transfer coefficient varies from 659 to 1795 W/m^2-K over the range of conditions tested, with one outlier among the data being 2560 W/m^2-K. These heat transfer coefficients are much higher than those obtained by Meacham and Garimella (2002) ($145 < \alpha_{des,s} < 510$ W/m^2-K) when they tested this same component as an absorber (presumably due to the solution distribution problems they encountered as noted in Chapter 2.) It should be noted that in the second version of the absorber tested by them (Meacham and Garinella 2004), the solution heat transfer coefficient range was $638 < \alpha_{des,s} < 1648$ W/m^2-K, which is almost exactly the same as the range obtained in the present study. Of course, here, the process under consideration is desorption rather than absorption, and also there are geometric differences between the revised absorber tested by Meacham and Garimella (2004) and the desorber tested in the

present study. But it is clear that essentially the same design as the first absorber prototype tested by them with a change in the dripper tray design results in a

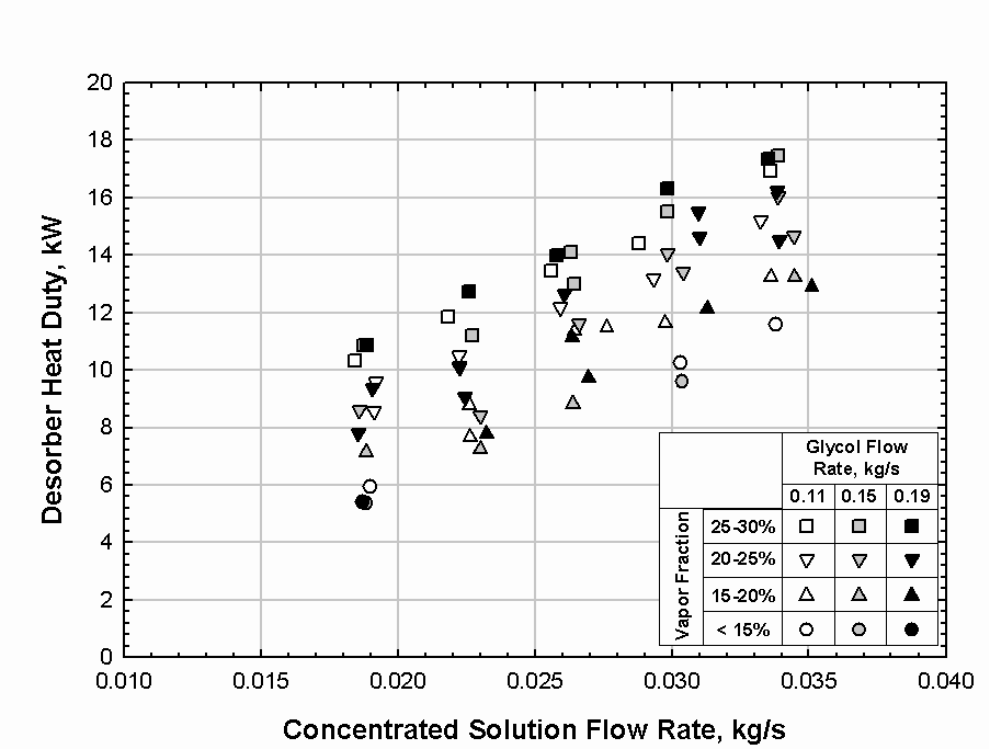

Figure 8 Desorber Heat Duty

configuration that functions extremely well as a desorber.

Tube-side heat transfer coefficients are relatively constant ($1396 < \alpha_{glyc} < 1466$ W/m^2-K) for the conditions tested in this study due to the flow being laminar ($145 < Re_{glyc} < 455$) throughout the experiments. It should be noted that in spite of laminar flow, due to the small diameter tubes, this α_{glyc} is relatively high, with the tube-side resistance constituting between 40 and 65 percent of the total thermal resistance.

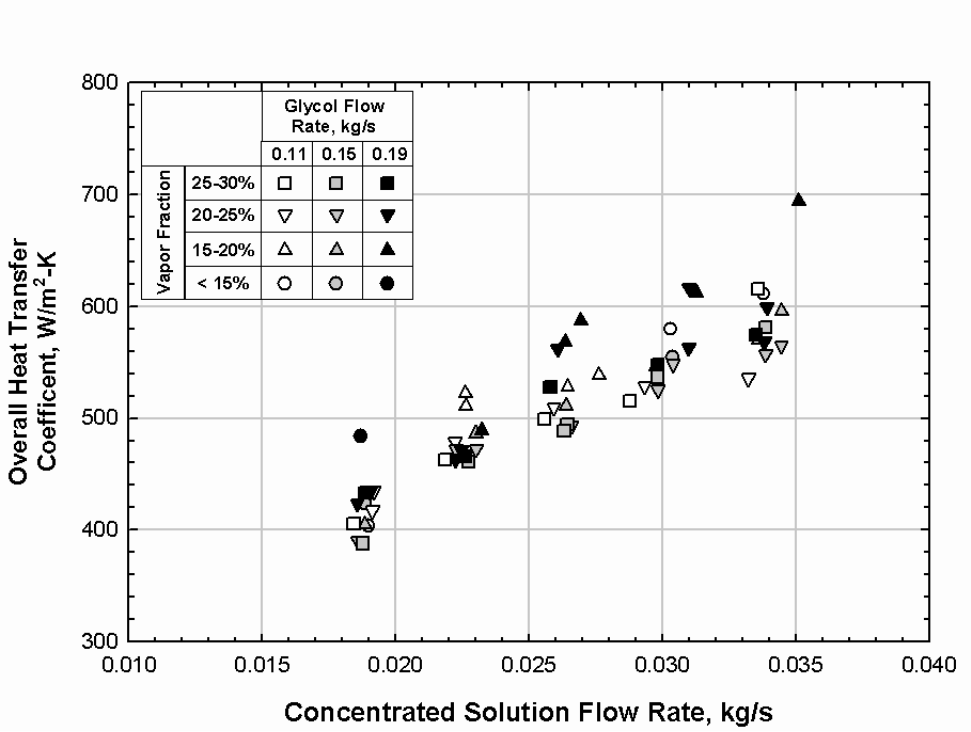

Figure 9 Overall Heat Transfer Coefficient

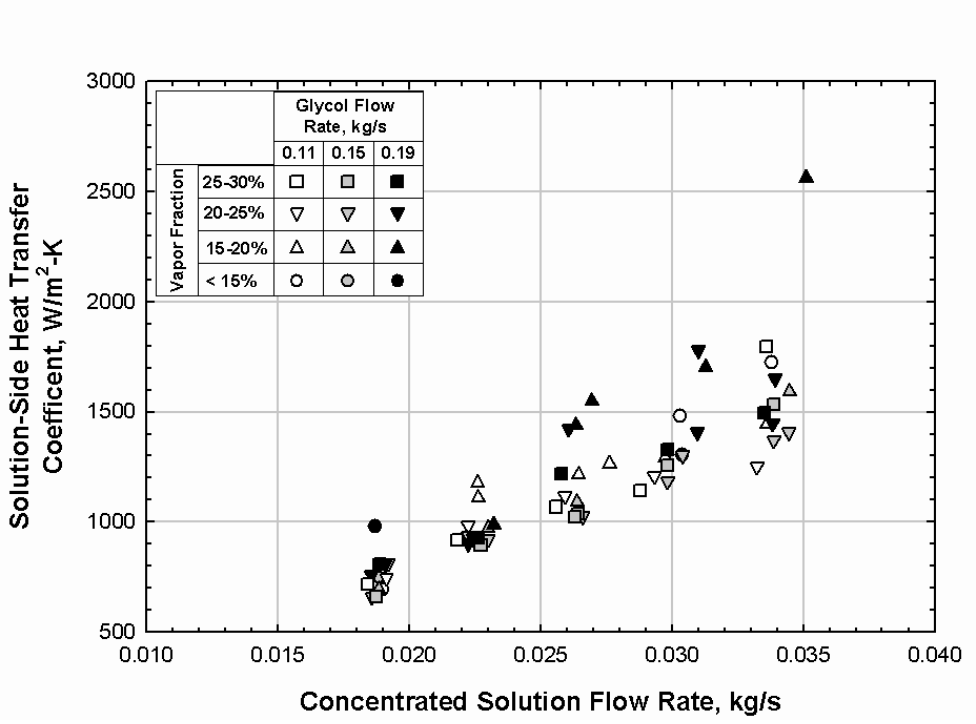

Figure 10 Solution-Side Heat Transfer Coefficient

Thus, the desorber is solution-side limited at the low solution flow rates, while at the high end of the ammonia-water solution flow rate, the ammonia-water heat transfer coefficient is high enough that the tube-side resistance is not negligible. This is illustrated by the increase in performance with an increase in solution flow rate, and a somewhat smaller dependence of the overall heat transfer coefficient on the coolant flow rate.

Figure 8 also shows an increase in heat duties at higher vapor fractions. This is of course because additional heat input is required to generate more ammonia vapor at the same concentrated solution flow rate. The overall U and solution-side heat transfer coefficient are less sensitive to vapor fraction (within the limits of experimental uncertainty), with no clear trend emerging in Figures 9 and 10. This is perhaps because the vapor-side velocities and more importantly, the vapor-phase resistance, does not change appreciably in the range of conditions tested. It should also be noted that constant vapor *fraction* cases in fact imply an increasing vapor *flow rate* as the solution flow rate increases. Thus, some of the increase in solution-side heat transfer coefficient that is seen in Figure 10 could perhaps be attributed to the simultaneous increase in vapor flow rate (at the same vapor generation fraction.)

The tube-side pressure drop in these tests varied from 11.4 kPa at a coolant flow rate of 0.113 kg/s to 29.6 kPa at 0.189 kg/s (Figure 11). It should be noted that a considerable portion of this pressure drop can be attributed to small lines leading to and from the tube lattice within the desorber. These extraneous losses were calculated to be 3.2 to 8.7 kPa over the range of conditions tested, representing approximately 30% of the total pressure drop. Thus, the heat and mass transfer performance achieved in this study

was obtained with low coolant pressure drops in spite of the use of extremely small diameter tubes, due to the parallel pass arrangement chosen.

The results of this experimental investigation indicate that this miniaturized heat and mass transfer technology is capable of transferring heat duties representative of those found in residential absorption heat pump applications.

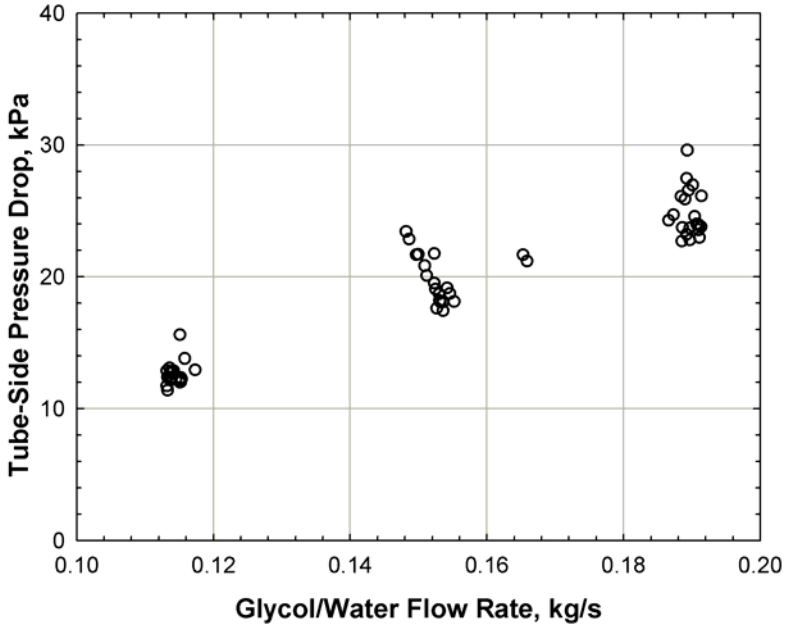

Figure 11 Glycol-Water Pressure Drop

6.2 Model Results

The experimental results presented above were further analyzed on a segmental basis to understand the details of the heat and mass transfer process within the desorber. Such an analysis is useful because of the ability to track variations in heat and mass transfer coefficients as well as the corresponding heat duties and desorption rates along the length of the heat and mass exchanger. In the analysis of the experimental data, temperature, pressure, concentration and flow rates at the inlet and outlets of the desorber

were used to estimate the overall heat transfer coefficient. In this segmental analysis, the outlet conditions of the liquid solution, the glycol inlet temperature as well as the measured glycol header temperatures, are used to calculate the inlet solution and outlet vapor conditions of each section. These values are then used as the starting conditions at the next segment of the desorber. These computations yield the local heat and mass transfer coefficients, as well as the wetted area fraction.

The model temperature profiles of the glycol, liquid solution and vapor for a representative data point, are shown in Figure 12. It can be seen that the model slightly over predicts the liquid solution inlet temperature at the top header (6). This is because the model assumes a saturated inlet condition (T = 57.6°C), while in fact the liquid enters the desorber at a slightly subcooled state (T = 53.94°C). The saturation temperature of the actual experimental conditions (T = 58.78°C) is almost the same as the temperature predicted by the model. The vapor temperature is under predicted by the model. The predicted vapor temperature at the desorber outlet is 61.21°C while the actual temperature was 68.39°C. However, it should be noted that because of the relatively low mass flow rate and specific heat of the vapor, this temperature discrepancy represents an error in heat duty on the order of 90 Watts. Compared to the overall heat duty of the desorber (11.1 kW), this is a relatively small (0.8%) error.

The pass heat duties (Figure 13) are plotted based on *measured* glycol temperatures at inlet/outlet headers of each pass. It can be seen that the heat transfer rate is the highest at the top of the desorber, decreases toward the middle, and rises again at the bottom-most pass.

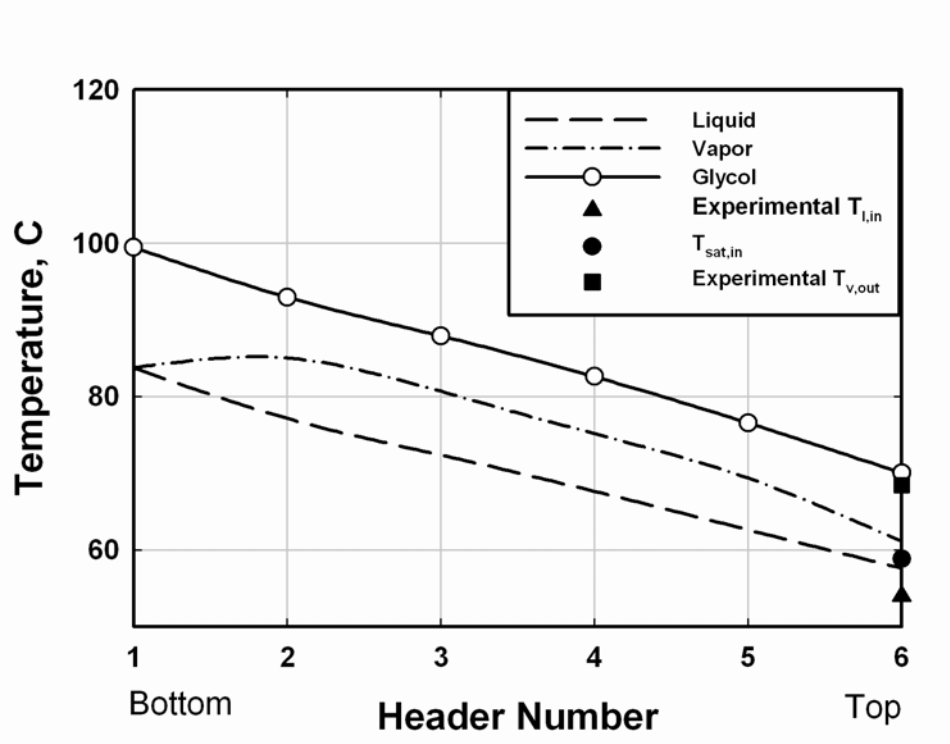

Figure 12 Desorber Temperature Profiles

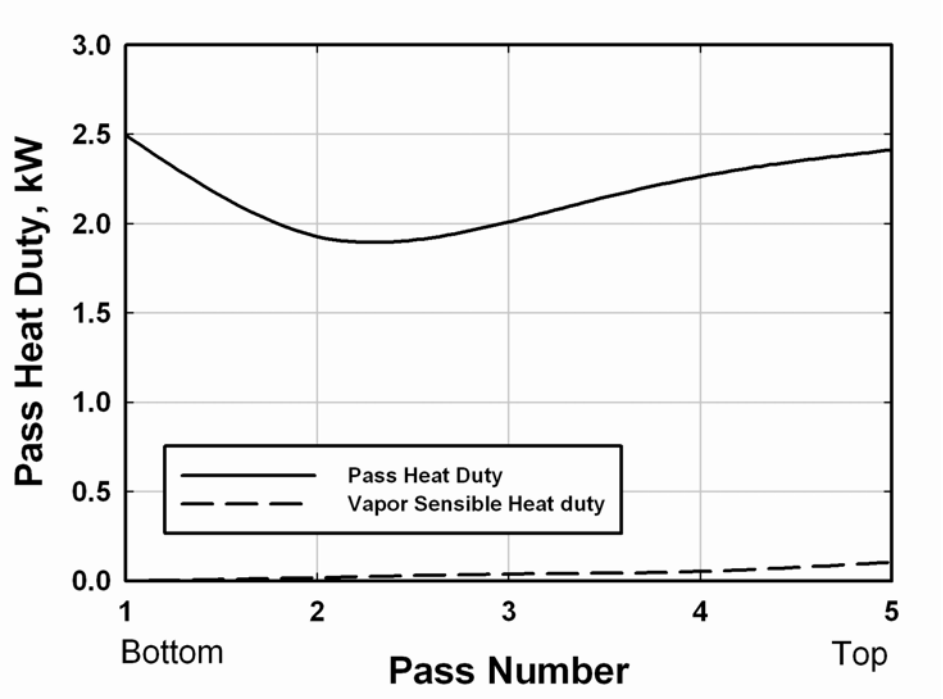

Figure 13 Pass Heat Duties

These results can be interpreted as follows. The measured temperature drops in the glycol, which correspond to the pass heat duty, are 6.5, 6.0, 5.3, 5.1, 6.5°C from the top to the bottom, respectively. The decreasing heat duty per pass in the first four passes appears to be the result of several competing factors as seen in figure 14. As the liquid film flows down the tube array, the total liquid flow rate is decreasing due to the vapor generation. The liquid, however, could also be coalescing into rivulets, partly due to surface tension, thus reducing the wetted area of the tubes. Based on the measured pass-by-pass glycol temperatures, the wetted area ratio required for model closure (Figure 15) decreases from 0.82 in the top pass to 0.24 at the fourth pass. The consolidation of the liquid film into rivulets, and therefore, the increased mass flux for a given mass flow rate, tends to

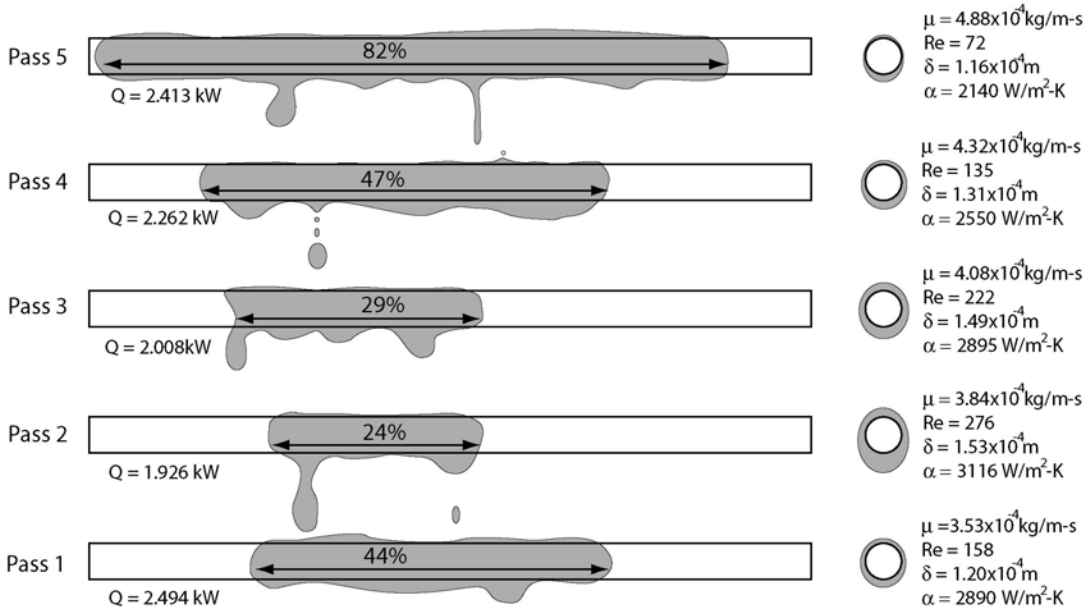

Figure 14 Model Overview

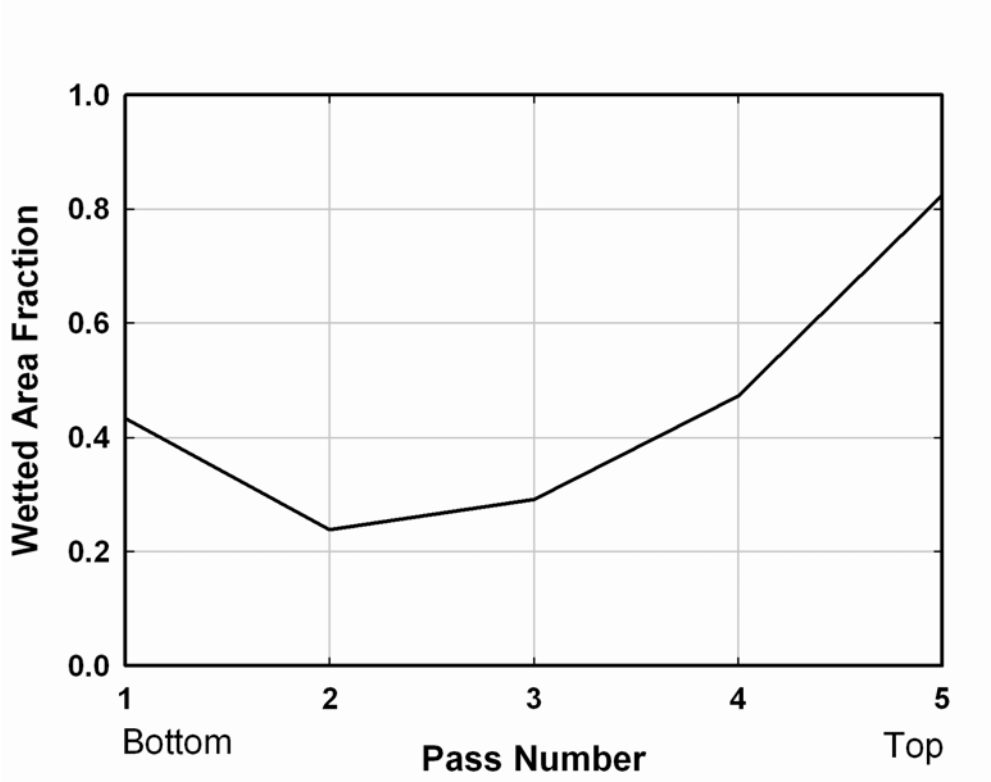

Figure 15 Wetted Area Fractions by Pass

decrease in the wetted area would also increase the liquid film thickness, which would contribute to a decrease in the heat transfer coefficient. It appears that the Reynolds number plays the more dominant role here, and the film heat transfer coefficient increases from 2140 to 3116 W/m^2-K from the top pass to the next to bottom pass, and then decreases in the final pass to 2890 W/m^2-K. It should be pointed out, however, that even though the heat transfer coefficient is the highest in the fourth pass, the overall heat duty of this pass is the lowest among all passes. This is due to the fact that the wetted area is the smallest in this pass and therefore there is the least amount of heat transfer area

between the tubes and the liquid film. This illustrates that increasing the liquid film heat transfer coefficient alone is an insufficient design goal for falling-film heat and mass exchangers. The wetted area ratio plays a major role in the total heat and mass transfer rates and therefore the size of the device. The average wetted area fraction over the entire desorber for this case is 0.45. Over the range of conditions investigated in this study, the average wetted area fraction ranged from 0.25 to 0.69.

The increasing wetted area fraction at the bottom pass is more difficult to explain. This increase in wetted area is substantiated by the corresponding increase in pass heat duty near the bottom of the desorber (Figure 13). It should be noted that pass-by-pass duties were in fact measured using glycol temperatures, thus these predictions have a basis in the actual measured quantities. It is possible that the lower solution flowrates and lower counter current vapor velocities at the bottom of the desorber result in thinner solution films that also spread over the tubes more uniformly. Figure 16 shows the average wetted area fraction for all 60 data points analyzed in this study versus the concentrated solution flowrate. It can be seen that increasing the solution flow rate leads to larger wetted areas. Figure 17 shows the pass wise variation in wetted area fractions for a representative data point at each of the 5 nominal solution flow rates. All of these cases show the same general behavior and the increase in wetted area fraction with increasing solution flowrates is evident. For the cases with higher flowrates, the area fraction actually approaches 1 in the upper-most pass.

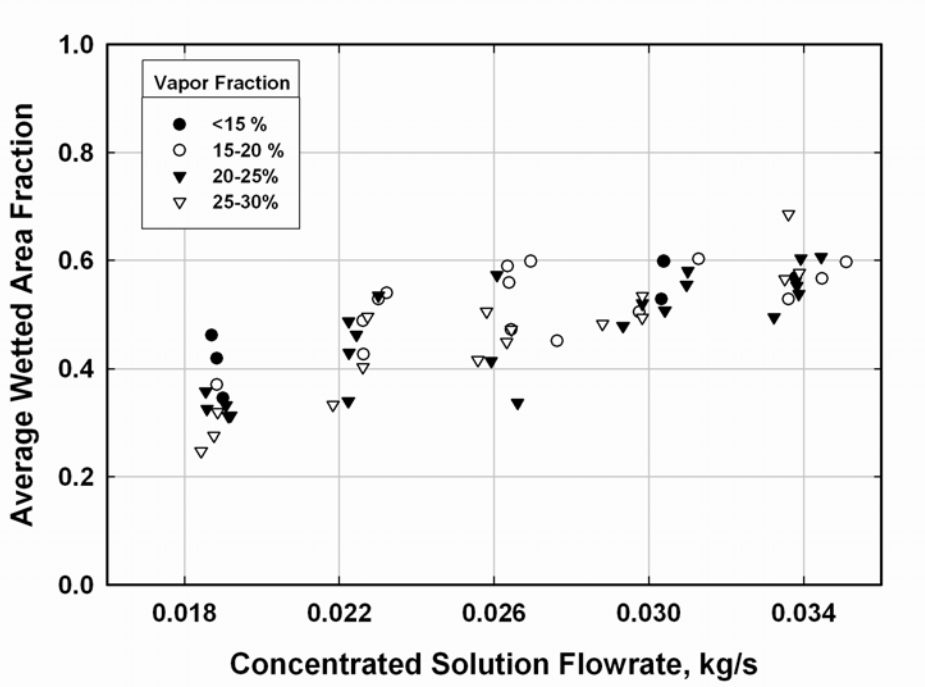

Figure 16 Average Wetted Areas for the Present Study

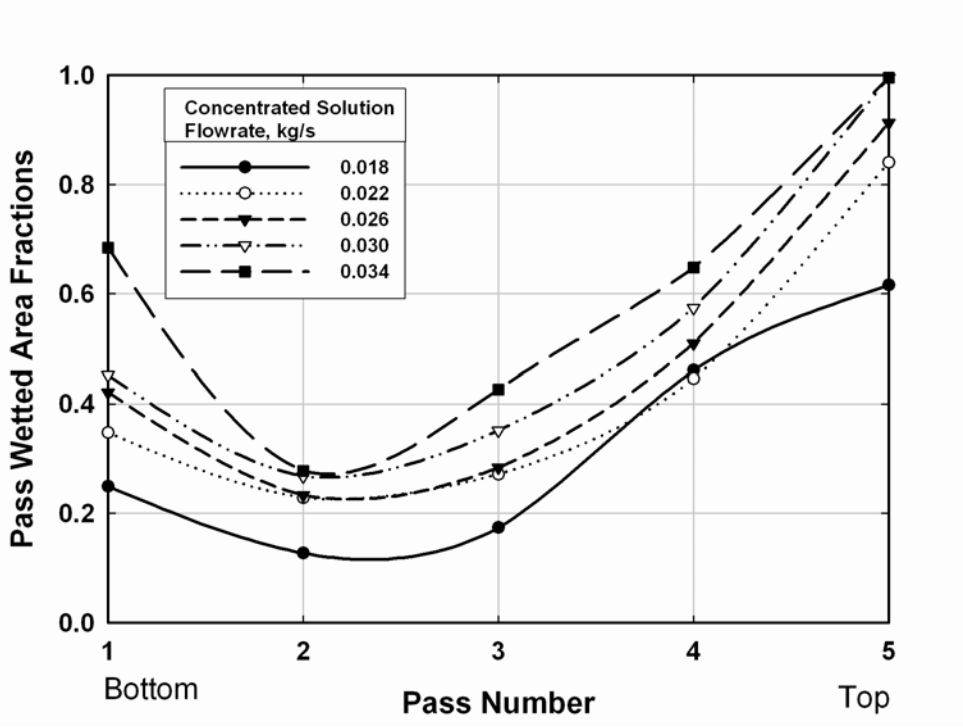

Figure 17 Wetted Area Fractions by Pass for Representative Points

Another potential explanation is that when the glycol solution entering at the bottom makes the first bend to enter the next pass, some tube side mal-distribution is introduced, which reduces local desorption rates, and is erroneously reflected as smaller wetted area fractions. Additional local solution-side and glycol-side measurements and flow visualization studies could confirm this interpretation.

Figure 18 shows the prediction of the concentration profiles along the desorber while Figure 19 shows the prediction of the mass flow rates. The model predictions are in excellent agreement with the concentration and flow rates of both the incoming solution as well as the existing vapor.

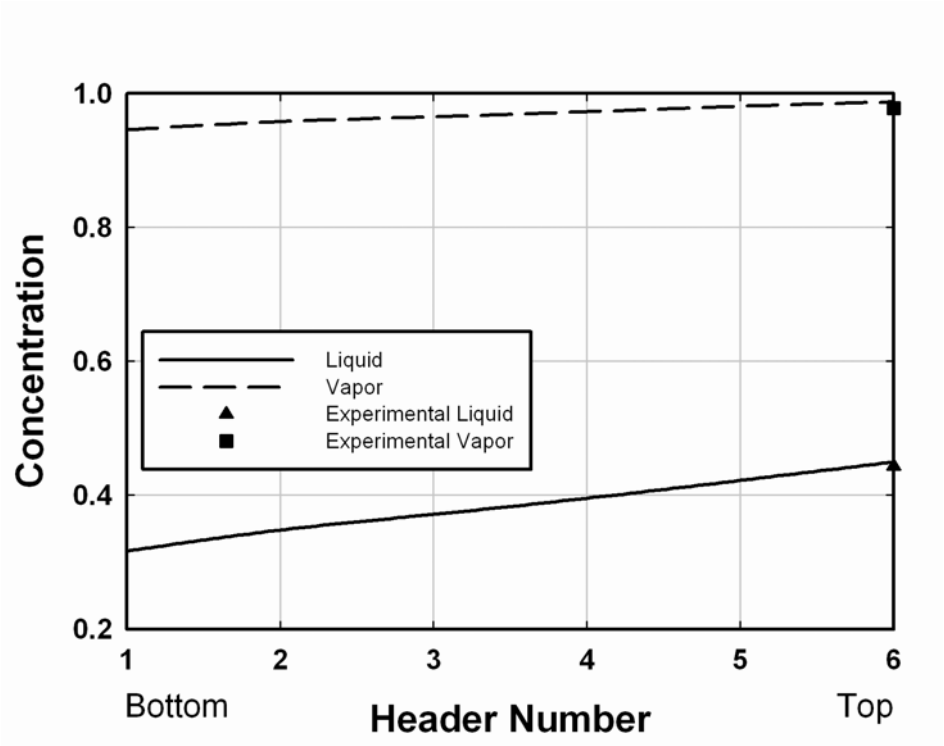

Figure 18 Pass Average Concentration

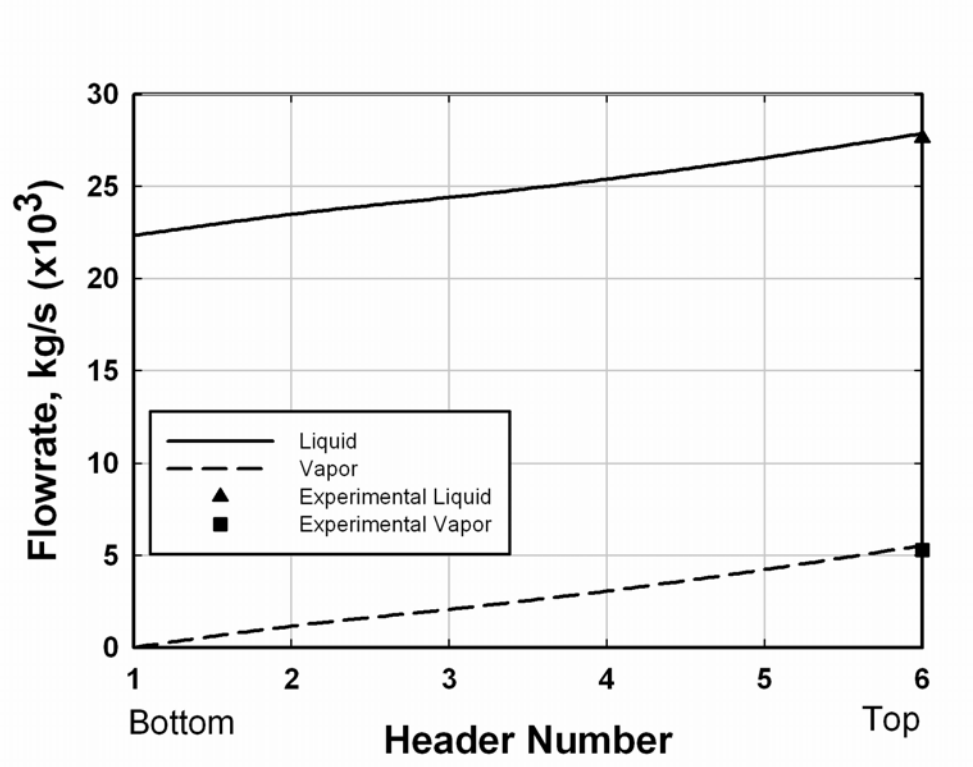

Figure 19 Vapor and Solution Mass Flowrates

The local desorption rates corresponding to the above results are illustrated in Figure 20. The ammonia and total desorption rates follow the trends of the pass heat duty and wetted area fractions shown in Figures 13 and 15. Although the water desorption rates are considerably smaller than those of the ammonia, some insights can be obtained from these trends. The water desorption rate decreases from the bottom of the desorber to the top, and actually becomes negative towards the top. This indicates that water is actually condensing out of the vapor near the top. As can be seen from the corresponding temperature profiles (Figure 12), the vapor is actually being cooled as it progresses up through the segments. This process is known as rectification. In absorption chillers and heat pumps that use volatile absorbents, water in this case, rectification is used to increase the refrigerant concentration in the vapor by cooling the vapor stream, which can be

partly accomplished in this case within the desorber due to the counterflow orientation of the solution and vapor streams.

It can also be seen in Figure 20 that the total and ammonia desorption rates follow the wetted area fraction trends shown in Figure 15. However, the balance between water desorption and reflux condensation (or rectification) rates is a stronger function of local temperature differences (between the vapor and the solution or between the vapor and the tube wall) than on the wetted area fraction. This coupled with the lower water desorption rates that are primarily the consequence of local vapor-liquid equilibrium concentration, results in a fairly monotonous trend in water desorption rates. Figure 21 shows the variation in average liquid and vapor concentration for each pass as well as the vapor interface concentration and the evaporating flux concentration, z. The bulk liquid concentration varies from 0.4358 at the inlet to 0.3321 at the outlet. The vapor is generated at the bottom at a concentration of 0.9515 with the bulk vapor concentration

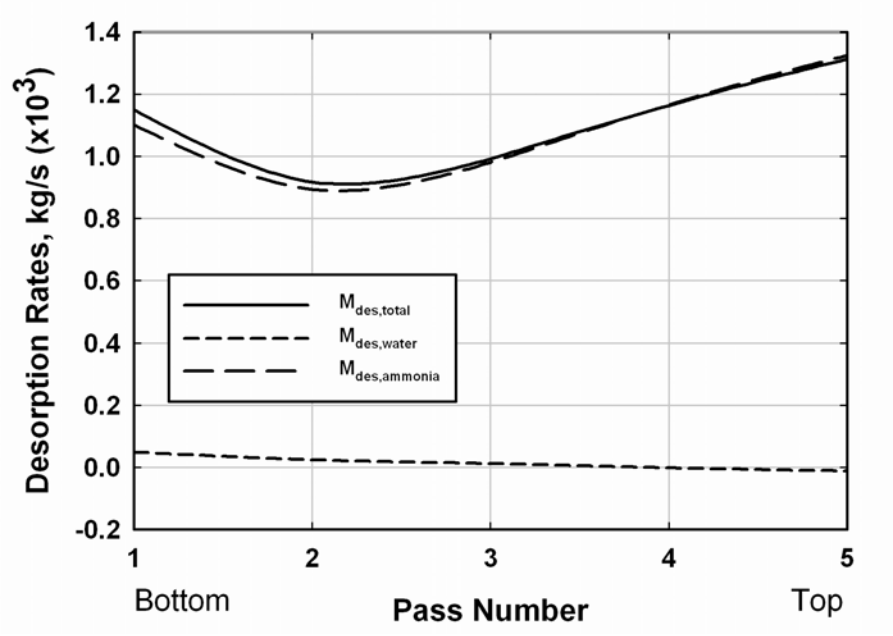

Figure 20 Pass Desorption Rates

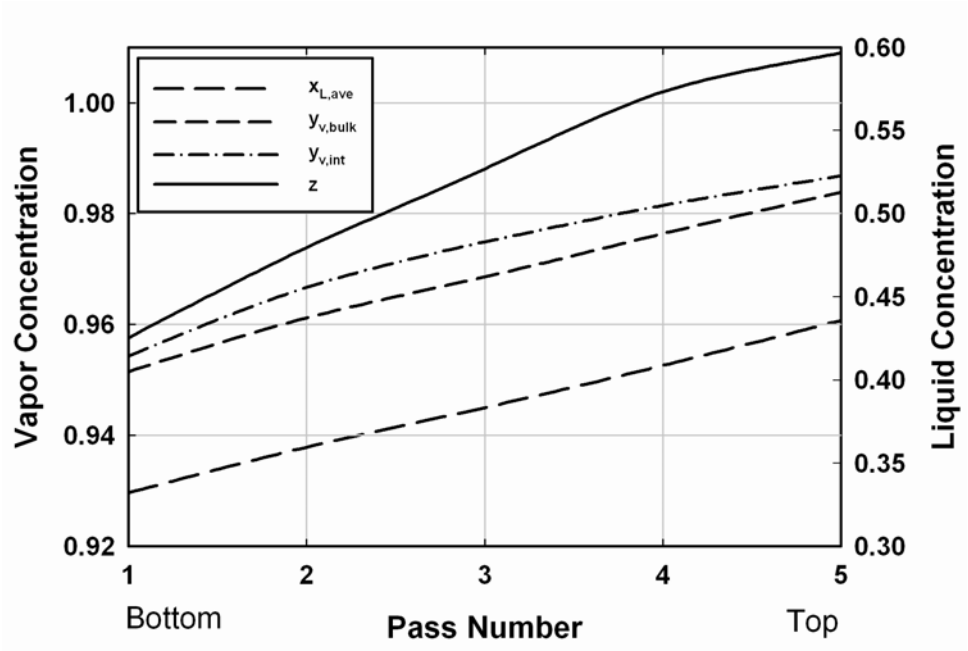

Figure 21 Pass Average Concentrations

rising to 0.9839 at the top due to the decreasing interface temperature and the simultaneous rectification process. The evaporating flux has a concentration of 0.9576 at the bottom and actually becomes greater than one at the top (1.009), indicating that water is undergoing reflux condensation near the top of the desorber.

7 CONCLUSIONS AND RECOMMENDATIONS

A microchannel heat and mass exchanger was tested as a desorber for application in an ammonia water absorption heat pump in this study. The experiments were conducted to investigate the effects of solution flow rate, vapor fraction and glycol/water flowrates on the heat and mass transfer performance. A model was developed to predict the performance of the heat and mass exchanger on a segmental basis through the desorber. This model used heat transfer correlations and the heat and mass transfer analogy to estimate heat and mass fluxes on a segmental basis in the heat and mass exchanger. A parallel resistance network as well as knowledge of the segmental heat duty was used to estimate the fraction of wetted tube area in each segment.

The experiments indicated that the solution flow rate has the largest impact on the overall heat transfer coefficient of the desorber. The overall heat transfer coefficient ranged from 388 to 617 W/m^2-K and the solution side heat transfer coefficient ranged from 659 to 1795 W/m^2-K over the solution flow rates tested.

The segmental analysis of the process revealed that the wetting ratio of the tubes is a major determining factor in the performance of the desorber. Previous work on this geometry had shown that wetting fractions as low as 20-30% were limiting the performance. The model in this study indicates that the average wetting ratios ranged from 25-69%. This increase in wetting ratio is most likely due to the new fluid distribution system used in this study. To further reduce the negative effects of incomplete wetting, it is recommended that the vertical height of the desorber be limited. By limiting the height of the desorber, and increasing the horizontal dimensions of the desorber to maintain adequate heat transfer area, the wetting fractions can be maximized.

While increasing the horizontal dimensions of the heat and mass exchanger will reduce the flow rate per length of tube, the lowered heat transfer coefficient resulting from the lower Reynolds number will be offset by the advantages of maintaining a higher wetting ratio over a larger portion of the heat and mass exchanger.

The model also revealed that rectification of the vapor stream occurs in the upper segments of the desorber. The result of this is a vapor stream with a very high concentration of ammonia, requiring the actual rectifier to be much smaller than would otherwise be necessary with a co-flow desorber design. This geometry is ideally suited for the indirect firing of a desorber, for example, in waste heat recuperation for cooling.

This study has shown that the heat and mass exchanger functions extremely well as a desorber for a residential size heat pump system. This is evidenced by the ability to transfer the required heat loads (6-18 kW) in a small space (178 mm x 178 mm x 0.508 m). This work, coupled with previous work on this heat and mass exchanger geometry by Meacham and Garimella (2003) shows that the same geometry may be used successfully for both the absorber and desorber in an absorption heat pump system. This desorber configuration is well suited for use in waste heat driven absorption systems where the heat source is low temperature cooling fluid, and can be used for GAX absorption system components. It is believed that further improvements and optimization of these designs will facilitate the implementation of compact absorption heat pumps.

Appendix A

Analysis of a Representative Data Point

Table A.1 Representative Test Point Measured Values

Solution Side Measured Values:	***SI***	***EE***
Desorber Vapor Outlet Temperature, $T_{des,v,out}$	68.39°C	155.1°F
Desorber Solution Inlet Temperature, $T_{des,s,in}$	53.94°C	129.1°F
Desorber Solution Outlet Temperature, $T_{des,s,out}$	83.33°C	182.0°F
Desorber Vapor Outlet Pressure, $P_{des,,v,out}$	668.1 kPa	96.9 psia
Desorber Solution Inlet Pressure, $P_{des,s,in}$	667.2 kPa	96.8 psia
Desorber Solution Outlet Pressure, $P_{des,s,out}$	658.7 kPa	95.5 psia
Desorber Solution in Flowrate, $m_{des,s,in}$	0.02762 kg/s	3.65 lb/min
Desorber Solution out Flowrate, $m_{des,s,out}$	0.02233 kg/s	2.95 lb/min
Glycol Side Measured Values:		
Desorber Glycol Inlet Temperature, $T_{des,glyc,in}$	101.10°C	214.0°F
Desorber Glycol Outlet Temperature, $T_{des,glyc,out}$	70.17°C	158.3°F
Desorber Glycol Flowrate, m_{glyc}	0.1152 kg/s	15.23 lb/min
Assumed Values		
Desorber Vapor Outlet Quality, $q_{des,v,out}$	1.0	1.0
Desorber Solution Outlet Quality, $q_{des,s,out}$	0.0	0.0

Table A.2 Overall Desorber Analysis

Eq.#	Equation	Inputs	Outputs
1	**Desorber Vapor Outlet Concentration** $y_{des,out} = f\left(T_{des,v,out}, P_{des,v,out}, q_{des,v,out}\right)$	$T_{des,v,out}$ = 68.39°C $P_{des,,v,out}$ = 668.1 kPa $q_{des,v,out}$ = 1.0	$y_{des,out}$ = 0.9774
2	**Desorber Solution Outlet Concentration** $x_{des,out} = f\left(T_{des,s,out}, P_{des,s,out}, q_{des,s,out}\right)$	$T_{des,s,out}$ = 83.33°C $P_{des,,s,out}$ = 658.7 kPa $q_{des,s,out}$ = 0.0	$x_{des,out}$ = 0.3135
3	**Desorber Mass Balance** $\dot{m}_{des,s,in} = \dot{m}_{des,s,out} + \dot{m}_{des,v,out}$	$m_{des,s,out}$ = 0.02119 kg/s $m_{des,s,in}$ = 0.02644 kg/s	$m_{des,v,out}$ = 0.005247 kg/s
4	**Desorber Species Balance** $x_{des,in} = \frac{\dot{m}_{des,s,out} \cdot x_{des,out} + \dot{m}_{des,v,out} \cdot y_{des,out}}{\dot{m}_{des,s,in}}$	$m_{des,s,in}$ = 0.02644 kg/s $m_{des,s,out}$ = 0.2119 kg/s $m_{des,v,out}$ =0.005247 kg/s $x_{des,out}$ = 0.3135 $y_{des,out}$ = 0.9774	$x_{des,in}$ = 0.445
5	**Solution and Vapor Enthalpies** $h_{des,s,out} = f\left(T_{des,s,out}, P_{des,s,out}, x_{des,out}\right)$ $h_{des,s,in} = f\left(T_{des,s,in}, P_{des,s,in}, x_{des,in}\right)$ $h_{des,v,out} = f\left(T_{des,v,out}, P_{des,v,out}, y_{des,out}\right)$	$T_{des,s,out}$ = 83.33°C $P_{des,,s,out}$ =658.7 kPa $x_{des,out}$ = 0.3135 $T_{des,s,in}$ = 53.94°C $P_{des,,s,in}$ = 667.2 kPa $x_{des,in}$ = 0.445 $T_{des,v,out}$ = 68.39 $P_{des,,v,out}$ = 668.39 kPa $y_{des,out}$ = 0.9774	$h_{des,s,out}$ = 165.2 kJ/kg $h_{des,s,in}$ = 4.477 kJ/kg $h_{des,v,out}$ = 1447 kJ/kg

Table A.2 Overall Desorber Analysis (Continued)

Eq.#	Equation	Inputs	Outputs
6	**Desorber Solution Side Heat Transfer Rate** $\dot{Q}_{des,s} = \dot{m}_{des,s,out} \cdot h_{des,s,out} + \dot{m}_{des,v,out} \cdot h_{des,v,out} - \dot{m}_{des,s,in} \cdot h_{des,s,in}$	$m_{des,s,in}$ = 0.02644 kg/s $m_{des,s,out}$ = 0.2119 kg/s $m_{des,v,out}$ = 0.005247 kg/s $h_{des,s,out}$ = 165.2 kJ/kg $h_{des,s,in}$ = 4.477 kJ/kg $h_{des,v,out}$ = 1447 kJ/kg	$Q_{des,s}$ = 11.22 kW
7	**Desorber Glycol Heat Transfer Rate** $\dot{Q}_{des,glyc} = \dot{m}_{glyc} \cdot c_{p,glyc} \left(T_{des,glyc,in} - T_{des,glyc,out} \right)$	m_{glyc} = 0.1152 kg/s $T_{des,glyc,in}$ = 101.1°C $T_{des,glyc,out}$ = 70.17°C $C_{p,glyc}$ = 3.299 kJ/kg-K	$Q_{des,glyc}$ = 11.76 kW
8	**Average Desorber Heat Transfer Rate** $\dot{Q}_{des,avg} = \left(\dot{Q}_{des,glyc} + \dot{Q}_{des,s} \right) / 2$	$Q_{des,glyc}$ = 11.76 kW $Q_{des,s}$ = 11.22 kW	$Q_{des,avg}$ = 11.49 kW $\Delta\dot{Q} / \dot{Q}_{des,avg}$ = 4.7%
9	**Desorber Log Mean Temperature Difference** $LMTD_{des} = \frac{\left(T_{des.glyc,in} - T_{des,s,out} \right) - \left(T_{des,glyc,out} - T_{des,s,in} \right)}{Ln\left[\frac{\left(T_{des.glyc,in} - T_{des,s,out} \right)}{\left(T_{des,glyc,out} - T_{des,s,in} \right)} \right]}$	$T_{des,glyc,in}$ = 101.1°C $T_{des,glyc,out}$ = 70.17°C $T_{des,s,in}$ = 53.94°C $T_{des,s,out}$ = 83.33°C	$LMTD_{des}$ = 14.27 K
10	**Heat Transfer Cross Sectional Areas, Per Pass and Total** $A_{pp} = N \cdot M \cdot L_{tube} \cdot \pi \cdot D_{OD}$ $A_{des,OD} = N \cdot M \cdot P \cdot L_{tube} \cdot \pi \cdot D_{OD}$ $A_{cs,pp} = N \cdot M \cdot \pi \cdot D_{ID}^2 / 4$	N = 27, Tubes per row M = 16, Rows per Pass P = 5, Number of Passes L_{tube} = 0.140 m D_{OD} = 1.575x10^{-3} m	A_{pp} = 0.2993 m^2 $A_{des,OD}$ = 1.496 m^2 $Area_{CS,pp}$ = 3.863x10^{-4} m^2

Table A.2 Overall Desorber Analysis (Continued)

Eq.#	Equation	Inputs	Outputs
11	**Overall Heat Transfer Coefficient** $\dot{Q}_{des,avg} = U \cdot A_{des,OD} \cdot LMTD_{des}$	$Q_{des,avg}$ = 11.49 kW $LMTD_{des}$ = 14.27 K $A_{des,OD}$ = 1.496 m^2	U = 538 W/m^2-K
12	**Glycol Reynolds Number** $\dot{V}_{glyc} = \frac{\dot{m}_{glyc}}{\rho_{glyc}}$ $V_{glyc} = \frac{\dot{V}_{glyc}}{Area_{cs,pp}}$ $\mathrm{Re}_{glyc} = \frac{\rho_{glyc} \cdot V_{glyc} \cdot D_{ID}}{\mu_{glyc}}$	m_{glyc} = 0.1152 kg/s ρ_{glyc} = 1044 kg/m^3 $Area_{CS,pp}$ = 3.863x10^{-4} m^2 D_{ID} = 1.067x10^{-3} m μ_{glyc} = 1.284x10^{-3} kg/m-s	$\dot{V}_{glyc}$ = 1.104x10^{-4} m^3/s V_{glyc} = 0.2857 m/s Re_{glyc} = 247.8 Flow is laminar: Nu_{glyc} = 4.364
13	**Glycol Heat Transfer Coefficient** $\alpha_{glyc} = \frac{Nu_{glyc} \cdot k_{glyc}}{D_{ID}}$	Nu_{glyc}= 4.364 k_{glyc} = 0.344 W/m-K D_{ID} = 1.067x10^{-3} m	α_{glyc} = 1409 W/m^2-K
14	**Tube Wall Thermal Resistance** $R_w = \frac{D_{OD}}{2 \cdot k_w} \ln\left[\frac{D_{OD}}{D_{ID}}\right]$	D_{OD}= 1.575 x10^{-3} m D_{ID} = 1.067x10^{-3} m k_w= 15.29 W/m-K	R_w = 2.005x10^{-5} m^2-K/W

Table A.2 Overall Desorber Analysis (Continued)

Eq.#	Equation	Inputs	Outputs
15	**Desorber Solution Side Heat Transfer Coefficient** $\alpha_{des,s} = \frac{1}{\left(\frac{1}{U} - \frac{D_{OD}}{D_{ID}\alpha_{glyc}} - R_w\right)}$	$R_w = 2.005 \times 10^{-5}$ m^2-K/W $D_{OD} = 1.575 \times 10^{-3}$ m $D_{ID} = 1.067 \times 10^{-3}$ m U = 538 W/m^2-K α_{glyc} = 1409 W/m^2-K	$\alpha_{des,s}$ = 1265 W/m^2-K

Table A.3 Segmental Heat And Mass Transfer Analysis, Pass 5, (Top)

Eq.#	Equation	Inputs	Outputs
1	**Liquid Surface Tension** $\sigma_{l,dyne/cm} = 1.121\times10^{-6}\cdot T_{l,ave,F}^3 - 1.1955\times10^{-3}\cdot T_{l,ave,F}^2 + 0.2970413\cdot T_{l,ave,F}$ $-6.2041\times10^{1}\cdot x_{l,ave}^3 + 103.3571\cdot x_{l,ave}^2 - 4.8571\times10^{1}\cdot x_{l,ave} + 39.92207$ $+1.9450\times10^{-4}\cdot x_{l,ave}^2\cdot T_{l,ave,F}^2 + 0.1851776\cdot x_{l,ave}^2\cdot T_{l,ave,F}$ $+1.40568\times10^{-3}\cdot x_{l,ave}\cdot T_{l,ave,F}^2 - 7.0072\times10^{-1}\cdot x_{l,ave}\cdot T_{l,ave,F}$ $\sigma_l = \sigma_{l,dyne/cm}\cdot 9.7254\times10^{-4}$ (Herold *et al.* 1996)	$T_{l,ave,F}$ = 140.2°F $x_{l,ave}$ = 0.4358	σ_l = 0.02937 kg/s^2

Table A.3 Segmental Heat And Mass Transfer Analysis, Pass 5 (Continued)

Eq.#	Equation	Inputs	Outputs
2	**Liquid Viscosity** $\mu_{l,cp} = 2.5210 + 1.0675 \cdot x_{l,ave} + 2.2685 \times 10^{-3} \cdot T_{l,ave,F}$ $-0.0322 \cdot (1 - x_{l,ave}) \cdot T_{l,ave,F} - 5.2229 \cdot x_{l,ave}$ $+112.90 \times 10^{-6} (1 - x_{l,ave})^2 \cdot T^2_{l,,ave,F} - 0.8639 \cdot x^3_{l,ave}$ $+2.4387 \cdot x^4_{l,ave}$ $\quad T_{l,ave,F} < 145^\circ\text{F}$ $\mu_{l,cp} = 1.0816 - 0.2202 \cdot x_{l,ave} - 2.17323 \times 10^{-3} \cdot T_{l,ave,F}$ $-1.9322 \times 10^{-3} \cdot (1 - x_{l,ave}) \cdot T_{l,ave,F} - 0.3905 \cdot x_{l,ave}$ $\quad 145^\circ\text{F} \le T_{l,ave,F} \le 195^\circ\text{F}$ $\mu_{l,cp} = 0.5279 + 0.1654 \cdot x_{l,ave} - 1.8905 \times 10^{-3} \cdot T_{l,ave,F}$ $+734.47 \times 10^{-6} \cdot (1 - x_{l,ave}) \cdot T_{l,ave,F}$ $\quad T_{l,ave,F} > 195$ $\mu_l = \mu_{l,cp} \cdot 1 \times 10^{-3}$ (Herold *et al.* 1996)	$T_{l,ave,F}$ = 140.2°F $x_{l,ave}$ = 0.4358	μ_l = 4.883x10^{-4} kg/m-s
3	**Liquid Thermal Conductivity** $k_l = 0.5727 + 1.7021 \times 10^{-3} \cdot T_{l,ave} - 0.0541 \cdot x_{l,ave} - 5.8359 \times 10^{-6} \cdot T^2_{l,ave}$ $+8.4900 \times 10^{-9} \cdot x_{l,ave} - 3.3410 \times 10^{-3} \cdot T_{l,ave} \cdot x_{l,ave}$ (Herold *et al.* 1996)	$T_{l,ave,F}$ = 140.2°F	k_l = 0.5428 W/m-K

Table A.3 Segmental Heat And Mass Transfer Analysis, Pass 5 (Continued)

Eq.#	Equation	Inputs	Outputs
4	**Liquid Specific Heat** $c_{p,l} = h_l(T,P) - h_l(T-1,P)$	T = 60.09 °C P = 664.7 kPa	$c_{p,l}$ = 4.477 kJ/kg-K
5	**Liquid Prandtl Number** $\mathrm{Pr}_l = \frac{\mu_l c_{p,l}}{k_l}$	μ_l = 4.883x10^{-4} kg/m-s $c_{p,l}$=4.477 kJ/kg-K k_l = 0.5428 W/m-K	Pr_l = 4.027
6	**Collision Integrals for Viscosity and Thermal Conductivity** $\Omega_{i,\mu} = 0.7221 - 1.5748\times10^{-3}\cdot\frac{T_{v,bulk}}{(\varepsilon/k)_i} + \frac{5.5435\cdot0.1859}{\left(0.1859+\frac{T_{v,bulk}}{(\varepsilon/k)_i}\right)}$ $\Omega_{i,k} = \Omega_{i,\mu}$ (Mills 1995)	$T_{v,bulk}$ = 65.11°C $(\varepsilon/k)_a$ = 558 K $(\varepsilon/k)_w$ = 809.1 K	$\Omega_{\mu,a}$ = 2.022 $\Omega_{\mu,w}$ = 2.428 $\Omega_{k,a}$ = 2.022 $\Omega_{k,w}$ = 2.428
7	**Component Vapor Viscosity** $\mu_{v,i} = 2.67\times10^{-6}\frac{\sqrt{M_i T}}{\sigma_i^2 \Omega_{\mu,i}}$	M_a = 17.03 kg/kmol M_w = 18.02 kg/kmol T = 65.11°C σ_a = 2.90 Å σ_w = 2.641 Å $\Omega_{\mu,a}$ = 2.022 $\Omega_{\mu,w}$ = 2.428	$\mu_{v,a}$ = 1.192x10^{-5} kg/m-s $\mu_{v,w}$ = 1.231x10^{-5} kg/m-s

Table A.3 Segmental Heat And Mass Transfer Analysis, Pass 5 (Continued)

Eq.#	Equation	Inputs	Outputs
8	**Component Vapor Thermal Conductivity** $k_{translational,i} = 8.32\times10^{-2}\frac{\sqrt{T/M_i}}{\sigma_i^{\,2}\Omega_{k,i}}$ $c_{p,v,i} = \left(5+N_{r,i}\right)\left(\frac{1}{2}\frac{R}{M_i}\right)$ $k_{v,i} = k_{translational,i} + 1.32\left(c_{p,v,i} - \frac{5}{2}\frac{R}{M_i}\right)\mu_{v,i}$	T = 65.11 M_a = 17.03 kg/kmol M_w = 18.02 kg/kmol σ_a = 2.90 Å σ_w = 2.641 Å $\Omega_{k,a}$ = 2.022 $\Omega_{k,w}$ = 1.428 $N_{r,a} = N_{r,w}$ = 3 $\mu_{v,a}$ = 1.192x10^{-5} kg/m-s $\mu_{v,w}$ = 1.231x10^{-5} kg/m-s R = 83414 J/Kmol-K	$k_{v,a}$ = 0.0333 W/m-K $k_{v,w}$ = 0.03254 W/m-K $c_{p,v,a}$ = 1.953 kJ/kg-K $c_{p,v,w}$ = 1.846 kJ/kg-K
9	**Mixture Rules** $\Phi_{ij} = \frac{\left[1+\left(\frac{\mu_{v,i}}{\mu_{v,j}}\right)^{1/2}\left(\frac{M_j}{M_i}\right)^{1/4}\right]^2}{\sqrt{8}\left[1+\left(\frac{M_i}{M_j}\right)\right]^{1/2}}$	M_a = 17.03 kg/kmol M_w = 18.02 kg/kmol $\mu_{v,a}$ = 1.192x10^{-5} kg/m-s $\mu_{v,w}$ = 1.231x10^{-5} kg/m-s	Φ_{aw} = 1.012 Φ_{wa} = 0.988 Φ_{aa} = 1 Φ_{ww} = 1
10	**Mixture Vapor Viscocity and Thermal Conductivity** $\mu_{v,mix} = \sum_{i=1}^{n}\frac{\tilde{y}_i\mu_i}{\sum_{j=1}^{n}\tilde{y}_j\Phi_{ij}}$ $\quad$ $k_{v,mix} = \sum_{i=1}^{n}\frac{\tilde{y}_i k_i}{\sum_{j=1}^{n}\tilde{y}_j\Phi_{ij}}$	$\tilde{y}_a$ = 0.9847 $\tilde{y}_w$ = 0.0153 $\mu_{v,a}$ = 1.192x10^{-5} kg/m-s $\mu_{v,w}$ = 1.231x10^{-5} kg/m-s $k_{v,a}$ = 0.03332 W/m-K $k_{v,w}$ = 0.03254 W/m-K Φ_{aw} = 1.012 Φ_{wa} = 0.988 Φ_{aa} = 1 Φ_{ww} = 1	$\mu_{v,mix}$ = 1.192 x10^{-5} kg/m-s $k_{v,mix}$ = 0.03331 W/m-K

Table A.3 Segmental Heat And Mass Transfer Analysis, Pass 5 (Continued)

Eq.#	Equation	Inputs	Outputs
11	**Vapor Prandtl Number** $\mathrm{Pr}_{v,mix} = \frac{\mu_{v,mix} c_{p,mix}}{k_{v,mix}}$	$\mu_{v,mix}$ = 1.192 x10^{-5} kg/m-s $k_{v,mix}$ = 0.03331 W/m-K $c_{p,v,mix}$ = 2.565 kJ/kg-K	$\mathrm{Pr}_{v,mix}$ = 0.9181
12	**Lennard-Jones Collision Diameter** $\sigma_{aw} = \frac{1}{2}\left(\sigma_a + \sigma_{w,D}\right)$	$\sigma_{w,D}$ = 3.737 Å σ_a = 2.90 Å	σ_{aw} = 3.319 Å
13	**Energy of Attraction Ratio** $\left(\varepsilon_{aw}/k\right)_D = \sqrt{\varepsilon_a/k \cdot \left(\varepsilon_w/k\right)_D}$	ε_a/k = 558 K $(\varepsilon_w/k)_D$ = 32 K	$(\varepsilon_{aw}/k)_D$ = 133.6 K
14	**Collision Integrals for Binary Diffusion Coefficient** $\Omega_D = 0.6716 - 1.8682\times10^{-3}\cdot\frac{T_v}{\left(\varepsilon_{aw}/k\right)_D} + \frac{6.4248\times0.1369}{\left(0.1369 + \frac{T_v}{\left(\varepsilon_{aw}/k\right)_D}\right)}$	$T_{v,bulk}$ = 338.26 K $(\varepsilon_{aw}/k)_D$ = 133.6 K	Ω_D = 0.9967
15	**Binary Diffusion Coefficient** $D_{aw,v} = 1.86\times10^{-7}\frac{\sqrt{T^3\left(\frac{1}{M_a}+\frac{1}{M_w}\right)}}{\sigma_{aw}^2\Omega_D P}$	$T_{v,bulk}$ = 338.26 K M_a = 17.03 kg/kmol M_w =18.02 kg/kmol Ω_D = 0.9967 σ_{aw} = 3.319 Å P = 6.56 atm	$D_{aw,v}$ = 5.432x10^{-6} m^2/s

Table A.3 Segmental Heat And Mass Transfer Analysis, Pass 5 (Continued)

Eq.#	Equation	Inputs	Outputs
16	**Average Vapor Mass Flow Rate** $\dot{m}_{v,ave} = \frac{\dot{m}_{v,in} + \dot{m}_{v,out}}{2}$	$\dot{m}_{v,in} = 0.004223$ kg/s $\dot{m}_{v,out} = 0.005533$ kg/s	$\dot{m}_{v,ave} = 0.004878$ kg/s
17	**Free Area for Vapor Flow** $A_{free} = L_t^2 - L_t \cdot D_{OD} \cdot N$	$L_t = 0.140$ m $D_{OD} = 1.575 \times 10^{-3}$ m N = 27	$A_{free} = 0.01365$ m^2
18	**Maximum Vapor Velocity** $V_{\max,v} = \frac{\dot{m}_{v,ave}}{\rho_v \cdot A_{free}}$	$\dot{m}_{v,ave} = 0.004878$ kg/s $\rho_v = 4.226$ kg/m^3 $A_{free} = 0.01365$ m^2	$V_{max,v} = 0.0846$ m/s
19	**Vapor Reynolds Number** $\mathrm{Re}_{\max,v} = \frac{\rho_v \cdot V_{\max,v} \cdot D_{OD}}{\mu_v}$	$\rho_v = 4.226$ kg/m^3 $V_{max,v} = 0.0846$ m/s $D_{OD} = 1.575 \times 10^{-3}$ m $\mu_v = 1.192 \times 10^{-5}$ kg/m-s	$Re_{max,v} = 47.22$
20	**Vapor Nusselt Number** $Nu_v = 0.3 + \frac{0.62 \cdot \mathrm{Re}_{\max,v}^{1/2} \cdot \mathrm{Pr}_v^{1/3}}{\left[1 + (0.4/\mathrm{Pr}_v)^{2/3}\right]^{1/4}} \left[1 + \left(\frac{\mathrm{Re}_{\max,v}}{282000}\right)^{5/8}\right]^{4/5}$	$Re_{max,v} = 47.22$ $Pr_v = 0.9181$ Churchill and Bernstein (1977) RePr > 0.2	$Nu_v = 3.996$

Table A.3 Segmental Heat And Mass Transfer Analysis, Pass 5 (Continued)

Eq.#	Equation	Inputs	Outputs
21	**Vapor Heat Transfer Coefficient** $\alpha_v = \frac{Nu_v \cdot k_v}{D_{OD}}$	$Nu_v = 3.996$ $D_{OD} = 1.575 \times 10^{-3}$ m $k_v = 0.03331$ W/m-K	$\alpha_v = 84.52$ W/m^2-K
22	**Vapor Schmidt Number** $Sc_v = \frac{\mu_v \cdot v_v}{D_{aw,v}}$	$\mu_v = 1.192 \times 10^{-5}$ kg/m-s $v_v = 0.2366$ m^3 $D_{aw,v} = 5.432 \times 10^{-6}$ m^2/s	$Sc_v = 0.5194$
23	**Vapor Sherwood Number** $Sh_v = Nu_v \left(\frac{Sc_v}{\mathrm{Pr}_v} \right)^{1/3}$	$Nu_v = 3.996$ $Sc_v = 0.5194$ $Pr_v = 0.9181$	$Sh_v = 3.305$
24	**Vapor Mass Transfer Coefficent** $\beta_v = \frac{Sh_v \cdot D_{12,v}}{D_{OD}}$	$Sh_v = 3.305$ $D_{aw,v} = 5.432 \times 10^{-6}$ m^2/s $D_{OD} = 1.575 \times 10^{-3}$ m	$\beta_v = 0.0114$ m/s
25	**Average Liquid Mass Flow Rate** $\dot{m}_l = \frac{\dot{m}_{l,i} + \dot{m}_{l,o}}{2}$	$\dot{m}_{l,i} = 0.02786$ kg/s $\dot{m}_{l,o} = 0.02655$ kg/s	$\dot{m}_l = 0.02721$ kg/s

Table A.3 Segmental Heat And Mass Transfer Analysis, Pass 5 (Continued)

Eq.#	Equation	Inputs	Outputs
26	**Flowrate Per Length of Wetted Tube** $\Gamma_l = \frac{\dot{m}_l}{N\left(a \cdot L_t\right)}$	$\dot{m}_l$ = 0.02721 kg/s N = 27 L_t = 0.140 m a = 0.8234	Γ_l = 8.742x10^{-3} kg/m-s
27	**Liquid Reynolds Number** $\mathrm{Re}_l = \frac{4\Gamma_L}{\mu_l}$	Γ_l = 8.742x10^{-3} kg/m-s μ_l = 4.883x10^{4} kg/m-s	Re_l = 71.61
28	**Liquid Film Thickness** $\delta_f = 0.8434 \cdot \mathrm{Re}^{1/3} \left(\frac{\nu_L^2}{g}\right)^{1/3}$	Γ_l = 8.742x10^{-3} kg/m-s μ_l = 4.883x10^{-4} kg/m-s g = 9.81 m^2/s ρ_l = 820.34 kg/m^3	$\delta_{f,l}$ = 1.158x10^{-4} m
29	**Liquid Nusselt Number** $Nu_l = 0.029 \cdot \mathrm{Re}_l^{0.533} \cdot \mathrm{Pr}_l^{0.344}$	Re_l = 71.61 Pr_l = 4.027	Nu_l = 0.4563
30	**Liquid Film Heat Transfer Coefficient** $\alpha_f = \frac{Nu_l \cdot k_l}{\delta_f}$	Nu_l = 0.4563 k_l = 0.5428 W/m-K $\delta_{f,l}$ = 1.158x10^{-4} m	α_f = 2140 W/m^2-K
31	**Glycol Heat Transfer Coefficient** $\alpha_{glyc} = \frac{Nu_{glyc} \cdot k_{glyc}}{D_{ID}}$	Nu_{glyc} = 4.364 k_{glyc} = 0.3446 W/m-K D_{ID}=1.067x10^{-3} m	α_{glyc} = 1409 W/m^2-K

Table A.3 Segmental Heat And Mass Transfer Analysis, Pass 5 (Continued)

Eq.#	Equation	Inputs	Outputs
32	**Glycol Thermal Resistance** $R_{glyc} = \frac{D_{OD}}{D_{ID} \cdot \alpha_g \cdot A_{pp}}$	$D_{ID} = 1.067 \times 10^{-3}$ m $D_{OD} = 1.575 \times 10^{-3}$ m $\alpha_g = 1409$ W/m^2-K $A_{pp} = 0.2993$ m^2	$R_{glyc} = 0.0035$ K/W
33	**Tube Wall Thermal Resistance** $R_w = \frac{D_{OD}}{2 \cdot k_w \cdot A_{pp}} \ln\left[\frac{D_{OD}}{D_{ID}}\right]$	$D_{ID} = 1.067 \times 10^{-3}$ m $D_{OD} = 1.575 \times 10^{-3}$ m $k_w = 15.54$ W/m-K $A_{pp} = 0.2993$ m^2	$R_w = 6.59 \times 10^{-5}$ K/W
34	**Heat Transfer Rate From Glycol to Tube Wall** $\dot{Q}_{glyc} = \left(\frac{1}{R_{wall} + R_{glyc}}\right) \cdot \left(T_{glyc,ave} - T_{wall}\right)$	$R_{glyc} = 0.0035$ K/W $R_w = 6.59 \times 10^{-5}$ K/W $T_{glyc,ave} = 73.28$°C $T_{wall} = 64.67$°C	$Q_{glyc} = 2.413$ kW
35	**Thermal Resistance of Liquid Film** $R_f = \frac{1}{\alpha_f \cdot a \cdot A_{pp}}$	$\alpha_f = 2140$ W/m^2-K $a = 0.8234$ $A_{pp} = 0.2993$ m^2	$R_f = 1.897 \times 10^{-3}$ K/W
36	**Heat Transfer Rate From Tube Wall to Liquid Film** $\dot{Q}_{wet} = \left(\frac{1}{R_f}\right) \cdot (T_{wall} - T_{l,ave})$	$R_f = 1.897 \times 10^{-3}$ K/W $T_{l,ave} = 60.09$°C $T_{wall} = 64.67$°C	$\dot{Q}_{wet} = 2.415$ kW

Table A.3 Segmental Heat And Mass Transfer Analysis, Pass 5 (Continued)

Eq.#	Equation	Inputs	Outputs
37	**Thermal Resistance of Vapor** $R_{v,dry} = \frac{1}{\alpha_v \cdot (1-a) \cdot A_{pp}}$	α_v = 84.52 W/m^2-K a = 0.8234 A_{pp} = 0.2993 m^2	$R_{v,dry}$ = 0.2238 K/W
38	**Heat Transfer From Tube Wall to Vapor** $\dot{Q}_{dry} = \left(\frac{1}{R_{v,dry}}\right) \cdot \left(T_{wall} - T_{v,bulk}\right)$	$R_{v,dry}$ = 0.2238 K/W $T_{v,bulk}$ = 65.11°C T_{wall} = 64.67°C	$\dot{Q}_{dry}$ = -0.001937 kW
39	**Total Segment Heat Transfer Rate** $\dot{Q}_{seg} = \dot{Q}_{wet} + \dot{Q}_{dry}$	$\dot{Q}_{wet}$ = 2.415 kW $\dot{Q}_{dry}$ = -0.001937 kW	$\dot{Q}_{seg}$ = 2.413 kW
40	**Liquid Film Interface Concentration (Well mixed condition)** $x_{l,\text{int}} = x_{l,ave}$	$x_{l,ave}$ = 0.4358	$x_{l,\text{int}}$ = 0.4358
41	**Interface Temperature** $T_{l,\text{int}} = f\left(P, x_{l,\text{int}}, q=0\right)$	P = 664.7 kPa $x_{l,\text{int}}$ = 0.4358	$T_{l,\text{int}}$ = 60.07°C
42	**Vapor Interface Concentration** $\tilde{y}_{\text{int}} = f\left(T_{l,\text{int}}, P, q=1\right)$	$T_{l,\text{int}}$ = 60.07°C P = 664.7 kPa	$\tilde{y}_{\text{int}}$ = 0.9875

Table A.3 Segmental Heat And Mass Transfer Analysis, Pass 5 (Continued)

Eq.#	Equation	Inputs	Outputs
43	**Vapor Molar Concentration** $C_T = \frac{P}{R \cdot T_{v,bulk}}$	P = 664.7 kPa R = 8314 J/kmol-K $T_{v,bulk}$ = 338.26 K	C_T = 0.2363 kmol/m^3
44	**Total Desorption Flux** $\dot{n}_T = -C_T \beta_v \ln\left[\frac{\tilde{z} - \tilde{y}_{int}}{\tilde{z} - \tilde{y}_{bulk}}\right]$	C_T = 0.2363 kmol/m^3 β_v = 0.0114 m/s $\tilde{z}$ = 1.009 (Obtained iteratively to satisfy mass, species and heat balance) $\tilde{y}_{int}$ = 0.9875 $\tilde{y}_{bulk}$ = 0.9847	$\dot{n}_T$ = 3.124x10^{-4} kmol/m^2-s
45	**Ammonia Desorption Flux** $\dot{n}_a = \tilde{z} \cdot \dot{n}_T$	$\dot{n}_T$ = 3.124x10^{-4} kmol/m^2-s $\tilde{z}$ = 1.009	$\dot{n}_a$ = 3.151 x10^{-4} kmol/m^2-s
46	**Water Desorption Flux** $\dot{n}_w = (1 - \tilde{z}) \cdot \dot{n}_T$	$\dot{n}_T$ = 3.124x10^{-4} kmol/m^2-s $\tilde{z}$ = 1.009	$\dot{n}_w$ = -2.727x10^{-6} kmol/m^2-s negative implies absorption
47	**Component Specific Heats** $\tilde{c}_{p,i} = \frac{R}{2}(5 + N_i)$	N_a = 3 N_w = 3 R = 8314 J/kmol-K	$\tilde{c}_{p,a}$ = 33.26 kJ/kmol-K $\tilde{c}_{p,w}$ = 33.26 kJ/kmol-K

Table A.3 Segmental Heat And Mass Transfer Analysis, Pass 5 (Continued)

Eq.#	Equation	Inputs	Outputs
48	**Parameter for Correction to Heat Transfer due to Mass Transfer** $\phi_T = \frac{\left(\dot{n}_a \cdot \tilde{c}_{p,a} + \dot{n}_w \cdot \tilde{c}_{p,w}\right)}{\alpha_v}$	$\tilde{c}_{p,a} = 33.26$ kJ/kmol-K $\tilde{c}_{p,w} = 33.26$ kJ/kmol-K $\dot{n}_a = 3.151$ x10^{-4} kmol/m^2-s $\dot{n}_w = -2.73$x10^{-6} kmol/m^2-s $\alpha_v = 84.52$ W/m^2-K	$\phi_T = 0.1229$
49	**Vapor-Liquid Log Mean Temperature Difference** $LMTD_{vl} = \frac{\left(T_{v,in} - T_{l,out}\right) - \left(T_{v,out} - T_{l,in}\right)}{Ln\left[\frac{\left(T_{v,in} - T_{l,out}\right)}{\left(T_{v,out} - T_{l,in}\right)}\right]}$	$T_{v,out} = 61.21$°C $T_{v,in} = 69.0$°C $T_{l,in} = 57.6$°C $T_{l,out} = 62.59$°C	$LMTD_{vl} = 4.881$°C
50	**Heat Transfer Rate From Vapor to Liquid** $\dot{Q}_{v\to l} = \alpha_v \left(\frac{\phi_T}{e^{\phi_T} - 1}\right) \cdot a \cdot A_{pp} \cdot LMTD_{vl}$	$\phi_T = 0.1229$ $\alpha_v = 84.52$ W/m^2-K $A_{pp} = 0.2993$ m^2 a = 0.8234 $LMTD_{vl} = 4.881$°C	$\dot{Q}_{v\to l} = 0.9552$ kW $\left(\frac{\phi_T}{e^{\phi_T} - 1}\right) = 0.9398$
51	**Heat Transfer Rate From liquid** $\dot{Q}_v = \dot{Q}_{v\to l} - \dot{Q}_{dry}$	$\dot{Q}_{v\to l} = 0.09552$ kW $\dot{Q}_{dry} = -0.001937$ kW	$\dot{Q}_v = 0.09746$ kW
52	**Segment Vapor Temperature Change** $\dot{Q}_v = \dot{m}_{v,ave} \cdot c_{p,v} \cdot \left(T_{v,in} - T_{v,out}\right)$	$\dot{m}_{v,ave} = 0.004878$ kg/s $c_{p,v} = 2.656$ kJ/kg-K $T_{v,out} = 61.21$°C $T_{v,in} = 69.0$°C	$\dot{Q}_v = 0.09746$ kW

Table A.3 Segmental Heat And Mass Transfer Analysis, Pass 5 (Continued)

Eq.#	Equation	Inputs	Outputs
53	**Vapor Phase Mass Balance** $\dot{m}_{v,out} = \dot{m}_{v,in} + \dot{m}_{des,T}$	$\dot{m}_{v,in} = 0.004223$kg/s $\dot{m}_{des,T} = 0.00131$ kg/s	$\dot{m}_{v,out} = 0.005533$ kg/s
54	**Segment Mass Balance** $\dot{m}_{l,in} + \dot{m}_{v,in} = \dot{m}_{l,out} + \dot{m}_{v,out}$	$\dot{m}_{v,in} = 0.004223$kg/s $\dot{m}_{l,out} = 0.02655$kg/s $\dot{m}_{v,out} = 0.005533$ kg/s	$\dot{m}_{l,in} = 0.02786$ kg/s
55	**Segment Species Balance** $\dot{m}_{l,in} \cdot x_{l,in} + \dot{m}_{v,in} \cdot y_{v,in} = \dot{m}_{l,out} \cdot x_{l,out} + \dot{m}_{v,out} \cdot y_{v,out}$	$\dot{m}_{l,in} = 0.02786$ kg/s $\dot{m}_{v,in} = 0.004223$ kg/s $\dot{m}_{l,out} = 0.02655$ kg/s $\dot{m}_{v,out} = 0.005533$ kg/s $y_{v,in} = 0.9804$ $x_{l,out} = 0.4220$ $y_{v,out} = 0.9873$	$x_{l,in} = 0.4496$
56	**Vapor Phase Species Balance** $\dot{m}_{v,out} \cdot y_{v,out} = \dot{m}_{v,in} \cdot y_{v,in} + \dot{m}_{des,a}$	$\dot{m}_{v,in} = 0.004223$kg/s $\dot{m}_{v,out} = 0.005533$ kg/s $\dot{m}_{des,a} = 0.001322$ kg/s $y_{v,in} = 0.9804$	$y_{v,out} = 0.9873$

Table A.3 Segmental Heat And Mass Transfer Analysis, Pass 5 (Continued)

Eq.#	Equation	Inputs	Outputs
57	**Segment Enthalpy Balance** $\dot{Q}_{seg} = \dot{m}_{l,out} \cdot h_{l,out} + \dot{m}_{v,out} \cdot h_{v,out} - \dot{m}_{l,in} \cdot h_{l,in} - \dot{m}_{v,in} \cdot h_{v,in}$	$\dot{m}_{l,in} = 0.02786$ kg/s $\dot{m}_{v,in} = 0.004223$kg/s $\dot{m}_{l,out} = 0.02655$kg/s $\dot{m}_{v,out} = 0.005533$ kg/s $h_{l,out} = 46.32$ kJ/kg-K $h_{v,out} = 1419$ kJ/kg-K $h_{l,in} = 20.26$ kJ/kg-K $h_{v,in} = 1445$ kJ/kg-K	$\dot{Q}_{seg} = 2.413$ kW
58	**Segment Glycol Heat Transfer Rate** $\dot{Q}_{seg} = \dot{m}_{glyc} \cdot c_{p,glyc} \cdot \left(T_{glyc,in} - T_{glyc,out}\right)$	$\dot{m}_{glyc} = 0.1152$ kg/s $c_{p,glyc} = 3.225$ kJ/kg-K $T_{glyc,in} = 76.53$ $T_{glyc,out} = 70.03$	$\dot{Q}_{seg} = 2.413$ kW

Appendix B

Uncertainty Analysis of a Representative Data Point

Table B.1 Uncertainty Analysis

Eq.#	Equation	Inputs	Outputs
1	**Vapor Mass Flowrate Uncertainty** $\frac{\partial \dot{m}_v}{\partial \dot{m}_{con}} = 1$ $\frac{\partial \dot{m}_v}{\partial \dot{m}_{dil}} = -1$ $u_{\dot{m}_v} = \left[\left(\frac{\partial \dot{m}_v}{\partial \dot{m}_{con}} \cdot u_{\dot{m}_{con}} \right)^2 + \left(\frac{\partial \dot{m}_v}{\partial \dot{m}_{dil}} \cdot u_{\dot{m}_{dil}} \right)^2 \right]^{1/2}$	$\dot{m}_{con} = 0.02644 \pm 3.96 \times 10^{-5}$ kg/s $\dot{m}_{dil} = 0.01964 \pm 2.95 \times 10^{-5}$ kg/s	$\dot{m}_v = 0.0068 \pm 4.94 \times 10^{-5}$ kg/s 0.7% Uncertainty
2	**Dilute Solution Concentration Uncertainty** $\frac{\partial x_{dil}}{\partial P_{dil}} = \left(\frac{x_{dil}\left(P_{dil} + u_{P_{dil}}\right) - x_{dil}\left(P_{dil} - u_{P_{dil}}\right)}{2 \cdot u_{P_{dil}}} \right)$ $\frac{\partial x_{dil}}{\partial T_{dil}} = \left(\frac{x_{dil}\left(T_{dil} + u_{T_{dil}}\right) - x_{dil}\left(T_{dil} - u_{T_{dil}}\right)}{2 \cdot u_{T_{dil}}} \right)$ $u_{x_{dil}} = \left[\left(\frac{\partial x_{dil}}{\partial T_{dil}} \cdot u_{T_{dil}} \right)^2 + \left(\frac{\partial x_{dil}}{\partial P_{dil}} \cdot u_{P_{dil}} \right)^2 \right]^{1/2}$	$T_{dil} = 79.39 \pm 0.5$°C $P_{dil} = 553.3 \pm 2.586$ kPa	$x_{dil} = 0.3049 \pm 0.002475$

Table B.1 Uncertainty Analysis (Continued)

Eq.#	Equation	Inputs	Outputs
3	**Concentrated Solution Concentration Uncertainty** $\frac{\partial x_{con}}{\partial \dot{m}_{con}} = \left(\frac{x_{con}\left(\dot{m}_{con} + u_{\dot{m}_{con}}\right) - x_{con}\left(\dot{m}_{con} - u_{\dot{m}_{con}}\right)}{2 \cdot u_{\dot{m}_{con}}} \right)$ $\frac{\partial x_{con}}{\partial \dot{m}_{dil}} = \left(\frac{x_{con}\left(\dot{m}_{dil} + u_{\dot{m}_{dil}}\right) - x_{con}\left(\dot{m}_{dil} - u_{\dot{m}_{dil}}\right)}{2 \cdot u_{\dot{m}_{dil}}} \right)$ $\frac{\partial x_{con}}{\partial P_{dil}} = \left(\frac{x_{con}\left(P_{dil} + u_{P_{dil}}\right) - x_{con}\left(P_{dil} - u_{P_{dil}}\right)}{2 \cdot u_{P_{dil}}} \right)$ $\frac{\partial x_{con}}{\partial P_{vap}} = \left(\frac{x_{con}\left(P_{vap} + u_{P_{vap}}\right) - x_{con}\left(P_{vap} - u_{P_{vap}}\right)}{2 \cdot u_{P_{vap}}} \right)$ $\frac{\partial x_{con}}{\partial T_{dil}} = \left(\frac{x_{con}\left(T_{dil} + u_{T_{dil}}\right) - x_{con}\left(T_{dil} - u_{T_{dil}}\right)}{2 \cdot u_{T_{dil}}} \right)$ $\frac{\partial x_{con}}{\partial T_{vap}} = \left(\frac{x_{con}\left(T_{vap} + u_{T_{vap}}\right) - x_{con}\left(T_{vap} - u_{T_{vap}}\right)}{2 \cdot u_{T_{vap}}} \right)$	$\dot{m}_{con} = 0.02644 \pm 3.96 \times 10^{-5}$ kg/s $\dot{m}_{dil} = 0.01964 \pm 2.95 \times 10^{-5}$ kg/s $P_{dil} = 553.3 \pm 2.586$ kPa $P_{vap} = 557.2 \pm 2.586$ kPa $T_{dil} = 79.39 \pm 0.5$°C $T_{vap} = 59.5 \pm 0.5$°C	$x_{con} = 0.4793 \pm 0.00213$

Table B.1 Uncertainty Analysis (Continued)

Eq.#	Equation	Inputs	Outputs
3 Cont.	**Concentrated Solution Concentration Uncertainty (Continued)** $u_{x_{con}} = \left[\left(\frac{\partial x_{con}}{\partial \dot{m}_{con}} \cdot u_{\dot{m}_{con}} \right)^2 + \left(\frac{\partial x_{con}}{\partial \dot{m}_{dil}} \cdot u_{\dot{m}_{dil}} \right)^2 + \left(\frac{\partial x_{con}}{\partial P_{dil}} \cdot u_{P_{dil}} \right)^2 + \left(\frac{\partial x_{con}}{\partial P_{vap}} \cdot u_{P_{vap}} \right)^2 + \left(\frac{\partial x_{con}}{\partial T_{dil}} \cdot u_{T_{dil}} \right) + \left(\frac{\partial x_{con}}{\partial T_{vap}} \cdot u_{T_{vap}} \right)^2 \right]^{1/2}$	$\dot{m}_{con} = 0.02644 \pm 3.96 \times 10^{-5}$ kg/s $\dot{m}_{dil} = 0.01964 \pm 2.95 \times 10^{-5}$ kg/s P_{dil}= 553.3±2.586 kPa P_{vap}= 557.2±2.586 kPa T_{dil}= 79.39±0.5°C T_{vap}= 59.5±0.5°C	x_{con} =0.4793±0.00213
4	**Vapor Concentration Uncertainty** $\frac{\partial y_{vap}}{\partial P_{vap}} = \left(\frac{y_{vap}\left(P_{vap} + u_{P_{vap}}\right) - y_{vap}\left(P_{vap} - u_{P_{vap}}\right)}{2 \cdot u_{P_{vap}}} \right)$ $\frac{\partial y_{vap}}{\partial T_{vap}} = \left(\frac{y_{vap}\left(T_{vap} + u_{T_{vap}}\right) - y_{vap}\left(T_{vap} - u_{T_{vap}}\right)}{2 \cdot u_{T_{vap}}} \right)$ $u_{y_{vap}} = \left[\left(\frac{\partial y_{vap}}{\partial T_{vap}} \cdot u_{T_{vap}} \right)^2 + \left(\frac{\partial y_{vap}}{\partial P_{vap}} \cdot u_{P_{vap}} \right)^2 \right]^{1/2}$	T_{vap}= 59.5±0.5°C P_{vap}= 557.2±2.586 kPa	y_{vap} =0.9832±0.0005794

Table B.1 Uncertainty Analysis (Continued)

Eq.#	Equation	Inputs	Outputs
5	**Dilute Solution Enthalpy Uncertainty** $\frac{\partial h_{dil}}{\partial P_{dil}} = \left(\frac{h_{dil}\left(P_{dil} + u_{P_{dil}}\right) - h_{dil}\left(P_{dil} - u_{P_{dil}}\right)}{2 \cdot u_{P_{dil}}} \right)$ $\frac{\partial h_{dil}}{\partial T_{dil}} = \left(\frac{h_{dil}\left(T_{dil} + u_{T_{dil}}\right) - h_{dil}\left(T_{dil} - u_{T_{dil}}\right)}{2 \cdot u_{T_{dil}}} \right)$ $u_{h_{dil}} = \left[\left(\frac{\partial h_{dil}}{\partial T_{dil}} \cdot u_{T_{dil}} \right)^2 + \left(\frac{\partial h_{dil}}{\partial P_{dil}} \cdot u_{P_{dil}} \right)^2 \right]^{1/2}$	T_{dil}= 79.39±0.5°C P_{dil}= 553.3±2.586 kPa	h_{dil}=151.9±3.128 kJ/kg
6	**Vapor Enthalpy Uncertainty** $\frac{\partial h_{vap}}{\partial P_{vap}} = \left(\frac{h_{vap}\left(P_{vap} + u_{P_{vap}}\right) - h_{vap}\left(P_{vap} - u_{P_{vap}}\right)}{2 \cdot u_{P_{vap}}} \right)$ $\frac{\partial h_{vap}}{\partial T_{vap}} = \left(\frac{h_{vap}\left(T_{vap} + u_{T_{vap}}\right) - h_{vap}\left(T_{vap} - u_{T_{vap}}\right)}{2 \cdot u_{T_{vap}}} \right)$ $u_{h_{vap}} = \left[\left(\frac{\partial h_{vap}}{\partial T_{vap}} \cdot u_{T_{vap}} \right)^2 + \left(\frac{\partial h_{vap}}{\partial P_{vap}} \cdot u_{P_{vap}} \right)^2 \right]^{1/2}$	T_{vap}= 59.5±0.5°C P_{vap}= 557.2±2.586 kPa	h_{vap} =1424±1.844 kJ/kg

Table B.1 Uncertainty Analysis (Continued)

Eq.#	Equation	Inputs	Outputs
7	**Concentrated Solution Enthalpy Uncertainty** $\frac{\partial h_{con}}{\partial \dot{m}_{con}} = \left(\frac{h_{con}\left(\dot{m}_{con} + u_{\dot{m}_{con}}\right) - h_{con}\left(\dot{m}_{con} - u_{\dot{m}_{con}}\right)}{2 \cdot u_{\dot{m}_{con}} \right)$ $\frac{\partial h_{con}}{\partial \dot{m}_{dil}} = \left(\frac{h_{con}\left(\dot{m}_{dil} + u_{\dot{m}_{dil}}\right) - h_{con}\left(\dot{m}_{dil} - u_{\dot{m}_{dil}}\right)}{2 \cdot u_{\dot{m}_{dil}} \right)$ $\frac{\partial h_{con}}{\partial P_{con}} = \left(\frac{h_{con}\left(P_{con} + u_{P_{con}}\right) - h_{con}\left(P_{con} - u_{P_{con}}\right)}{2 \cdot u_{P_{con}} \right)$ $\frac{\partial h_{con}}{\partial P_{dil}} = \left(\frac{h_{con}\left(P_{dil} + u_{P_{dil}}\right) - h_{con}\left(P_{dil} - u_{P_{dil}}\right)}{2 \cdot u_{P_{dil}} \right)$ $\frac{\partial h_{con}}{\partial P_{vap}} = \left(\frac{h_{con}\left(P_{vap} + u_{P_{vap}}\right) - h_{con}\left(P_{vap} - u_{P_{vap}}\right)}{2 \cdot u_{P_{vap}} \right)$ $\frac{\partial h_{con}}{\partial T_{con}} = \left(\frac{h_{con}\left(T_{con} + u_{T_{con}}\right) - h_{con}\left(T_{con} - u_{T_{con}}\right)}{2 \cdot u_{T_{con}} \right)$ $\frac{\partial h_{con}}{\partial T_{dil}} = \left(\frac{h_{con}\left(T_{dil} + u_{T_{dil}}\right) - h_{con}\left(T_{dil} - u_{T_{dil}}\right)}{2 \cdot u_{T_{dil}} \right)$	$\dot{m}_{con} = 0.02644 \pm 3.96 \times 10^{-5}$ kg/s $\dot{m}_{dil} = 0.01964 \pm 2.95 \times 10^{-5}$ kg/s $P_{con} = 559.9 \pm 2.586$ kPa $P_{dil} = 553.3 \pm 2.586$ kPa $P_{vap} = 557.2 \pm 2.586$ kPa $T_{con} = 47.39 \pm 0.5$°C $T_{dil} = 79.39 \pm 0.5$°C $T_{vap} = 59.5 \pm 0.5$°C	$h_{con} = -15.75 \pm 12.31$ kJ/kg

Table B.1 Uncertainty Analysis (Continued)

Eq.#	Equation	Inputs	Outputs
7 Cont.	**Concentrated Solution Enthalpy Uncertainty (Continued)** $\frac{\partial h_{con}}{\partial T_{vap}} = \left(\frac{h_{con}\left(T_{vap}+u_{T_{vap}}\right) - h_{con}\left(T_{vap}-u_{T_{vap}}\right)}{2 \cdot u_{T_{vap}}} \right)$ $u_{h_{con}} = \left[\begin{array}{l} \left(\frac{\partial h_{con}}{\partial \dot{m}_{con}} \cdot u_{\dot{m}_{con}} \right)^2 + \left(\frac{\partial h_{con}}{\partial \dot{m}_{dil}} \cdot u_{\dot{m}_{dil}} \right)^2 + \left(\frac{\partial h_{con}}{\partial P_{con}} \cdot u_{P_{con}} \right)^2 \\ + \left(\frac{\partial h_{con}}{\partial P_{dil}} \cdot u_{P_{dil}} \right)^2 + \left(\frac{\partial h_{con}}{\partial P_{vap}} \cdot u_{P_{vap}} \right)^2 + \left(\frac{\partial h_{con}}{\partial T_{con}} \cdot u_{T_{vap}} \right)^2 \\ + \left(\frac{\partial h_{con}}{\partial T_{dil}} \cdot u_{T_{dil}} \right)^2 + \left(\frac{\partial h_{con}}{\partial T_{vap}} \cdot u_{T_{vap}} \right)^2 \end{array} \right]^{1/2}$	$\dot{m}_{con} = 0.02644 \pm 3.96 \times 10^{-5}$ kg/s $\dot{m}_{dil} = 0.01964 \pm 2.95 \times 10^{-5}$ kg/s P_{con}= 559.9±2.586 kPa P_{dil}= 553.3±2.586 kPa P_{vap}= 557.2±2.586 kPa T_{con}= 47.39±0.5°C T_{dil}= 79.39±0.5°C T_{vap}= 59.5±0.5°C	h_{con} =-15.75±12.31 kJ/kg
8	**Solution-Side Heat Duty Uncertainty** $\frac{\partial \dot{Q}_{sol}}{\partial \dot{m}_{con}} = \left(\frac{\dot{Q}_{sol}\left(\dot{m}_{con}+u_{\dot{m}_{con}}\right) - \dot{Q}_{sol}\left(\dot{m}_{con}-u_{\dot{m}_{con}}\right)}{2 \cdot u_{\dot{m}_{con}}} \right)$ $\frac{\partial \dot{Q}_{sol}}{\partial \dot{m}_{dil}} = \left(\frac{\dot{Q}_{sol}\left(\dot{m}_{dil}+u_{\dot{m}_{dil}}\right) - \dot{Q}_{sol}\left(\dot{m}_{dil}-u_{\dot{m}_{dil}}\right)}{2 \cdot u_{\dot{m}_{dil}}} \right)$	$\dot{m}_{con} = 0.02644 \pm 3.96 \times 10^{-5}$ kg/s $\dot{m}_{dil} = 0.01964 \pm 2.95 \times 10^{-5}$ kg/s P_{con}= 559.9±2.586 kPa P_{dil}= 553.3±2.586 kPa P_{vap}= 557.2±2.586 kPa T_{con}= 47.39±0.5°C T_{dil}= 79.39±0.5°C T_{vap}= 59.5±0.5°C	$\dot{Q}_{sol} = 13.09 \pm 0.347$ kW 2.6% Uncertainty

Table B.1 Uncertainty Analysis (Continued)

Eq.#	Equation	Inputs	Outputs
8 Cont.	**Solution-Side Heat Duty Uncertainty (Continued)** $\frac{\partial \dot{Q}_{sol}}{\partial P_{con}} = \left(\frac{\dot{Q}_{sol}\left(P_{con}+u_{P_{con}}\right) - \dot{Q}_{sol}\left(P_{con}-u_{P_{con}}\right)}{2 \cdot u_{P_{con}}} \right)$ $\frac{\partial \dot{Q}_{sol}}{\partial P_{dil}} = \left(\frac{\dot{Q}_{sol}\left(P_{dil}+u_{P_{dil}}\right) - \dot{Q}_{sol}\left(P_{dil}-u_{P_{dil}}\right)}{2 \cdot u_{P_{dil}}} \right)$ $\frac{\partial \dot{Q}_{sol}}{\partial P_{vap}} = \left(\frac{\dot{Q}_{sol}\left(P_{vap}+u_{P_{vap}}\right) - \dot{Q}_{sol}\left(P_{vap}-u_{P_{vap}}\right)}{2 \cdot u_{P_{vap}}} \right)$ $\frac{\partial \dot{Q}_{sol}}{\partial T_{con}} = \left(\frac{\dot{Q}_{sol}\left(T_{con}+u_{T_{con}}\right) - \dot{Q}_{sol}\left(T_{con}-u_{T_{con}}\right)}{2 \cdot u_{T_{con}}} \right)$ $\frac{\partial \dot{Q}_{sol}}{\partial T_{dil}} = \left(\frac{\dot{Q}_{sol}\left(T_{dil}+u_{T_{dil}}\right) - \dot{Q}_{sol}\left(T_{dil}-u_{T_{dil}}\right)}{2 \cdot u_{T_{dil}}} \right)$ $\frac{\partial \dot{Q}_{sol}}{\partial T_{vap}} = \left(\frac{\dot{Q}_{sol}\left(T_{vap}+u_{T_{vap}}\right) - \dot{Q}_{sol}\left(T_{vap}-u_{T_{vap}}\right)}{2 \cdot u_{T_{vap}}} \right)$	$\dot{m}_{con} = 0.02644 \pm 3.96 \times 10^{-5}$ kg/s $\dot{m}_{dil} = 0.01964 \pm 2.95 \times 10^{-5}$ kg/s P_{con}= 559.9±2.586 kPa P_{dil}= 553.3±2.586 kPa P_{vap}= 557.2±2.586 kPa T_{con}= 47.39±0.5°C T_{dil}= 79.39±0.5°C T_{vap}= 59.5±0.5°C	$\dot{Q}_{sol} = 13.09 \pm 0.347$ kW 2.6% Uncertainty

Table B.1 Uncertainty Analysis (Continued)

Eq.#	Equation	Inputs	Outputs
8 Cont.	**Solution-Side Heat Duty Uncertainty (Continued)** $u_{\dot{Q}_{sol}} = \left[\begin{array}{l} \left(\frac{\partial \dot{Q}_{sol}}{\partial \dot{m}_{con}} \cdot u_{\dot{m}_{con}} \right)^2 + \left(\frac{\partial \dot{Q}_{sol}}{\partial \dot{m}_{dil}} \cdot u_{\dot{m}_{dil}} \right)^2 + \left(\frac{\partial \dot{Q}_{sol}}{\partial P_{con}} \cdot u_{P_{con}} \right)^2 \\ + \left(\frac{\partial \dot{Q}_{sol}}{\partial P_{dil}} \cdot u_{P_{dil}} \right)^2 + \left(\frac{\partial \dot{Q}_{sol}}{\partial P_{vap}} \cdot u_{P_{vap}} \right)^2 + \left(\frac{\partial \dot{Q}_{sol}}{\partial T_{con}} \cdot u_{T_{vap}} \right)^2 \\ + \left(\frac{\partial \dot{Q}_{sol}}{\partial T_{dil}} \cdot u_{T_{dil}} \right)^2 + \left(\frac{\partial \dot{Q}_{sol}}{\partial T_{vap}} \cdot u_{T_{vap}} \right)^2 \end{array} \right]^{1/2}$	$\dot{m}_{con} = 0.02644 \pm 3.96 \text{x} 10^{-5}$ kg/s $\dot{m}_{dil} = 0.01964 \pm 2.95 \text{x} 10^{-5}$ kg/s P_{con}= 559.9±2.586 kPa P_{dil}= 553.3±2.586 kPa P_{vap}= 557.2±2.586 kPa T_{con}= 47.39±0.5°C T_{dil}= 79.39±0.5°C T_{vap}= 59.5±0.5°C	$\dot{Q}_{sol} = 13.09 \pm 0.347$ kW 2.6% Uncertainty
9	**Glycol-Side Heat Duty Uncertainty** $\frac{\partial \dot{Q}_{glyc}}{\partial \dot{m}_{glyc}} = \left(\frac{\dot{Q}_{glyc}\left(\dot{m}_{glyc} + u_{\dot{m}_{glyc}}\right) - \dot{Q}_{glyc}\left(\dot{m}_{glyc} - u_{\dot{m}_{glyc}}\right)}{2 \cdot u_{\dot{m}_{glyc}}} \right)$ $\frac{\partial \dot{Q}_{glyc}}{\partial T_{glyc,in}} = \left(\frac{\dot{Q}_{glyc}\left(T_{glyc,in} + u_{T_{glyc,in}}\right) - \dot{Q}_{glyc}\left(T_{glyc,in} - u_{T_{glyc,in}}\right)}{2 \cdot u_{T_{glyc,in}}} \right)$ $\frac{\partial \dot{Q}_{glyc}}{\partial T_{glyc,out}} = \left(\frac{\dot{Q}_{glyc}\left(T_{glyc,out} + u_{T_{glyc,out}}\right) - \dot{Q}_{glyc}\left(T_{glyc,out} - u_{T_{glyc,out}}\right)}{2 \cdot u_{T_{glyc,out}}} \right)$	$\dot{m}_{glyc} = 0.1531 \pm 2.297 \text{x} 10^{-4}$ kg/s $T_{glyc,in}$=93.78±0.5°C $T_{glyc,out}$=68.0±0.5°C	$\dot{Q}_{glyc} = 12.93 \pm 0.3553$ kW 2.7% Uncertainty

Table B.1 Uncertainty Analysis (Continued)

Eq.#	Equation	Inputs	Outputs
9 Cont.	**Glycol-Side Heat Duty Uncertainty (Continued)** $u_{\dot{Q}_{glyc}} = \left[\left(\frac{\partial \dot{Q}_{glyc}}{\partial \dot{m}_{glyc}} \cdot u_{\dot{m}_{glyc}} \right)^2 + \left(\frac{\partial \dot{Q}_{glyc}}{\partial T_{glyc,in}} \cdot u_{T_{glyc,in}} \right)^2 + \left(\frac{\partial \dot{Q}_{glyc}}{\partial T_{glyc,out}} \cdot u_{T_{glyc,out}} \right)^2 \right]^{1/2}$	$\dot{m}_{glyc} = 0.1531 \pm 2.297 \text{x} 10^{-4}$ kg/s $T_{glyc,in}$=93.78±0.5°C $T_{glyc,out}$=68.0±0.5°C	$\dot{Q}_{glyc} = 12.93 \pm 0.3553$ kW 2.7% Uncertainty
10	**Average Desorber Heat Duty Uncertainty** $\frac{\partial \dot{Q}_{ave}}{\partial \dot{m}_{con}} = \left(\frac{\dot{Q}_{ave}\left(\dot{m}_{con} + u_{\dot{m}_{con}}\right) - \dot{Q}_{ave}\left(\dot{m}_{con} - u_{\dot{m}_{con}}\right)}{2 \cdot u_{\dot{m}_{con}}} \right)$ $\frac{\partial \dot{Q}_{ave}}{\partial \dot{m}_{dil}} = \left(\frac{\dot{Q}_{ave}\left(\dot{m}_{dil} + u_{\dot{m}_{dil}}\right) - \dot{Q}_{ave}\left(\dot{m}_{dil} - u_{\dot{m}_{dil}}\right)}{2 \cdot u_{\dot{m}_{dil}}} \right)$ $\frac{\partial \dot{Q}_{ave}}{\partial \dot{m}_{glyc}} = \left(\frac{\dot{Q}_{ave}\left(\dot{m}_{glyc} + u_{\dot{m}_{glyc}}\right) - \dot{Q}_{ave}\left(\dot{m}_{glyc} - u_{\dot{m}_{glyc}}\right)}{2 \cdot u_{\dot{m}_{glyc}}} \right)$ $\frac{\partial \dot{Q}_{ave}}{\partial P_{con}} = \left(\frac{\dot{Q}_{ave}\left(P_{con} + u_{P_{con}}\right) - \dot{Q}_{ave}\left(P_{con} - u_{P_{con}}\right)}{2 \cdot u_{P_{con}}} \right)$ $\frac{\partial \dot{Q}_{ave}}{\partial P_{dil}} = \left(\frac{\dot{Q}_{ave}\left(P_{dil} + u_{P_{dil}}\right) - \dot{Q}_{ave}\left(P_{dil} - u_{P_{dil}}\right)}{2 \cdot u_{P_{dil}}} \right)$	$\dot{m}_{con} = 0.02644 \pm 3.96 \text{x} 10^{-5}$ kg/s $\dot{m}_{dil} = 0.01964 \pm 2.95 \text{x} 10^{-5}$ kg/s $\dot{m}_{glyc} = 0.1531 \pm 2.297 \text{x} 10^{-4}$ kg/s P_{con}= 559.9±2.586 kPa P_{dil}= 553.3±2.586 kPa P_{vap}= 557.2±2.586 kPa T_{con}= 47.39±0.5°C T_{dil}= 79.39±0.5°C T_{vap}= 59.5±0.5°C $T_{glyc,in}$=93.78±0.5°C $T_{glyc,out}$=68.0±0.5°C	$\dot{Q}_{ave} = 13.01 \pm 0.2483$ kW 1.9% Uncertainty

Table B.1 Uncertainty Analysis (Continued)

Eq.#	Equation	Inputs	Outputs
10 Cont.	**Average Desorber Heat Duty Uncertainty (Continued)** $\frac{\partial \dot{Q}_{ave}}{\partial P_{vap}} = \left(\frac{\dot{Q}_{ave}\left(P_{vap} + u_{P_{vap}}\right) - \dot{Q}_{ave}\left(P_{vap} - u_{P_{vap}}\right)}{2 \cdot u_{P_{vap}}} \right)$ $\frac{\partial \dot{Q}_{ave}}{\partial T_{con}} = \left(\frac{\dot{Q}_{ave}\left(T_{con} + u_{T_{con}}\right) - \dot{Q}_{ave}\left(T_{con} - u_{T_{con}}\right)}{2 \cdot u_{T_{con}}} \right)$ $\frac{\partial \dot{Q}_{ave}}{\partial T_{dil}} = \left(\frac{\dot{Q}_{ave}\left(T_{dil} + u_{T_{dil}}\right) - \dot{Q}_{ave}\left(T_{dil} - u_{T_{dil}}\right)}{2 \cdot u_{T_{dil}}} \right)$ $\frac{\partial \dot{Q}_{ave}}{\partial T_{vap}} = \left(\frac{\dot{Q}_{ave}\left(T_{vap} + u_{T_{vap}}\right) - \dot{Q}_{ave}\left(T_{vap} - u_{T_{vap}}\right)}{2 \cdot u_{T_{vap}}} \right)$ $\frac{\partial \dot{Q}_{ave}}{\partial T_{glyc,in}} = \left(\frac{\dot{Q}_{ave}\left(T_{glyc,in} + u_{T_{glyc,in}}\right) - \dot{Q}_{ave}\left(T_{glyc,in} - u_{T_{glyc,in}}\right)}{2 \cdot u_{T_{glyc,in}}} \right)$ $\frac{\partial \dot{Q}_{ave}}{\partial T_{glyc,out}} = \left(\frac{\dot{Q}_{ave}\left(T_{glyc,out} + u_{T_{glyc,out}}\right) - \dot{Q}_{ave}\left(T_{glyc,out} - u_{T_{glyc,out}}\right)}{2 \cdot u_{T_{glyc,out}}} \right)$	$\dot{m}_{con} = 0.02644 \pm 3.96 \times 10^{-5}$ kg/s $\dot{m}_{dil} = 0.01964 \pm 2.95 \times 10^{-5}$ kg/s $\dot{m}_{glyc} = 0.1531 \pm 2.297 \times 10^{-4}$ kg/s P_{con}= 559.9±2.586 kPa P_{dil}= 553.3±2.586 kPa P_{vap}= 557.2±2.586 kPa T_{con}= 47.39±0.5°C T_{dil}= 79.39±0.5°C T_{vap}= 59.5±0.5°C $T_{glyc,in}$=93.78±0.5°C $T_{glyc,out}$=68.0±0.5°C	$\dot{Q}_{ave} = 13.01 \pm 0.2483$ kW 1.9% Uncertainty

Table B.1 Uncertainty Analysis (Continued)

Eq.#	Equation	Inputs	Outputs
10 Cont.	**Average Desorber Heat Duty Uncertainty (Continued)** $u_{\dot{Q}_{ave}} = \left[\begin{array}{l} \left(\frac{\partial \dot{Q}_{ave}}{\partial \dot{m}_{con}} \cdot u_{\dot{m}_{con}} \right)^2 + \left(\frac{\partial \dot{Q}_{ave}}{\partial \dot{m}_{dil}} \cdot u_{\dot{m}_{dil}} \right)^2 + \left(\frac{\partial \dot{Q}_{ave}}{\partial \dot{m}_{glyc}} \cdot u_{\dot{m}_{glyc}} \right)^2 \\ + \left(\frac{\partial \dot{Q}_{ave}}{\partial P_{con}} \cdot u_{P_{con}} \right)^2 + \left(\frac{\partial \dot{Q}_{ave}}{\partial P_{dil}} \cdot u_{P_{dil}} \right)^2 + \left(\frac{\partial \dot{Q}_{ave}}{\partial P_{vap}} \cdot u_{P_{vap}} \right)^2 \\ + \left(\frac{\partial \dot{Q}_{ave}}{\partial T_{con}} \cdot u_{T_{con}} \right)^2 + \left(\frac{\partial \dot{Q}_{ave}}{\partial T_{dil}} \cdot u_{T_{dil}} \right)^2 + \left(\frac{\partial \dot{Q}_{ave}}{\partial T_{vap}} \cdot u_{T_{vap}} \right)^2 \\ + \left(\frac{\partial \dot{Q}_{ave}}{\partial T_{glyc,in}} \cdot u_{T_{glyc,in}} \right)^2 + \left(\frac{\partial \dot{Q}_{ave}}{\partial T_{glyc,out}} \cdot u_{T_{glyc,out}} \right)^2 \end{array} \right]^{1/2}$	$\dot{m}_{con} = 0.02644 \pm 3.96 \times 10^{-5}$ kg/s $\dot{m}_{dil} = 0.01964 \pm 2.95 \times 10^{-5}$ kg/s $\dot{m}_{glyc} = 0.1531 \pm 2.297 \times 10^{-4}$ kg/s P_{con}= 559.9±2.586 kPa P_{dil}= 553.3±2.586 kPa P_{vap}= 557.2±2.586 kPa T_{con}= 47.39±0.5°C T_{dil}= 79.39±0.5°C T_{vap}= 59.5±0.5°C $T_{glyc,in}$=93.78±0.5°C $T_{glyc,out}$=68.0±0.5°C	$\dot{Q}_{ave} = 13.01 \pm 0.2483$ kW 1.9% Uncertainty
11	**Log Mean Temperature Difference Uncertainty** $\frac{\partial LMTD_{des}}{\partial \dot{m}_{con}} = \left(\frac{LMTD_{des}\left(\dot{m}_{con} + u_{\dot{m}_{con}}\right) - LMTD_{des}\left(\dot{m}_{con} - u_{\dot{m}_{con}}\right)}{2 \cdot u_{\dot{m}_{con}}} \right)$ $\frac{\partial LMTD_{des}}{\partial \dot{m}_{dil}} = \left(\frac{LMTD_{des}\left(\dot{m}_{dil} + u_{\dot{m}_{dil}}\right) - LMTD_{des}\left(\dot{m}_{dil} - u_{\dot{m}_{dil}}\right)}{2 \cdot u_{\dot{m}_{dil}}} \right)$ $\frac{\partial LMTD_{des}}{\partial P_{con}} = \left(\frac{LMTD_{des}\left(P_{con} + u_{P_{con}}\right) - LMTD_{des}\left(P_{con} - u_{P_{con}}\right)}{2 \cdot u_{P_{con}}} \right)$	$\dot{m}_{con} = 0.02644 \pm 3.96 \times 10^{-5}$ kg/s $\dot{m}_{dil} = 0.01964 \pm 2.95 \times 10^{-5}$ kg/s P_{con}= 559.9±2.586 kPa P_{dil}= 553.3±2.586 kPa P_{vap}= 557.2±2.586 kPa T_{dil}= 79.39±0.5°C T_{vap}= 59.5±0.5°C $T_{glyc,in}$=93.78±0.5°C $T_{glyc,out}$=68.0±0.5°C	$LMTD_{des}$= 17.6±0.5588°C

Table B.1 Uncertainty Analysis (Continued)

Eq.#	Equation	Inputs	Outputs
11 Cont.	**Log Mean Temperature Difference Uncertainty (Continued)** $\frac{\partial LMTD_{des}}{\partial P_{dil}} = \left(\frac{LMTD_{des}\left(P_{dil}+u_{P_{dil}}\right) - LMTD_{des}\left(P_{dil}-u_{P_{dil}}\right)}{2 \cdot u_{P_{dil}}} \right)$ $\frac{\partial LMTD_{des}}{\partial P_{vap}} = \left(\frac{LMTD_{des}\left(P_{vap}+u_{P_{vap}}\right) - LMTD_{des}\left(P_{vap}-u_{P_{vap}}\right)}{2 \cdot u_{P_{vap}}} \right)$ $\frac{\partial LMTD_{des}}{\partial T_{dil}} = \left(\frac{LMTD_{des}\left(T_{dil}+u_{T_{dil}}\right) - LMTD_{des}\left(T_{dil}-u_{T_{dil}}\right)}{2 \cdot u_{T_{dil}}} \right)$ $\frac{\partial LMTD_{des}}{\partial T_{vap}} = \left(\frac{LMTD_{des}\left(T_{vap}+u_{T_{vap}}\right) - LMTD_{des}\left(T_{vap}-u_{T_{vap}}\right)}{2 \cdot u_{T_{vap}}} \right)$ $\frac{\partial LMTD_{des}}{\partial T_{glyc,in}} = \left(\frac{LMTD_{des}\left(T_{glyc,in}+u_{T_{glyc,in}}\right) - LMTD_{des}\left(T_{glyc,in}-u_{T_{glyc,in}}\right)}{2 \cdot u_{T_{glyc,in}}} \right)$ $\frac{\partial LMTD_{des}}{\partial T_{glyc,out}} = \left(\frac{LMTD_{des}\left(T_{glyc,out}+u_{T_{glyc,out}}\right) - LMTD_{des}\left(T_{glyc,out}-u_{T_{glyc,out}}\right)}{2 \cdot u_{T_{glyc,out}}} \right)$	$\dot{m}_{con} = 0.02644 \pm 3.96\text{x}10^{-5}$ kg/s $\dot{m}_{dil} = 0.01964 \pm 2.95\text{x}10^{-5}$ kg/s P_{con}= 559.9±2.586 kPa P_{dil}= 553.3±2.586 kPa P_{vap}= 557.2±2.586 kPa T_{dil}= 79.39±0.5°C T_{vap}= 59.5±0.5°C $T_{glyc,in}$=93.78±0.5°C $T_{glyc,out}$=68.0±0.5°C	$LMTD_{des}$= 17.6±0.5588°C

Table B.1 Uncertainty Analysis (Continued)

Eq.#	Equation	Inputs	Outputs
11 Cont.	**Log Mean Temperature Difference Uncertainty (Continued)** $u_{LMTD_{des}} = \left[\left(\frac{\partial LMTD_{des}}{\partial \dot{m}_{con}} \cdot u_{\dot{m}_{con}} \right)^2 + \left(\frac{\partial LMTD_{des}}{\partial \dot{m}_{dil}} \cdot u_{\dot{m}_{dil}} \right)^2 + \left(\frac{\partial LMTD_{des}}{\partial P_{con}} \cdot u_{P_{con}} \right)^2 + \left(\frac{\partial LMTD_{des}}{\partial P_{dil}} \cdot u_{P_{dil}} \right)^2 + \left(\frac{\partial LMTD_{des}}{\partial P_{vap}} \cdot u_{P_{vap}} \right)^2 + \left(\frac{\partial LMTD_{des}}{\partial T_{dil}} \cdot u_{T_{dil}} \right)^2 + \left(\frac{\partial LMTD_{des}}{\partial T_{vap}} \cdot u_{T_{vap}} \right)^2 + \left(\frac{\partial LMTD_{des}}{\partial T_{glyc,in}} \cdot u_{T_{glyc,in}} \right)^2 + \left(\frac{\partial LMTD_{des}}{\partial T_{glyc,out}} \cdot u_{T_{glyc,out}} \right)^2 \right]^{1/2}$	$\dot{m}_{con} = 0.02644 \pm 3.96 \times 10^{-5}$ kg/s $\dot{m}_{dil} = 0.01964 \pm 2.95 \times 10^{-5}$ kg/s P_{con}= 559.9±2.586 kPa P_{dil}= 553.3±2.586 kPa P_{vap}= 557.2±2.586 kPa T_{dil}= 79.39±0.5°C T_{vap}= 59.5±0.5°C $T_{glyc,in}$=93.78±0.5°C $T_{glyc,out}$=68.0±0.5°C	$LMTD_{des}$= 17.6±0.5588°C
12	**Overall Heat Transfer Coefficient Uncertainty** $\frac{\partial U_{des}}{\partial \dot{m}_{con}} = \left(\frac{U_{des}\left(\dot{m}_{con} + u_{\dot{m}_{con}}\right) - U_{des}\left(\dot{m}_{con} - u_{\dot{m}_{con}}\right)}{2 \cdot u_{\dot{m}_{con}}} \right)$ $\frac{\partial U_{des}}{\partial \dot{m}_{dil}} = \left(\frac{U_{des}\left(\dot{m}_{dil} + u_{\dot{m}_{dil}}\right) - U_{des}\left(\dot{m}_{dil} - u_{\dot{m}_{dil}}\right)}{2 \cdot u_{\dot{m}_{dil}}} \right)$ $\frac{\partial U_{des}}{\partial \dot{m}_{glyc}} = \left(\frac{U_{des}\left(\dot{m}_{glyc} + u_{\dot{m}_{glyc}}\right) - U_{des}\left(\dot{m}_{glyc} - u_{\dot{m}_{glyc}}\right)}{2 \cdot u_{\dot{m}_{glyc}}} \right)$	$\dot{m}_{con} = 0.02644 \pm 3.96 \times 10^{-5}$ kg/s $\dot{m}_{dil} = 0.01964 \pm 2.95 \times 10^{-5}$ kg/s $\dot{m}_{glyc} = 0.1531 \pm 2.297 \times 10^{-4}$ kg/s P_{con}= 559.9±2.586 kPa P_{dil}= 553.3±2.586 kPa P_{vap}= 557.2±2.586 kPa T_{con}= 47.39±0.5°C T_{dil}= 79.39±0.5°C T_{vap}= 59.5±0.5°C $T_{glyc,in}$=93.78±0.5°C $T_{glyc,out}$=68.0±0.5°C	$U_{des,s}$ = 493.9±20.11 W/m^2-K 4.1% Uncertainty

Table B.1 Uncertainty Analysis (Continued)

Eq.#	Equation	Inputs	Outputs
12 Cont.	**Overall Heat Transfer Coefficient Uncertainty (Continued)** $\frac{\partial U_{des}}{\partial P_{con}} = \left(\frac{U_{des}\left(P_{con}+u_{P_{con}}\right) - U_{des}\left(P_{con}-u_{P_{con}}\right)}{2 \cdot u_{P_{con}}} \right)$ $\frac{\partial U_{des}}{\partial P_{dil}} = \left(\frac{U_{des}\left(P_{dil}+u_{P_{dil}}\right) - U_{des}\left(P_{dil}-u_{P_{dil}}\right)}{2 \cdot u_{P_{dil}}} \right)$ $\frac{\partial U_{des}}{\partial P_{vap}} = \left(\frac{U_{des}\left(P_{vap}+u_{P_{vap}}\right) - U_{des}\left(P_{vap}-u_{P_{vap}}\right)}{2 \cdot u_{P_{vap}}} \right)$ $\frac{\partial U_{des}}{\partial T_{dil}} = \left(\frac{U_{des}\left(T_{dil}+u_{T_{dil}}\right) - U_{des}\left(T_{dil}-u_{T_{dil}}\right)}{2 \cdot u_{T_{dil}}} \right)$ $\frac{\partial U_{des}}{\partial T_{vap}} = \left(\frac{U_{des}\left(T_{vap}+u_{T_{vap}}\right) - U_{des}\left(T_{vap}-u_{T_{vap}}\right)}{2 \cdot u_{T_{vap}}} \right)$ $\frac{\partial U_{des}}{\partial T_{glyc,in}} = \left(\frac{U_{des}\left(T_{glyc,in}+u_{T_{glyc,in}}\right) - U_{des}\left(T_{glyc,in}-u_{T_{glyc,in}}\right)}{2 \cdot u_{T_{glyc,in}}} \right)$	$\dot{m}_{con} = 0.02644 \pm 3.96\text{x}10^{-5}$ kg/s $\dot{m}_{dil} = 0.01964 \pm 2.95\text{x}10^{-5}$ kg/s $\dot{m}_{glyc} = 0.1531 \pm 2.297\text{x}10^{-4}$ kg/s P_{con}= 559.9±2.586 kPa P_{dil}= 553.3±2.586 kPa P_{vap}= 557.2±2.586 kPa T_{con}= 47.39±0.5°C T_{dil}= 79.39±0.5°C T_{vap}= 59.5±0.5°C $T_{glyc,in}$=93.78±0.5°C $T_{glyc,out}$=68.0±0.5°C	$U_{des,s}$ = 493.9±20.11 W/m^2-K 4.1% Uncertainty

Table B.1 Uncertainty Analysis (Continued)

Eq.#	Equation	Inputs	Outputs
12 Cont.	**Overall Heat Transfer Coefficient Uncertainty (Continued)** $\frac{\partial U_{des}}{\partial T_{glyc,out}} = \left(\frac{U_{des}\left(T_{glyc,out} + u_{T_{glyc,out}}\right) - U_{des}\left(T_{glyc,out} - u_{T_{glyc,out}}\right)}{2 \cdot u_{T_{glyc,out}}} \right)$ $u_{U_{des}} = \left[\begin{array}{l} \left(\frac{\partial U_{des}}{\partial \dot{m}_{con}} \cdot u_{\dot{m}_{con}} \right)^2 + \left(\frac{\partial U_{des}}{\partial \dot{m}_{dil}} \cdot u_{\dot{m}_{dil}} \right)^2 + \left(\frac{\partial U_{des}}{\partial \dot{m}_{glyc}} \cdot u_{\dot{m}_{glyc}} \right)^2 \\ + \left(\frac{\partial U_{des}}{\partial P_{con}} \cdot u_{P_{con}} \right)^2 + \left(\frac{\partial U_{des}}{\partial P_{dil}} \cdot u_{P_{dil}} \right)^2 + \left(\frac{\partial U_{des}}{\partial P_{vap}} \cdot u_{P_{vap}} \right)^2 \\ + \left(\frac{\partial U_{des}}{\partial T_{con}} \cdot u_{T_{con}} \right)^2 + \left(\frac{\partial U_{des}}{\partial T_{dil}} \cdot u_{T_{dil}} \right)^2 + \left(\frac{\partial U_{des}}{\partial T_{vap}} \cdot u_{T_{vap}} \right)^2 \\ + \left(\frac{\partial U_{des}}{\partial T_{glyc,in}} \cdot u_{T_{glyc,in}} \right)^2 + \left(\frac{\partial U_{des}}{\partial T_{glyc,out}} \cdot u_{T_{glyc,out}} \right)^2 \end{array} \right]^{1/2}$	$\dot{m}_{con} = 0.02644 \pm 3.96\text{x}10^{-5}$ kg/s $\dot{m}_{dil} = 0.01964 \pm 2.95\text{x}10^{-5}$ kg/s $\dot{m}_{glyc} = 0.1531 \pm 2.297\text{x}10^{-4}$ kg/s P_{con}= 559.9±2.586 kPa P_{dil}= 553.3±2.586 kPa P_{vap}= 557.2±2.586 kPa T_{con}= 47.39±0.5°C T_{dil}= 79.39±0.5°C T_{vap}= 59.5±0.5°C $T_{glyc,in}$=93.78±0.5°C $T_{glyc,out}$=68.0±0.5°C	$U_{des,s}$ = 493.9±20.11 W/m^2-K 4.1% Uncertainty
13	**Solution-Side Heat Transfer Coefficient Uncertainty** $\frac{\partial \alpha_{sol}}{\partial \dot{m}_{con}} = \left(\frac{\alpha_{sol}\left(\dot{m}_{con} + u_{\dot{m}_{con}}\right) - \alpha_{sol}\left(\dot{m}_{con} - u_{\dot{m}_{con}}\right)}{2 \cdot u_{\dot{m}_{con}}} \right)$ $\frac{\partial \alpha_{sol}}{\partial \dot{m}_{dil}} = \left(\frac{\alpha_{sol}\left(\dot{m}_{dil} + u_{\dot{m}_{dil}}\right) - \alpha_{sol}\left(\dot{m}_{dil} - u_{\dot{m}_{dil}}\right)}{2 \cdot u_{\dot{m}_{dil}}} \right)$	$\dot{m}_{con} = 0.02644 \pm 3.96\text{x}10^{-5}$ kg/s $\dot{m}_{dil} = 0.01964 \pm 2.95\text{x}10^{-5}$ kg/s	α_{sol}=1037±293.2 W/m^2-K 28.2% Uncertainty

Table B.1 Uncertainty Analysis (Continued)

Eq.#	Equation	Inputs	Outputs
13 Cont.	**Solution-Side Heat Transfer Coefficient Uncertainty (Continued)** $\frac{\partial \alpha_{sol}}{\partial \dot{m}_{glyc}} = \left(\frac{\alpha_{sol}\left(\dot{m}_{glyc} + u_{\dot{m}_{glyc}}\right) - \alpha_{sol}\left(\dot{m}_{glyc} - u_{\dot{m}_{glyc}}\right)}{2 \cdot u_{\dot{m}_{glyc}}} \right)$ $\frac{\partial \alpha_{sol}}{\partial P_{con}} = \left(\frac{\alpha_{sol}\left(P_{con} + u_{P_{con}}\right) - \alpha_{sol}\left(P_{con} - u_{P_{con}}\right)}{2 \cdot u_{P_{con}}} \right)$ $\frac{\partial \alpha_{sol}}{\partial P_{dil}} = \left(\frac{\alpha_{sol}\left(P_{dil} + u_{P_{dil}}\right) - \alpha_{sol}\left(P_{dil} - u_{P_{dil}}\right)}{2 \cdot u_{P_{dil}}} \right)$ $\frac{\partial \alpha_{sol}}{\partial P_{vap}} = \left(\frac{\alpha_{sol}\left(P_{vap} + u_{P_{vap}}\right) - \alpha_{sol}\left(P_{vap} - u_{P_{vap}}\right)}{2 \cdot u_{P_{vap}}} \right)$ $\frac{\partial \alpha_{sol}}{\partial T_{dil}} = \left(\frac{\alpha_{sol}\left(T_{dil} + u_{T_{dil}}\right) - \alpha_{sol}\left(T_{dil} - u_{T_{dil}}\right)}{2 \cdot u_{T_{dil}}} \right)$ $\frac{\partial \alpha_{sol}}{\partial T_{vap}} = \left(\frac{\alpha_{sol}\left(T_{vap} + u_{T_{vap}}\right) - \alpha_{sol}\left(T_{vap} - u_{T_{vap}}\right)}{2 \cdot u_{T_{vap}}} \right)$ $\frac{\partial \alpha_{sol}}{\partial T_{glyc,in}} = \left(\frac{\alpha_{sol}\left(T_{glyc,in} + u_{T_{glyc,in}}\right) - \alpha_{sol}\left(T_{glyc,in} - u_{T_{glyc,in}}\right)}{2 \cdot u_{T_{glyc,in}}} \right)$	$\dot{m}_{con} = 0.02644 \pm 3.96 \times 10^{-5}$ kg/s $\dot{m}_{dil} = 0.01964 \pm 2.95 \times 10^{-5}$ kg/s $\dot{m}_{glyc} = 0.1531 \pm 2.297 \times 10^{-4}$ kg/s P_{con}= 559.9±2.586 kPa P_{dil}= 553.3±2.586 kPa P_{vap}= 557.2±2.586 kPa T_{con}= 47.39±0.5°C T_{dil}= 79.39±0.5°C T_{vap}= 59.5±0.5°C $T_{glyc,in}$=93.78±0.5°C $T_{glyc,out}$=68.0±0.5°C	α_{sol}=1037±293.2 W/m^2-K 28.2% Uncertainty

Table B.1 Uncertainty Analysis (Continued)

Eq.#	Equation	Inputs	Outputs
13 Cont.	**Solution-Side Heat Transfer Coefficient Uncertainty (Continued)** $\frac{\partial \alpha_{sol}}{\partial T_{glyc,out}} = \left(\frac{\alpha_{sol}\left(T_{glyc,out} + u_{T_{glyc,out}}\right) - \alpha_{sol}\left(T_{glyc,out} - u_{T_{glyc,out}}\right)}{2 \cdot u_{T_{glyc,out}}} \right)$ $u_{\alpha_{sol}} = \left[\begin{array}{l} \left(\frac{\partial \alpha_{sol}}{\partial \dot{m}_{con}} \cdot u_{\dot{m}_{con}} \right)^2 + \left(\frac{\partial \alpha_{sol}}{\partial \dot{m}_{dil}} \cdot u_{\dot{m}_{dil}} \right)^2 + \left(\frac{\partial \alpha_{sol}}{\partial \dot{m}_{glyc}} \cdot u_{\dot{m}_{glyc}} \right)^2 \\ + \left(\frac{\partial \alpha_{sol}}{\partial P_{con}} \cdot u_{P_{con}} \right)^2 + \left(\frac{\partial \alpha_{sol}}{\partial P_{dil}} \cdot u_{P_{dil}} \right)^2 + \left(\frac{\partial \alpha_{sol}}{\partial P_{vap}} \cdot u_{P_{vap}} \right)^2 \\ + \left(\frac{\partial \alpha_{sol}}{\partial T_{con}} \cdot u_{T_{con}} \right)^2 + \left(\frac{\partial \alpha_{sol}}{\partial T_{dil}} \cdot u_{T_{dil}} \right)^2 + \left(\frac{\partial \alpha_{sol}}{\partial T_{vap}} \cdot u_{T_{vap}} \right)^2 \\ + \left(\frac{\partial \alpha_{sol}}{\partial T_{glyc,in}} \cdot u_{T_{glyc,in}} \right)^2 + \left(\frac{\partial \alpha_{sol}}{\partial T_{glyc,out}} \cdot u_{T_{glyc,out}} \right)^2 \end{array} \right]^{1/2}$	$\dot{m}_{con} = 0.02644 \pm 3.96\text{x}10^{-5}$ kg/s $\dot{m}_{dil} = 0.01964 \pm 2.95\text{x}10^{-5}$ kg/s $\dot{m}_{glyc} = 0.1531 \pm 2.297\text{x}10^{-4}$ kg/s P_{con}= 559.9±2.586 kPa P_{dil}= 553.3±2.586 kPa P_{vap}= 557.2±2.586 kPa T_{con}= 47.39±0.5°C T_{dil}= 79.39±0.5°C T_{vap}= 59.5±0.5°C $T_{glyc,in}$=93.78±0.5°C $T_{glyc,out}$=68.0±0.5°C	α_{sol}=1037±293.2 W/m^2-K 28.2% Uncertainty

REFERENCES

ASHRAE (2001). *ASHRAE Handbook of Fundementals*.

Beutler, A., L. Hoffmann, F. Ziegler, G. Alefeld, K. Gommed, G. Grossman and A. Shavit (1996), "Experimental Investigation of Heat and Mass Transfer in Film Absorption on Horizontal and Vertical Tubes," *International Ab-Sorption Heat Pump Conference*, Montreal, Quebec, Canada, pp. 409-419.

Carmody, S. and S. V. Shelton (1994), "Direct Second Law Analysis of Advandced Absorption Cycles Utilizing an Ideal Solution Model," *Proceedings of the International Absorption Heat Pump Conference*, New Orleans, LA, pp. 369-374.

Churchill, S. W. and M. Bernstein (1977), "A Correlating Equation for Forced Convection from Gases and Liquids to a Circular Cylinder in Crossflow," *Journal of Heat Transfer* Vol. 99(2) pp. 300-306.

Colburn, A. P. and T. B. Drew (1937), "The Condensation of Mixed Vapours," *Transactions of the AICHE* Vol. 33(1) pp. 197-215.

DeVault, R. C. and J. Marsala (1990), "Ammonia-Water Triple-Effect Absorption Cycle," *ASHRAE Transactions* Vol. 96(1) pp. 676-682.

Engler, M., G. Grossman and H. M. Hellmann (1996), "Comparative Simulation and Investigation of Ammonia-Water Absorption Cycles for Heat Pump Applications," *Proceedings of the International Ab-sorption Heat Pump Conference*, Montreal, Canada, pp. 209-219.

Erickson, D. C., R. A. Papar and G. Anand (1996), "Basic Gax Cycle Prototype Results," *Proceedings of the International Ab-Sorption Heat Pump Conference*, Montreal, Canada, pp. 717-724.

Frances, V. M. S. and J. M. P. Ojer (2003), "Validation of a Model for the Absorption Process of H2o(Vap) by a Libr(Aq) in a Horizontal Tube Bundle, Using a Multi-Factorial Analysis," *International Journal of Heat and Mass Transfer* Vol. 46 pp. 3299-3312.

Garimella, S. (1999), "Miniaturized Heat and Mass Transfer Technology for Absorption Heat Pumps," *International Sorption Heat Pump Conference*, Munich, Germany

Garimella, S. (2004). Method and Means for Miniaturization of Binary-Fluid Heat and Mass Exchangers. 6,802,364

Garimella, S., R. N. Christensen and D. Lacy (1996), "Performance Evaluation of a Generator Absorber Heat Exchange Heat Pump," *Applied Thermal Engineering* Vol. 16(7) pp. 591-604.

Garimella, S., D. Lacy and R. E. Stout (1997), "Space-Conditioning Using Triple-Effect Absorption Heat Pumps," *Applied Thermal Engineering* Vol. 17(12) pp. 1183-1197.

Gommed, K. and G. Grossman (1990), "Performance Analysis of Staged Absorption Heat Pumps: Water-Lithium Bromide Systems," *ASHRAE Transactions* Vol. 96(1) pp. 1590-1598.

Grossman, G., K. Gommed and D. Gadoth (1991). Computer Model for Simulation of Absorption Systems in Flexible and Modular Form. Oak Ridge, TN, ORNL/Sub/90-89673p.

Grossman, G., M. Wilk and R. C. DeVault (1994), "Simulation and Performance Analysis of Triple-Effect Absorption Cycles," *ASHRAE Transactions* Vol. 100(1) pp. 452-462.

Grossman, G., A. Zaltash, P. W. Adcock and R. C. DeVault (1995), "Simulating a 4-Effect Absorption Chiller," *ASHRAE Journal* Vol. 37(6) pp. 45-53.

Herold, K. E. and M. Pande (1996), "Counterflow Vapor-Liquid Exchange Processes Using Ammonia/Water," *International Ab-Sorption Heat Pump Conference*, Montreal, Quebec, Canada, pp. 481-488.

Herold, K. E., R. Radermacher and S. A. Klein (1996). *Absorption Chillers and Heat Pumps*, CRC Press, Inc.

Ivester, D. N. and S. V. Shelton (1994), "Varying Heat Exchanger Parameters in the Triple-Effect Absorption Cycle," *Proceedings of the International Absorption Heat Pump Conference*, New Orleans, LA, ASME-AES, pp. 243-250.

Jeong, S. and S. Garimella (2002), "Falling-Film and Droplet Mode Heat and Mass Transfer in a Horizontal Tube Libr/Water Absorber," *International Journal of Heat and Mass Trasnfer* Vol. 45(7) pp. 1445-1458.

Jeong, S., S. K. Lee and K. Koo (1998), "Heat Transfer Performance of a Coiled Tube Absorber with Working Fluid of Ammonia/Water," *ASHRAE Transactions* Vol. 104(1) pp. 1577-1583.

Kang, Y. T., A. Akisawa and T. Kashiwagi (1999), "Experimental Correlation of Combined Heat and Mass Transfer for Nh3-H20 Falling Film Absorption," *International Journal of Refrigeration* Vol. 22 pp. 250-262.

Kang, Y. T., W. Chen and R. N. Christensen (1997), "Generalized Component Design Model by Combined Heat and Mass Transfer Analysis in Nh3-H2o Absorption Heat Pump Systems," *ASHRAE Transactions* Vol. 103(1) pp. 444-453.

Kang, Y. T. and R. N. Christensen (1994), "Development of a Counter-Current Model for a Vertical Fluted Tube Gax Absorber," *Proceedings of the International Absorption Heat Pump Conference*, New Orleans, LA, ASME-AES, pp. 7-16.

Killion, J. D. and S. Garimella (2001), "A Critical Review of Models of Coupled Heat and Mass Transfer in Falling-Film Absorption," *International Journal of Refrigeration* Vol. 24(8) pp. 755-797.

Killion, J. D. and S. Garimella (2003), "A Review of Experimental Investigations of Absorption of Water Vapor in Liquid Films Falling over Horizontal Tubes," *International Journal of Heating, Ventilating, Air-Conditioning and Refrigerating Research* Vol. 9(2) pp. 111-136.

Klein, S. A. (2004). *Engineering Equation Solver*. Madison, WI, F-Chart Software.

McGahey, K., S. Garimella, F. B. Cook and R. N. Christensen (1994), "Enhancement of the Ornl Absorption Model and Simulation of a Double-Effect Absorption Heat Pump," *Proceedings of the International Absorption Heat Pump Conference*, New Orleans, LA, pp. 141-148.

Meacham, J. M. and S. Garimella (2002), "Experimental Demonstration of a Prototype Microchannel Absorber for Space-Conditioning Systems," *International Sorption Heat Pump Conference*, Shanghai, China

Meacham, J. M. and S. Garimella (2002), "Experimental Demonstration of a Prototype Microchannel Absorber for Space-Conditioning Systems," *International Sorption Heat Pump Conference*, Shanghai, China, pp. 270-276.

Meacham, J. M. and S. Garimella (2003), "Modeling of Local Measured Heat and Mass Transfer Variations in a Microchannel Ammonia-Water Absorber," *Technical and Symposium Papers Presented At the 2003 Winter Meeting of The ASHRAE, Jan 26-29 2003*, Chicago, IL, United States, Amer. Soc. Heating, Ref. Air-Conditoning Eng. Inc., pp. 412-422.

Meacham, J. M. and S. Garimella (2004), "Ammonia-Water Absorption Heat and Mass Transfer in Microchannel Absorbers with Visual Confirmation," *ASHRAE Transactions* Vol. 110 PART 1 pp. 525-532.

Meacham, J. M. and S. Garimella (2004), "Simultaneous Flow Visualization and Heat and Mass Transfer in Microchannel Ammonia-Water Absorbers," *ASHRAE Transactions (in review)*.

Merrill, T., T. Setoguchi and H. Perez-Blanco (1994), "Compact Bubble Absorber Design and Analysis," *Proceedings of the International Absorption Heat Pump Conference,Jan 19-21 1994*, New Orleans,LA,USA, Publ by ASME,New York,NY,USA, pp. 217-223.

Merrill, T. L. and H. Perez-Blanco (1997), "Combined Heat and Mass Transfer During Bubble Absorption in Binary Solutions," *International Journal of Heat and Mass Trasnfer* Vol. 40(3) pp. 589-603.

Mills, A. F. (1995). *Heat and Mass Transfer*. Concord, MA, Richard D. Irwin, Inc.

Nomura, T., N. Nishimura, S. Wei, S. Yamaguchi and R. Kawakami (1994), "Heat and Mass Transfer Mechanism in the Absorber of Water/Libr Conventional Absorption Refrigerator: Experimental Examination by Visual Model," *Proceedings of the International Absorption Heat Pump Conference*, New Orleans, LA, pp. 203-208.

Perez-Blanco, H. (1988), "A Model of an Ammonia Water Falling Film Absorber," *ASHRAE Transactions* Vol. 94(1) pp. 467-483.

Potnis, S. V., A. Gomezplata, R. A. Papar, G. Anand and D. C. Erickson (1997), "Gax Component Simulation and Validation," *ASHRAE Transactions* Vol. 103(1) pp. 454-459.

Price, B. C. and K. J. Bell (1974), "Design of Binary Vapor Condensers Using the Colburn-Drew Equations," *AIChE Symposium Series - Heat Transfer - Research and Design* Vol. 70(138) pp. 163-171.

Richter, H. J. (1981), "Flooding in Tubes and Annuli," *International Journal of Multiphase Flow* Vol. 7(6) pp. 647-658.

Serpente, C. P., M. Kernen, J. S. Seewald and H. Perez-Blanco (1994), "A 2 Kw Lithium Bromide Absorption Machice with Heat Recovery and Recirculation for Novel Fluid Testing," *Proceedings of the International Absorption Heat Pump Conference*, New Orleans, LA, pp. 65-71.

Taylor, B. N. and C. E. Kuyatt (1994). *Guidelines for Evaluating and Expressing the Uncertainty of Nist Measurement Results*.

Treffinger, P. (1996), "Development and Performance of a Single Stage, High Efficient Absorption Heat Pump for Domestic Heatings," *Proceedings of the International Ab-Sorption Heat Pump Conference*, Montreal, Canada, pp. 579-585.

Wang, S. K. (2001). *Handbook of Air Conditioning and Refrigeration*. 2 Ed. New York, McGraw-Hill.

Wilke, C. R. (1950), "A Viscosity Equation for Gas Mixtures," *Journal of Chemical Physics* Vol. 18(4) pp. 517-519.

Wilke, W. (1962), "Heat Transfer to Falling Liquid Films (Waermeuebergang an Rieselfilme)," *VDI - Forschungsheft* Vol. 490 p. 36.

Ziegler, F. and G. Alefeld (1994), "Comparison of Multi-Effect Absorption Cycles," *Proceedings of the International Heat Pump Conference*, New Orleans, LA, ASME-AES, pp. 257-264.